

**SELF-ADJOINT S-PARAMETER SENSITIVITY
ANALYSIS WITH FINITE-DIFFERENCE TIME-
DOMAIN (FDTD) METHOD**

**SELF-ADJOINT S-PARAMETER SENSITIVITY
ANALYSIS WITH FINIT-DIFFERENCE TIME-
DOMAIN (FDTD) METHOD**

By

YAN LI, B. Eng.

A Thesis

Submitted to the School of Graduate Studies

in Partial Fulfillment of the Requirements

for the Degree

Master of Applied Science

McMaster University

© Copyright by Yan Li, June 2006

MASTER OF APPLIED SCIENCE (2006)
(Electrical and Computer Engineering)

McMASTER UNIVERSITY
Hamilton, Ontario

TITLE: SELF-ADJOINT S-PARAMETER SENSITIVITY
ANALYSIS WITH FINITE-DIFFERENCE TIME-DOMAIN
(FDTD) METHOD

AUTHOR: Yan Li
B. Eng. (Electrical Engineering, University of Science and
Technology of China)

SUPERVISOR: Dr. Natalia K. Nikolova, Associate Professor
Department of Electrical and Computer Engineering
Dipl. Eng. (Technical University of Varna)
Ph.D. (University of Electro-Communication)
P. Eng. (Ontario)

NUMBER OF PAGES: xv, 112

ABSTRACT

This thesis contributes to the development of a novel electromagnetic (EM) time-domain computational approach, the self-adjoint variable method, for the scattering parameter (S -parameter) sensitivity analysis of high frequency problems.

The design sensitivity analysis provides sensitivity information in the form of the response gradient (response Jacobian). For that, various techniques are used, ranging from finite-difference approximations to quadratic and spline interpolations. However, when the number of design parameters becomes large, the simulation time would become unaffordable, which is especially the case with EM simulations. The proposed self-adjoint sensitivity analysis (SASA) approach aims at providing sensitivity information efficiently without sacrificing the accuracy. Its efficiency lies in the fact that regardless of the number of design parameters, only one simulation of the original structure is required — the one used to compute the S -parameters. Thus, the sensitivity computation has negligible overhead. At the same time, it has second-order accuracy.

Currently, commercial EM simulators provide only specific engineering responses, such as Z - or S -parameters. No sensitivity information is actually made available. With the SASA approach, the only requirement for the EM solver is the ability to access the field solution at the perturbation grid points. This feature is generally available with all time-domain EM simulators. The manipulation of the field solutions in this approach is simple and it adds practically negligible overhead to the simulation time.

We confirm the validity of this approach for both the shape and constitutive parameters of the design structures. 2-D examples including metallic and dielectric details are presented, using the field solutions from an in-house time-domain solver. We also explore the feasibility of implementing this approach with one of the commercial solvers, XFDTD v. 6.3.

Suggestions for future research are provided.

ACKNOWLEDGMENTS

The author wishes to express her thanks to Dr. Natalia K. Nikolova for her supervision and research advices during the course of study. The author has greatly benefited from her expert advice, knowledge and ideas. Her patience, encouragement and understanding during the years of study will always be remembered.

It is the author's pleasure to acknowledge the collaboration and discussions with her colleagues from the Computational Electromagnetics Laboratory in Electrical & Computer Engineering Department at McMaster University: Dongying Li, Jiang Zhu, Wenhuan Yu, Ying Li and Dr. Mohamed Bakr.

Last but not least, the author would like to express her deep thanks to her parents, Lixian Li, Anqi Luo, and her fiancé Lei Zhang, for their love, understanding, encouragement and continuous support throughout the course of her work.

CONTENTS

ABSTRACT	iii
ACKNOWLEDGMENTS	v
LIST OF FIGURES	ix
LIST OF TABLES	xv
CHAPTER 1 INTRODUCTION	1
References.....	4
CHAPTER 2 THE FINITE-DIFFERENCE TIME-DOMAIN (FDTD) METHOD	7
2.1 Introduction.....	7
2.2 FDTD Basics.....	8
2.2.1 Maxwell equations.....	8
2.2.2 Excitation schemes for the FDTD method.....	13
2.3 The <i>S</i> -parameter Computation.....	16
2.3.1 Definition of the <i>S</i> -parameters.....	16
2.3.2 De-embedding.....	18
2.4 References.....	20

CHAPTER 3	THE SELF-ADJOINT SENSITIVITY ANALYSIS IN (SASA)	23
3.1	Introduction.....	23
3.2	The Adjoint-variable Method (AVM) in the Time-domain Analysis.....	24
3.2.1	Exact AVM for dynamic systems.....	24
3.2.2	Approximate AVM for structured grids.....	26
3.2.3	Vector wave equation and the original problem.....	27
3.2.4	Adjoint problem and its excitation.....	31
3.2.5	Derivatives of the system coefficients for shape perturbations.....	33
3.2.6	Derivative of the system coefficients for constitutive parameter perturbations	35
3.3	Self-adjoint Sensitivity Analysis for <i>S</i> - Parameters.....	36
3.3.1	Self-adjoint conditions.....	36
3.3.2	Summary of the self-adjoint sensitivity algorithm for <i>S</i> -parameters.....	45
3.4	2-D Implementations with an In-house FDTD Solver.....	47
3.4.1	Metallic objects.....	47
3.4.2	Dielectric objects.....	54
3.5	Summary.....	63
3.6	References.....	63
CHAPTER 4	THE FDTD S-PARAMETER SENSITIVITY ANALYSIS WITH COMMERCIAL SIMULATORS	66
4.1	Introduction.....	66
4.2	Settings in XFDTD.....	68
4.2.1	Simulation mode.....	68
4.2.2	Excitation.....	70

4.2.3	Boundaries and simulation time.....	73
4.2.4	Data export.....	74
4.3	Implementation with XFDTD.....	75
4.4	Examples.....	77
4.4.1	Single-resonator filter.....	77
4.4.2	H-plane filter.....	90
4.5	Feasibility of Other Time-domain Simulators.....	99
4.6	Summary.....	100
4.7	References.....	101
 CHAPTER 5 CONCLUSIONS		 103
 COMPLETE REFERENCE LIST		 106

LIST OF FIGURES

Figure 2.1	Allocations of the electric and magnetic field components on the Yee cell.....	11
Figure 2.2	Waveform and frequency spectrum of a sinusoidal signal modulated by a Gaussian pulse, with a central frequency at 4 GHz and HPBW of 2 GHz.....	15
Figure 2.3	A multi-port network.....	18
Figure 3.1	Field mapping technique.....	32
Figure 3.2	Original excitation $g(t)$ and assumed adjoint excitation $\hat{g}(t)=g(T_{\max}-t)$, with $T_{\max}=1600\Delta t$	41
Figure 3.3	The single-resonator filter.....	47
Figure 3.4	Comparison of the magnitudes of the S -parameters.....	50
Figure 3.5	Derivative of $\text{Re}S_{11}$ with respect to the septum width W of the single-resonator filter at the nominal design $\mathbf{p}^T=[d \ W]=[28 \ 13]$ mm.....	51
Figure 3.6	Derivative of $\text{Im}S_{11}$ with respect to the septum width W of the single-resonator filter at the nominal design $\mathbf{p}^T=[d \ W]=[28 \ 13]$ mm.....	51
Figure 3.7	Derivative of $ S_{11} $ with respect to the septum width W of the single-resonator filter at the nominal design $\mathbf{p}^T=[d \ W]=[28 \ 13]$ mm.....	52

Figure 3.8	Derivative of $\text{Re}(S_{21})$ with respect to the septum width W of the single-resonator filter at the nominal design $p^T = [d \ W] = [28 \ 13]$ mm.....	52
Figure 3.9	Derivative of $\text{Im}(S_{21})$ with respect to the septum width W of the single-resonator filter at the nominal design $p^T = [d \ W] = [28 \ 13]$ mm.....	53
Figure 3.10	Derivative of $ S_{21} $ with respect to the septum width W of the single-resonator filter at the nominal design $p^T = [d \ W] = [28 \ 13]$ mm.....	53
Figure 3.11	Recorded field points in the FDTD simulation. The points at which the field is recorded are marked with a cross. The original field and the adjoint field are needed at the points marked with circles and squares, respectively. The arrows denote the field mapping used to obtain the adjoint field of the perturbed problem.....	54
Figure 3.12	Geometry of the lossy dielectric object in vacuum.....	57
Figure 3.13	S -parameters of the structure shown in Figure 3.12.....	57
Figure 3.14	Derivative of $\text{Re}(S_{11})$ with respect to the relative permittivity ϵ_r of the central layer at the nominal design: $\epsilon_r = 15, \sigma = 0.15$ S/m.....	58
Figure 3.15	Derivative of $\text{Im}(S_{11})$ with respect to the relative permittivity ϵ_r of the central layer at the nominal design: $\epsilon_r = 15, \sigma = 0.15$ S/m.....	58
Figure 3.16	Derivative of $ S_{11} $ with respect to the relative permittivity ϵ_r of the central layer at the nominal design: $\epsilon_r = 15, \sigma = 0.15$ S/m.....	59
Figure 3.17	Derivative of $\text{Re}(S_{21})$ with respect to the relative permittivity ϵ_r of the central layer at the nominal design: $\epsilon_r = 15, \sigma = 0.15$ S/m.....	59

Figure 3.18	Derivative of $\text{Im}(S_{21})$ with respect to the relative permittivity ϵ_r of the central layer at the nominal design: $\epsilon_r = 15, \sigma = 0.15 \text{ S/m}$	60
Figure 3.19	Derivative of $ S_{21} $ with respect to the relative permittivity ϵ_r of the central layer at the nominal design: $\epsilon_r = 15, \sigma = 0.15 \text{ S/m}$	60
Figure 3.20	Derivative of $\text{Re}(S_{11})$ with respect to the conductivity σ of the central layer at the nominal design: $\epsilon_r = 15, \sigma = 0.15 \text{ S/m}$	61
Figure 3.21	Derivative of $\text{Im}(S_{11})$ with respect to the conductivity σ of the central layer at the nominal design: $\epsilon_r = 15, \sigma = 0.15 \text{ S/m}$	61
Figure 3.22	Derivative of $ S_{11} $ with respect to the conductivity σ of the central layer at the nominal design: $\epsilon_r = 15, \sigma = 0.15 \text{ S/m}$	62
Figure 3.23	The recorded points in simulation. The points with marks are the points where we record the field for both the original and the adjoint E-field.....	62
Figure 4.1	The single-resonator filter viewed in the editing window in XFDTD.....	69
Figure 4.2	The mesh setting for a 2-D simulation.....	70
Figure 4.3	Three types of sources in XFDTD.....	71
Figure 4.4	Current or voltage sources in XFDTD.....	72
Figure 4.5	The five excitation points for the simulation of the single-resonator filter.....	72
Figure 4.6	The outer-boundary section.....	74
Figure 4.7	The reference structure for the S-parameter computation..	74

Figure 4.8	Select the perturbation field points in XFDTD.....	76
Figure 4.9	The single-resonator filter.....	78
Figure 4.10	The S -parameters of the single-resonator filter ($\Delta h=1$ mm).....	80
Figure 4.11	Derivative of $\text{Re}(S_{11})$ with respect to d over a sweep of frequencies for $[d \ W] = [28\Delta h \ 13\Delta h]$ using metallization.....	81
Figure 4.12	Derivatives of $\text{Im}(S_{11})$ with respect to d over a sweep of frequencies for $[d \ W] = [28 \ \Delta h \ 13 \ \Delta h]$ using metallization.....	81
Figure 4.13	Derivatives of $ S_{11} $ with respect to d over a sweep of frequencies for $[d \ W] = [28 \ \Delta h \ 13 \ \Delta h]$ using metallization.....	82
Figure 4.14	Derivatives of $\text{Re}(S_{21})$ with respect to d over a sweep of frequencies for $[d \ W] = [28 \ \Delta h \ 13 \ \Delta h]$ using metallization.....	82
Figure 4.15	Derivatives of $\text{Im}(S_{21})$ with respect to d over a sweep of frequencies for $[d \ W] = [28 \ \Delta h \ 13 \ \Delta h]$ using metallization.....	83
Figure 4.16	Derivatives of $ S_{21} $ with respect to d over a sweep of frequencies for $[d \ W] = [28 \ \Delta h \ 13 \ \Delta h]$ using metallization.....	83
Figure 4.17	Differences in the sensitivities with respect to d between metallization and de-metallization cases.....	84
Figure 4.18	Perturbation grid points in the metallization case. The points at which the field is recorded are marked with a cross. The original field and the adjoint field are needed at the points marked with circles and squares, respectively. The arrows denote the field mapping we use to obtain the adjoint field of the perturbed problem...	84

Figure 4.19	Perturbation grid points needed in the de-metallization case. The points at which the field is recorded are marked with a cross. The original field and the adjoint field are needed at the points marked with circles and squares, respectively. The arrows denote the field mapping we use to obtain the adjoint field of the perturbed problem.....	85
Figure 4.20	Comparison of magnitudes of the S -parameters among $\Delta h=0.5$, $\Delta h=1$ mm, and HFSS results.....	86
Figure 4.21	Derivative of $\text{Re}(S_{11})$ with respect to d , with $\Delta h = 0.5$ mm.....	87
Figure 4.22	Derivative of $\text{Im}(S_{11})$ with respect to d , with $\Delta h = 0.5$ mm.....	87
Figure 4.23	Comparison of the derivatives of $ S_{11} $ with respect to d , with $\Delta h = 0.5$ mm and $\Delta h = 1$ mm.....	88
Figure 4.24	Derivative of $\text{Re}(S_{21})$ with respect to d , with $\Delta h = 0.5$ mm.....	88
Figure 4.25	Derivative of $\text{Im}(S_{21})$ with respect to d , with $\Delta h = 0.5$ mm.....	89
Figure 4.26	Comparison of the derivative of $ S_{21} $ with respect to d , with $\Delta h = 0.5$ mm and $\Delta h = 1$ mm	89
Figure 4.27	The six-resonator H-plane filter.....	92
Figure 4.28	The S -parameters of the H-plane filter.....	93
Figure 4.29	The derivative of $\text{Re}(S_{21})$ with respect to L_4 at 7 GHz for the H-plane filter.....	94
Figure 4.30	The derivative of $\text{Im}(S_{21})$ with respect to L_4 at 7 GHz for the H-plane filter.....	94
Figure 4.31	The derivative of $ S_{21} $ with respect to L_4 at 7 GHz for the H-plane filter.....	95

Figure 4.32	The derivative of $ S_{11} $ with respect to S_1 at 7 GHz for the H-plane filter.....	95
Figure 4.33	The derivative of $\text{Re}(S_{21})$ with respect to S_1 at 7 GHz for the H-plane filter.....	96
Figure 4.34	The derivative of $\text{Im}(S_{21})$ with respect to S_1 at 7 GHz for the H-plane filter.....	96
Figure 4.35	The derivative of $ S_{21} $ with respect to S_1 at 7 GHz for the H-plane filter.....	97
Figure 4.36	The recorded-field points for the derivatives with respect to L_4 . The points, at which the field is recorded, are marked with a cross. The original field and the adjoint field are needed at the points marked with circles and squares, respectively. The arrows denote the field mapping we use to obtain the adjoint field of the perturbed problem.....	97
Figure 4.37	The recorded-field points for the derivatives with respect to S_1 . The points, at which the field is recorded, are marked with a cross. The original field and the adjoint field are needed at the points marked with circles and squares, respectively. The arrows denote the field mapping we use to obtain the adjoint field of the perturbed problem.....	98

LIST OF TABLES

Table 3.1	Comparison between the desired and obtained excitations and field solutions.....	44
Table 3.2	Nominal design values of the single-resonator filter.....	50
Table 4.1	The nominal design parameter values. (All dimensions in mm).....	93
Table 4.2	Simulation time in XFDTD.....	98
Table 4.3	Derivative computation time in MATLAB.....	99

Chapter 1

INTRODUCTION

The first methods of design sensitivity analysis (DSA) can be traced back to the 1970's, when they were applied to structural engineering [1]. We also find their applications in control theory [2] and circuit theory [3], as well as the gradient-based optimization for the solution of inverse problems. The DSA studies the derivatives of a response function with respect to the design variables. The response sensitivity is represented by the gradient in the design variable space, while the design variables can be shape or constitutive parameters of the structure. There are two major techniques to evaluate the design sensitivity: the finite-difference method and the adjoint variable method (AVM). The drawback of the first method is that for each design variable, it requires at least one additional system analysis, while the second one requires at most two system analyses regardless of the number of the design variables.

The first developments in the adjoint-based DSA of microwave structures have been formulated in terms of circuit concepts and referred to as adjoint

network methods [3], [4], based on Tellegen's theory [5], [6]. Recently, a set of feasible AVM approaches for field-based electromagnetic analyses have been proposed, both in the time-domain [7]-[10] and the frequency-domain [11]-[13]. The AVM yields the sensitivity information through two system analyses: of the original and adjoint systems. In general, two system analyses are sufficient regardless of the number of design parameters. The overhead of the AVM sensitivity computation is associated with: (i) the adjoint system analysis, and (ii) the computation of the system matrix derivatives.

Some characteristics of the adjoint analysis confine the AVM approach to implementations with in-house solvers only. This is mainly due to the virtual adjoint system excitation, which is dependent on the local response function and the backward propagating wave equation. Thus, the adjoint system analysis cannot be performed with the existing commercial EM solvers unless significant modifications of the software are made. This holds back the implementation of the AVM into a versatile CAD environment.

In this thesis, we propose and implement the self-adjoint sensitivity analysis (SASA) approach with the finite-difference time-domain (FDTD) method for S -parameter sensitivity computation. In the AVM, the computational load of the adjoint system analysis is equivalent to that of the original system. It constitutes the major computational overhead. With the SASA approach, we reduce the overall computational overhead by avoiding the adjoint system analysis. The only requirements to the solver are to perform the original analysis

and to export the field at the designated perturbation points. These capabilities exist in most of the commercial solvers. Therefore, the SASA approach is independent of the solvers and its implementation with most of the time-domain EM simulators is feasible.

The author's contributions include:

- 1) The implementation of the SASA approach with the FDTD method for the S -parameter sensitivity analysis. Both metallic and dielectric details and components have been considered.
- 2) The implementation of the SASA approach with one of the commercial time-domain EM simulators, XFDTD v. 6.3 [14].

Chapter 2 briefly reviews the FDTD method and the specifics of the computation of the S -parameters, which are used in the development of the SASA approach.

Chapter 3 begins with the review of the theory of the DSA with the AVM in the time domain. The theory of the SASA approach and its implementation in the case of metallic and dielectric objects are presented afterwards. The features and the difficulties in the implementation are addressed.

Chapter 4 focuses on the implementation of the SASA approach with one of the commercial FDTD solvers, XFDTD 6.3. S -parameter computations, details of the settings and the field exporting with this solver are discussed.

The thesis concludes in Chapter 5 with suggestions for further research.

References

- [1] E. J. Haug, K. K. Choi, and V. Komkov, *Design Sensitivity Analysis of Structural System*. New York: Academic, 1996.
- [2] L. J. Lions, *Optimal Control of Systems Governed by Partial Differential Equations*. S. K Mitter, Ed. Berlin, Germany: Springer-Verlag, 1971.
- [3] S. W. Director and R. A. Rohrer, “The generalized adjoint network and network sensitivities,” *IEEE Trans. Circuit Theory*, vol. CT-16, pp. 318-323, Aug. 1969.
- [4] S. W. Director and R. A. Rohrer, “Automated network design- The frequency-domain case,” *IEEE Trans. Circuit Theory*, vol. CT-16, pp. 330-337, Aug. 1969.
- [5] B. D. H. Tellegen, “A general network theorem, with applications,” *Philips Res. Rep.*, vol. 7, pp. 259-269, 1959.
- [6] P. Penfield, Jr., R. Spence, and S. Duinker, “A generalized form of Tellegen’s theorem,” *IEEE Trans. Circuit Theory*, vol. CT-17, pp. 302-305, Aug. 1970.
- [7] N. K. Nikolova, H. W. Tam, M. H. Bakr, “Sensitivity analysis with the FDTD method on structured grids,” *IEEE Trans. Microwave Theory Tech.*, vol. 52, pp. 1207-1216, Apr. 2004.

- [8] G. Shen, H. W. W. Tam, N. K. Nikolova, M. H. Bakr, “Adjoint sensitivity techniques for FDTD method on structured grids,” *IEEE/URSI Int. Antennas and Propagation Symp. Dig. 2003*, vol. 3, Columbus, OH, June 2003, pp. 746-749.
- [9] M. H. Bakr, N. K. Nikolova, “An adjoint variable method for time domain TLM with fixed structured grids,” *IEEE/URSI Int. Antennas and Propagation Symp. Dig. 2003*, vol. 2, Columbus, OH, June 2003, pp. 1121-1124.
- [10] P. A. W. Basl, M. H. Bakr, N. K. Nikolova, “An AVM technique for 3-D TLM with symmetric condensed nodes,” *IEEE Microwave and Wireless Components Letters*, vol. 15, pp. 618-620, Oct. 2005.
- [11] N. K. Georgieva, S. Glavic, M. H. Bakr and J. W. Bandler, “Feasible adjoint sensitivity technique for EM design optimization,” *IEEE Trans. Microwave Theory Tech.*, vol. 50, pp. 2751-2758, Dec. 2002.
- [12] M. H. Bakr and N. K. Nikolova, “An adjoint variable method for frequency domain TLM problems with conducting boundaries,” *IEEE Microwave and Wireless Components Letters*, vol. 13, pp. 408-410, Sept. 2003.
- [13] S. M. Ali, N. K. Nikolova, and M. H. Bakr, “Recent advances in sensitivity analysis with frequency-domain full-wave EM solvers,” *Applied Computational Electromagnetics Society Journal*, vol. 19, pp. 147-154, Nov. 2004.

[14] XFDTD v. 6.3, Remcom, <http://www.remcom.com>.

Chapter 2

THE FINITE DIFFERENCE TIME DOMAIN (FDTD) METHOD

2.1 Introduction

The finite-difference time-domain (FDTD) method is one of the most popular numerical methods in computational electromagnetics. It converts Maxwell's curl equations to central difference equations in the time domain [1]-[5]. The field solutions are updated with Yee's algorithm, which was presented by K. S. Yee in 1966 [1]. In this chapter, the basics of the FDTD method are reviewed. First, Maxwell's equations and their discretized forms are presented. Second, excitation schemes for FDTD simulations are introduced. Finally, the computation of the S -parameters and the de-embedding technique are discussed.

2.2 FDTD Basics

The FDTD method is a numerical method to the solution of Maxwell's equations directly in the time domain over a properly discretized problem (FDTD space) [3]. It can be applied to problems containing complex high frequency (HF) structures that may be difficult to solve using analytical methods. The transient responses are obtained from the field solutions in space and in time. The frequency domain data can be obtained through the Fourier transform over a wide spectrum. The FDTD method can be applied to any inhomogeneous, lossy, anisotropic, time varying and dispersive medium. That is why the FDTD method has been widely used for solving electromagnetic problems. In this section, a brief summary of the FDTD algorithm is presented including: Yee's grid, the 3-D discretized FDTD equations, the stability criterion and the excitation schemes.

2.2.1 Maxwell equations

In a source-free, linear, isotropic and nondispersive medium, the differential form of the Maxwell's equations is [4]

$$\nabla \cdot \vec{D} = 0 \quad (2.1)$$

$$\nabla \cdot \vec{B} = 0 \quad (2.2)$$

$$\nabla \times \vec{E} = -\mu \frac{\partial \vec{H}}{\partial t} \quad (2.3)$$

$$\nabla \times \vec{H} = \varepsilon \frac{\partial \vec{E}}{\partial t} + \sigma \vec{E} \quad (2.4)$$

where:

\vec{E} is the electric field intensity (V/m),

\vec{H} is the magnetic field intensity (A/m),

\vec{D} is the electric flux density (C/m²),

\vec{B} is the electric flux density (C/m²),

ε is the electric permittivity (F/m),

σ is the electric conductivity (S/m), and

μ is the magnetic permeability (H/m).

The FDTD algorithm is based on the two Maxwell's curl equations (2.3) and (2.4).

In a rectangular coordinate system, the two equations are expanded into the system of partial differential equations:

$$\frac{\partial H_x}{\partial t} = -\frac{1}{\mu} \left(\frac{\partial E_z}{\partial y} - \frac{\partial E_y}{\partial z} \right) \quad (2.5)$$

$$\frac{\partial H_y}{\partial t} = -\frac{1}{\mu} \left(\frac{\partial E_x}{\partial z} - \frac{\partial E_z}{\partial x} \right) \quad (2.6)$$

$$\frac{\partial H_z}{\partial t} = -\frac{1}{\mu} \left(\frac{\partial E_y}{\partial x} - \frac{\partial E_x}{\partial y} \right) \quad (2.7)$$

$$\frac{\partial E_x}{\partial t} = \frac{1}{\varepsilon} \left(\frac{\partial H_z}{\partial y} - \frac{\partial H_y}{\partial z} - \sigma E_x \right) \quad (2.8)$$

$$\frac{\partial E_y}{\partial t} = \frac{1}{\varepsilon} \left(\frac{\partial H_x}{\partial z} - \frac{\partial H_z}{\partial x} - \sigma E_y \right) \quad (2.9)$$

$$\frac{\partial E_z}{\partial t} = \frac{1}{\varepsilon} \left(\frac{\partial H_y}{\partial x} - \frac{\partial H_x}{\partial y} - \sigma E_z \right). \quad (2.10)$$

Using central finite differences, the above system is discretized as [9] :

$$H_x^{n+0.5}(i, j, k) = H_x^{n-0.5}(i, j, k) - \frac{\Delta t}{\mu} \cdot \left[\frac{E_z^n(i, j, k) - E_z^n(i, j-1, k)}{\Delta y} - \frac{E_y^n(i, j, k) - E_y^n(i, j, k-1)}{\Delta z} \right] \quad (2.11)$$

$$H_y^{n+0.5}(i, j, k) = H_y^{n-0.5}(i, j, k) - \frac{\Delta t}{\mu} \cdot \left[\frac{E_x^n(i, j, k) - E_x^n(i, j, k-1)}{\Delta z} - \frac{E_z^n(i, j, k) - E_z^n(i-1, j, k)}{\Delta x} \right] \quad (2.12)$$

$$H_z^{n+0.5}(i, j, k) = H_z^{n-0.5}(i, j, k) - \frac{\Delta t}{\mu} \cdot \left[\frac{E_y^n(i, j, k) - E_y^n(i-1, j, k)}{\Delta x} - \frac{E_x^n(i, j, k) - E_x^n(i, j-1, k)}{\Delta y} \right] \quad (2.13)$$

$$E_x^{n+1}(i, j, k) = K_E^E \cdot E_x^n(i, j, k) + K_H^E \cdot \left[\frac{H_z^{n+0.5}(i, j+1, k) - H_z^{n+0.5}(i, j, k)}{\Delta y} - \frac{H_y^{n+0.5}(i, j, k+1) - H_y^{n+0.5}(i, j, k)}{\Delta z} \right] \quad (2.14)$$

$$E_y^{n+1}(i, j, k) = K_E^E \cdot E_y^n(i, j, k) + K_H^E \cdot \left[\frac{H_x^{n+0.5}(i, j, k+1) - H_x^{n+0.5}(i, j, k)}{\Delta z} - \frac{H_z^{n+0.5}(i+1, j, k) - H_z^{n+0.5}(i, j, k)}{\Delta x} \right] \quad (2.15)$$

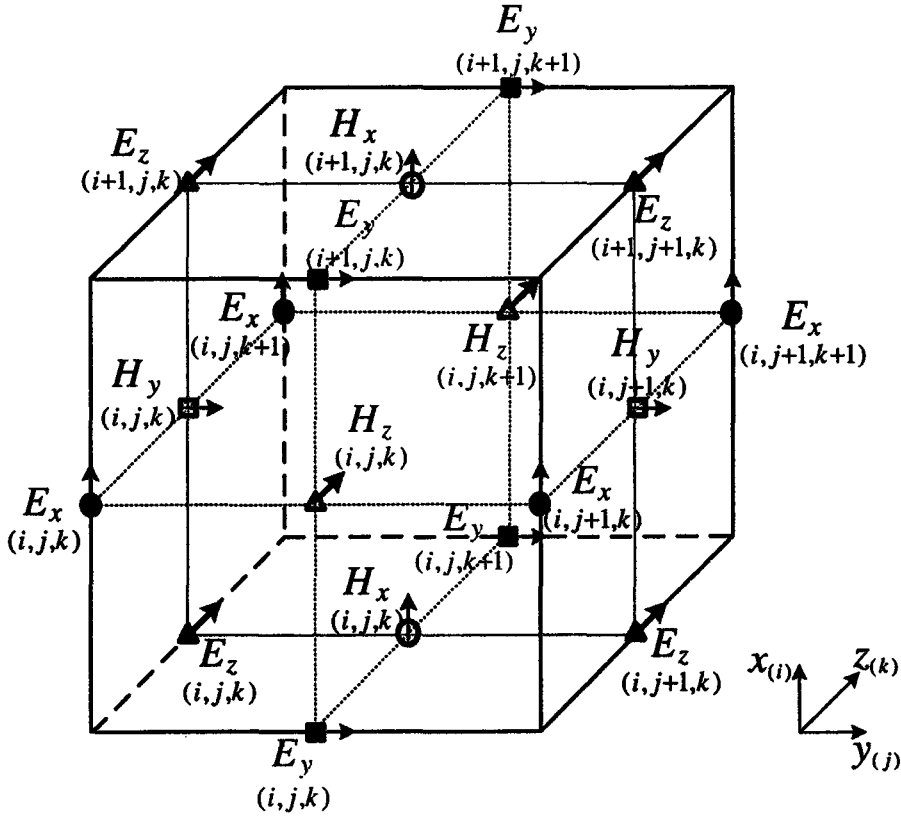


Figure 2.1 Allocations of the electric and magnetic field components on the Yee cell.

$$E_z^{n+1}(i, j, k) = K_E^E \cdot E_z^n(i, j, k) + K_H^E \cdot \left[\frac{H_y^{n+0.5}(i+1, j, k) - H_y^{n+0.5}(i, j, k)}{\Delta x} - \frac{H_x^{n+0.5}(i, j+1, k) - H_x^{n+0.5}(i, j, k)}{\Delta y} \right] \quad (2.16)$$

where

$$K_E^E = \frac{1 - \frac{\sigma \Delta t}{2\epsilon}}{1 + \frac{\sigma \Delta t}{2\epsilon}}, \text{ and } K_H^E = \frac{\Delta t}{1 + \frac{\sigma \Delta t}{2\epsilon}}. \quad (2.17)$$

The mutual location of the points at which each field component is computed is given by Yee's cell in Figure 2.1.

The numerical algorithm for Maxwell's curl equations defined by the finite difference system requires that the time step Δt has a specific bound relative to the spatial steps Δx , Δy , and Δz . This bound is necessary to avoid numerical instability [4]. The Courant's stability criterions for 1-D, 2-D and 3-D FDTD cases are defined as follows [4],

$$\begin{aligned}
 \text{1-D: } \Delta t &\leq \frac{\Delta x}{c} \\
 \text{2-D: } \Delta t &\leq \frac{1}{c} \sqrt{\left(\frac{1}{\Delta x^2} + \frac{1}{\Delta y^2}\right)^{-1}} \\
 \text{3-D: } \Delta t &\leq \frac{1}{c} \sqrt{\left(\frac{1}{\Delta x^2} + \frac{1}{\Delta y^2} + \frac{1}{\Delta z^2}\right)^{-1}}
 \end{aligned} \tag{2.18}$$

where c is the speed of light in the medium in which it is maximum.

In addition, the selection of Δx , Δy , and Δz is also crucial for the accuracy of the algorithm. In order to guarantee accuracy better than 1%, the minimal spatial step $\Delta h = \min(\Delta x, \Delta y, \Delta z)$ is typically set as [9]:

$$\begin{aligned}
 \text{1-D: } \Delta h &\leq \frac{\lambda_{\min}}{18} \\
 \text{2-D: } \Delta h &\leq \frac{\lambda_{\min}}{18\sqrt{2}} \\
 \text{3-D: } \Delta h &\leq \frac{\lambda_{\min}}{18\sqrt{3}}.
 \end{aligned} \tag{2.19}$$

When we model the structure with lossy, dispersive, nonlinear or gain materials, it is necessary to choose a smaller value for Δt to avoid the so-called late time divergence problem [5]. With the proper time and spatial steps, the FDTD simulations yield accurate and reliable responses.

2.2.2 Excitation schemes for the FDTD method

To perform a successful FDTD simulation, we have to choose the appropriate excitation. There are a number of source signals such as sinusoidal, Gaussian and sinusoidal-modulated Gaussian, that we can choose from. Gaussian pulse, either baseband or modulated, is one of the preferable source waveforms, because of its well-controlled frequency band and smooth shape.

For the waveguide structures, there are certain important aspects, which need to be considered:

1. The waveguide system usually supports a number of distinct propagating modes, which have different spatial field distributions. In order to excite the desired mode, we have to know the transverse field distribution beforehand and excite with the proper waveform with the same or similar spatial distribution as the desired mode.
2. A wideband pulsed source introduces spectral energy that travels at widely varying group velocities due to the dispersion. This can cause difficulty in specifying any numerical source condition that is not completely localized in space [4].

3. The distance between the excitation plane and the interaction structure of interest further down the waveguide has to be long enough to allow the evanescent fields to decay substantially.
4. The excitation plane should be certain distance (ten cells or more) away from the absorbing boundaries to avoid unwanted reflections from the imperfect absorbing boundary conditions (ABCs).

With the above considerations in mind, we usually choose sinusoidal signal modulated with a Gaussian pulse as the source waveform for the waveguide problems, since its band-limited frequency spectrum is well controlled by the pulse width. It can be expressed as

$$g(t) = e^{-\alpha(t-t_0)^2} \sin(2\pi f_0 t), \quad (2.20)$$

where t_0 is the center of the pulse and f_0 is the carrier frequency. Figure 2.2 shows a waveform in the time domain and its frequency spectrum for a sine modulated by a Gaussian pulse with a center frequency at 4 GHz and half-power bandwidth (HPBW) of 2 GHz.

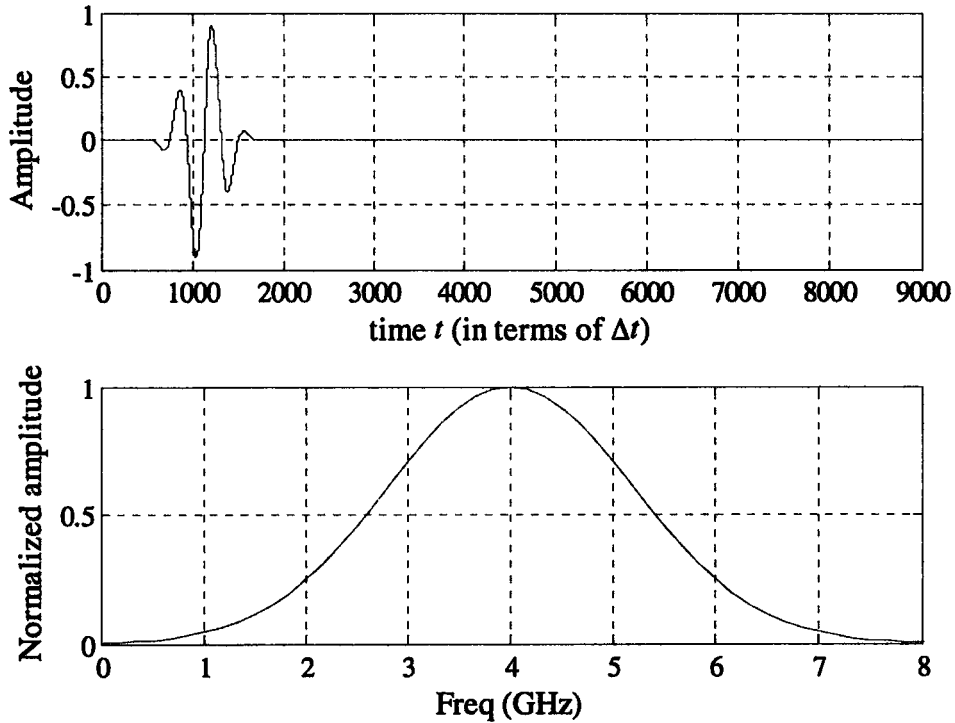


Figure 2.2 Waveform and frequency spectrum of a sinusoidal signal modulated by a Gaussian pulse, with a central frequency at 4 GHz and HPBW of 2 GHz.

We usually excite the structure using a current source, corresponding to the current density \vec{J} in the following equation,

$$\nabla \times \vec{H} = \varepsilon \frac{\partial \vec{E}}{\partial t} + \vec{J}. \quad (2.21)$$

Its discretized form in the x direction can be expressed as

$$E_x^{n+1}(i, j, k) = E_x^n(i, j, k) - \frac{\Delta t}{\epsilon} J_x^{n+0.5}(i, j, k) - \frac{\Delta t}{\epsilon} \left[\frac{H_z^{n+0.5}(i, j+1, k) - H_z^{n+0.5}(i, j, k)}{\Delta y} - \frac{H_y^{n+0.5}(i, j, k+1) - H_y^{n+0.5}(i, j, k)}{\Delta z} \right] \quad (2.22)$$

In the work to follow, we will use current-density sources.

2.3 The S -parameter Computation

2.3.1 Definition of the S -parameters

The S -parameters are frequently used for characterizing the performance of microwave and millimeter-wave circuits. For a multi-port network with N connecting ports as shown in Figure 2.3, the S -parameters can be expressed by an $N \times N$ matrix. Each element in the S -matrix can be calculated as [10]

$$S_{pq} = \frac{\tilde{F}_p}{\tilde{F}_q} \sqrt{\frac{Z_w^q}{Z_w^p}} \quad (2.23)$$

if the q th port is excited. Here,

$$\tilde{F}_p = \int_0^{T_{\max}} \iint_{S_{p\text{-port}}} \mathbf{E}_{pq}^{out}(x'_p, y'_p, t) \cdot \mathbf{M}_p(x'_p, y'_p) dx'_p dy'_p \cdot e^{-j\omega t} dt \quad (2.24)$$

$$\tilde{F}_q = \int_0^{T_{\max}} \iint_{S_{q\text{-port}}} \mathbf{E}_q^{in}(x'_q, y'_q, t) \cdot \mathbf{M}_q(x'_q, y'_q) dx'_q dy'_q \cdot e^{-j\omega t} dt \quad (2.25)$$

and Z_w^p, Z_w^q are the wave impedances of ports p and q . \mathbf{E}_{pq}^{out} and \mathbf{E}_q^{in} are the field

solutions at ports p and q ; x'_ζ, y'_ζ ($\zeta = p, q$) are local coordinates at ports p and q ; ω_0 is the frequency at which the S -parameters are computed; \mathbf{M}_p and \mathbf{M}_q are modal vectors representing the normalized field distributions of the respective modes of interest across the ports p and q [6]. The modal vectors of a port form an orthonormal basis [7]:

$$\iint_{A_\zeta} (\mathbf{e}_i^\zeta \cdot \mathbf{e}_j^\zeta) dx'_\zeta dy'_\zeta = \delta_{ij}, \quad \zeta = p, q \quad (2.26)$$

where δ_{ij} is the Kronecker delta. It is defined as

$$\delta_{ij} = \begin{cases} 0 & \text{for } i \neq j, \\ 1 & \text{for } i = j. \end{cases} \quad (2.27)$$

In particular, the modal vector of the dominant TE_{z10} mode in a rectangular waveguide port is

$$\mathbf{e}^{(\text{TE}_{10})}(x', y') = \hat{\mathbf{y}} \sqrt{\frac{2}{ab}} \sin\left(\frac{\pi}{a} x'\right) \quad (2.28)$$

where a and b denote the width and height of the port, respectively. The wave impedances Z_w^p and Z_w^q in a rectangular waveguide are computed as

$$Z_w = \frac{k\eta}{\beta} \quad (2.29)$$

for the TE mode [8]. Here, $k = \omega\sqrt{\mu\varepsilon}$ is the wavenumber in the medium, $\eta = \sqrt{\mu/\varepsilon}$ is the intrinsic impedance of the medium, and $\beta = \sqrt{k^2 - k_c^2}$ is the propagation constant, where

$$k_c = \sqrt{\left(\frac{m\pi}{a}\right)^2 + \left(\frac{n\pi}{b}\right)^2}. \quad (2.30)$$

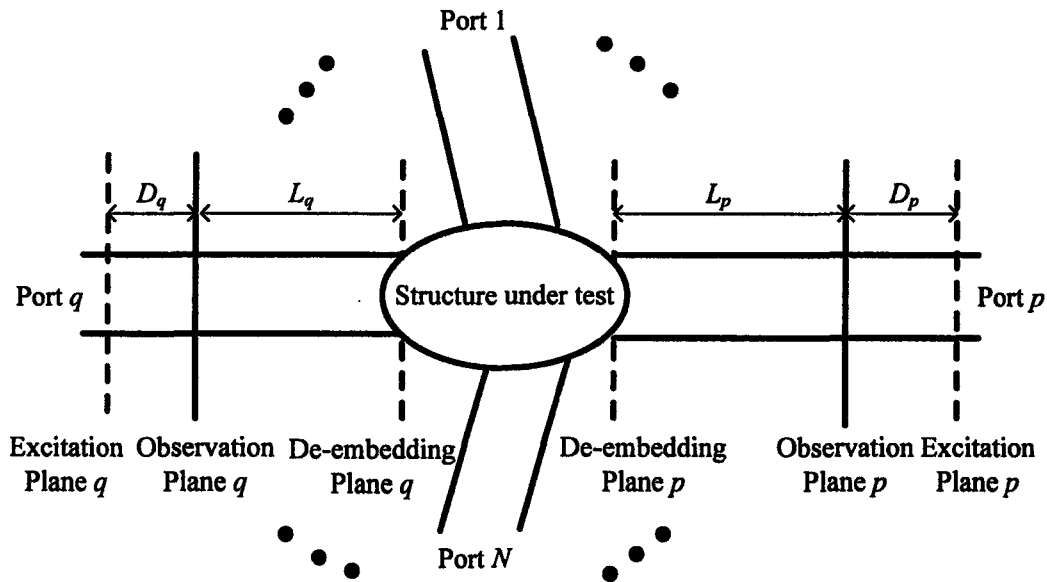


Figure 2.3 A multi-port network.

2.3.2 De-embedding

In most practical microwave circuits, there are feedlines connected to the intrinsic part of the circuit and the phase de-embedding (reference) planes are usually defined at the connections [3]. However, in the FDTD simulation, it is common practice to choose the observation plane at some distance away from the

de-embedding plane of each port in order to avoid possible higher-order and evanescent mode effects at the discontinuities. Thus, it is necessary to transform the phases of the S -parameters to the de-embedding plane as indicated in Figure 2.3. The de-embedding technique is used to account for the phase delay and, possibly, for the attenuation in a lossy line. There are two ways to account for the phase difference (see Figure 2.3).

Case 1: We assume that the de-embedding plane coincides with the excitation plane. In this case, the S -parameters are transformed from the observation plane to the excitation plane. The de-embedded S -parameter S_{pq}^{exc} is computed as

$$S_{pq}^{\text{exc}} = S_{pq}^{\text{obs}} e^{-\gamma_p D_p - \gamma_q D_q} \quad (2.31)$$

where S_{pq}^{obs} is the S -parameter computed from the observation plane signals, γ_p and γ_q are the propagation constants in the waveguides connected to the ports p and q , D_p and D_q are the distances between the observation plane and excitation plane. We assume that the observation plane is further in the port with respect to the excitation plane.

Case 2: We assume that the de-embedding plane coincides with the observation plane. In this case, we do not need to de-embed the S -parameters.

The S -parameter is given by

$$S_{pq}^{\text{obs}} = \frac{\tilde{F}_{pq}^{\text{obs}}}{\tilde{F}_q^{\text{obs}}} \sqrt{\frac{Z_w^q}{Z_w^p}}. \quad (2.32)$$

Case 3: We assume that the de-embedding plane does not coincide with any of the excitation or observation planes. The de-embedded S -parameter S_{pq}^d is computed as

$$S_{pq}^d = S_{pq}^{\text{obs}} e^{\gamma_p L_p + \gamma_q L_q} \quad (2.33)$$

where L_p and L_q are the distances between the observation and de-embedding planes. Here, we assume that the de-embedding plane is further in the port, with respect to the observation plane as shown in Figure 2.3. The S -parameter becomes

$$S_{pq}^d = \frac{\tilde{F}_{pq}^{\text{obs}}}{\tilde{F}_q^{\text{obs}}} \sqrt{\frac{Z_w^q}{Z_w^p}} \cdot e^{\gamma_p L_p + \gamma_q L_q} . \quad (2.34)$$

In some cases, we can avoid the above phase adjustments by setting the observation plane no more than two cells away from the excitation plane. This is acceptable when the port is excited with the exact modal field distribution. In this case, we ignore the phase error brought by the one or two-cell signal path.

2.4 References

- [1] K. S. Yee, “Numerical solution of initial boundary value problems involving Maxwell’s equations in isotropic media,” *IEEE Trans. Antennas Propagat.*, vol. AP-14, pp. 302-307, 1966.

- [2] T. Weiland, “A discretization method for the solution of Maxwell’s equations for six-component fields,” *Electronics and Communication (AEU)*, vol. 31, 1977, pp. 116-120.
- [3] Y. Qian and T. Itoh, *FDTD Analysis and Design of Microwave Circuits and Antennas: Software and Applications*. Realize Inc., Tokyo, 1999.
- [4] A. Taflove, *Computational Electrodynamics: the Finite-Difference Time-Domain Method*. Artech House, 1995.
- [5] K. Kunz, R. Luebbers, *Finite-Difference Time-Domain Method for Electromagnetics*. Artech House, 1995.
- [6] N. K. Nikolova, Ying Li, Yan Li, M. H. Bakr, “Sensitivity analysis of scattering parameters with electromagnetic time-domain simulators,” *IEEE Trans. Microwave Theory Tech.*, vol. 54, pp. 1598-1610, April 2006.
- [7] N. Marcuvitz, *Waveguide Handbook*. London, UK: Peter Peregrinus Ltd., 1993 reprint, Chapter 2.
- [8] D. Pozar, *Microwave Engineering*. USA: Addison Wesley Publishing Company Inc., 1993.
- [9] N. K. Nikolova, “The finite-difference time-domain (FDTD) method-part III,” lecture notes of ECE 758 Numerical Techniques in Electromagnetics, Electrical & Computer Engineering Department, McMaster University, Fall 2004.

- [10] N. K. Nikolova, “Extracting S -parameter derivatives from time domain solutions: the case,” Computational Electromagnetics Research Laboratory presentation, Dec. 2004.

Chapter 3

THE SELF-ADJOINT SENSITIVITY ANALYSIS (SASA)

3.1 Introduction

The design sensitivity analysis (DSA) concerns the relationship between the objective function and the design variables, in which the sensitivity of the objective function is represented in the form of its gradient with respect to the design variables. DSA techniques can be grouped into two categories: approximations based on response information and adjoint variable techniques. An example in the first category is the finite-difference approximation. This method requires more simulations than the adjoint variable method (AVM), because it computes the derivative of the objective function by performing at least one additional system analysis for each design variable. The AVM requires at the most two simulations regardless of the number of design parameters: one is for

the original problem and the other is for the adjoint problem. The self-adjoint AVM reduces the number of simulations to only one for certain objective functions such as the S -parameters. Compared to the finite-difference approximation, the self-adjoint method is much more efficient especially when the number of design variables is large. In this chapter, the theory of the AVM in the time-domain analysis [1], [2] is applied to the solution of Maxwell's equations with the FDTD method. The self-adjoint technique is developed for the S -parameter sensitivity computation. The self-adjoint technique is implemented and investigated through 2-D examples.

3.2 The Adjoint Variable Method (AVM) in the Time-Domain Analysis [2]

3.2.1 Exact AVM for dynamic systems [3]

After proper discretization is applied, a second-order system can be expressed as a set of system equations

$$M\ddot{\mathbf{x}} + N\dot{\mathbf{x}} + K\mathbf{x} = \mathbf{Q} \quad (3.1)$$

where M , N , K are system matrices, \mathbf{Q} is the system excitation and \mathbf{x} is the system solution. $\dot{\mathbf{x}}$ and $\ddot{\mathbf{x}}$ represent the first-order and second-order derivatives of the system solutions with respect to time, respectively. The initial conditions are typically set as $\mathbf{x}(0) = \mathbf{0}$ and $\dot{\mathbf{x}}(0) = \mathbf{0}$.

The objective function F in the DSA is defined as the integral of the local response f over time and space,

$$F = \int_{t=0}^{t=T_{\max}} \iiint_{\Omega} f(\mathbf{x}, \dot{\mathbf{x}}, \ddot{\mathbf{x}}, \mathbf{p}) d\Omega dt \quad (3.2)$$

where \mathbf{p} is the design parameter vector and Ω is the computational domain.

The n th design sensitivity is defined as the derivative of the objective function F with respect to the n th design parameter p_n as

$$\frac{\partial F}{\partial p_n} = \int_0^{T_{\max}} \left(\nabla_{\mathbf{x}} f \cdot \frac{\partial \mathbf{x}}{\partial p_n} \right) dt + \frac{\partial^e F}{\partial p_n}, \quad n = 1, 2, \dots, N \quad (3.3)$$

where N is the number of design parameters. The last term in (3.3) is the explicit dependence of F on p_n .

The first applications of the AVM technique were realized in structural engineering and control theory, where the exact sensitivity expression was used [1]. For electromagnetic (EM) problems, the exact sensitivity formula can be expressed as [5]

$$\frac{\partial F}{\partial p_n} = \frac{\partial^e F}{\partial p_n} - \int_0^{T_{\max}} \hat{\mathbf{x}}^T \cdot \frac{\partial \mathbf{R}(\bar{\mathbf{x}}, \dot{\bar{\mathbf{x}}}, \ddot{\bar{\mathbf{x}}})}{\partial p_n} dt, \quad n = 1, \dots, N \quad (3.4)$$

where the adjoint system is defined as

$$\begin{aligned} \mathbf{M}^T \hat{\ddot{\mathbf{x}}} - \mathbf{N}^T \hat{\dot{\mathbf{x}}} + \mathbf{K}^T \hat{\mathbf{x}} &= [\nabla_{\mathbf{x}} f]^T \\ \hat{\mathbf{x}}_{(t=T_{\max})} &= \mathbf{0} \\ \hat{\dot{\mathbf{x}}}_{(t=T_{\max})} &= \mathbf{0} \end{aligned} \quad (3.5)$$

and $\partial \mathbf{R}(\bar{\mathbf{x}}, \dot{\bar{\mathbf{x}}}, \ddot{\bar{\mathbf{x}}}) / \partial p_n$ is defined as

$$\frac{\partial \mathbf{R}(\bar{\mathbf{x}}, \dot{\bar{\mathbf{x}}}, \ddot{\bar{\mathbf{x}}})}{\partial p_n} = \frac{\partial \mathbf{M}}{\partial p_n} \ddot{\bar{\mathbf{x}}} + \frac{\partial \mathbf{N}}{\partial p_n} \dot{\bar{\mathbf{x}}} + \frac{\partial \mathbf{K}}{\partial p_n} \bar{\mathbf{x}} - \frac{\partial \mathbf{Q}}{\partial p_n}, \quad n = 1, \dots, N. \quad (3.6)$$

Note that the sensitivity expression includes the derivatives of the system matrices. The vectors $\bar{\mathbf{x}}$, $\dot{\bar{\mathbf{x}}}$, $\ddot{\bar{\mathbf{x}}}$ correspond to the solution of the original problem (3.1), its first-order and second-order derivatives in time, respectively. $\nabla_{\mathbf{x}} f$ is the gradient of the local response f with respect to the original system solution \mathbf{x} .

Three quantities are involved in the sensitivity expression in (3.4): 1) the original system solution $\bar{\mathbf{x}}$ and its temporal derivatives, 2) the adjoint system solution $\hat{\mathbf{x}}$, 3) the derivatives of the system matrices.

In the following section, we introduce our methodologies to modify this general sensitivity expression in order to make it feasible for applications with the FDTD method.

3.2.2 Approximate AVM for structured grids [3] [5]

When we analyze the system using the FDTD method on a structured grid, we cannot actually compute analytically the system matrix derivatives in (3.4) to (3.6). Instead, we replace them by finite-difference ratios. We derive the approximate sensitivity expression as [5]

$$\frac{\partial F}{\partial p_n} \approx \frac{\partial^e F}{\partial p_n} - \int_0^{T_{\max}} \hat{\mathbf{x}}_n^T \cdot \left(\frac{\Delta_n \mathbf{M}}{\Delta p_n} \ddot{\bar{\mathbf{x}}} + \frac{\Delta_n \mathbf{N}}{\Delta p_n} \dot{\bar{\mathbf{x}}} + \frac{\Delta_n \mathbf{K}}{\Delta p_n} \bar{\mathbf{x}} - \frac{\Delta_n \mathbf{Q}}{\Delta p_n} \right) dt, \quad n = 1, \dots, N. \quad (3.7)$$

Here, Δp_n represents the discrete perturbation of the n th design parameter, and $\Delta_n \mathbf{M}$, $\Delta_n \mathbf{N}$, $\Delta_n \mathbf{K}$, $\Delta_n \mathbf{Q}$ are the changes of the system matrices when the n th parameter is perturbed.

The adjoint solutions $\hat{\mathbf{x}}_n$ are defined by the perturbed adjoint systems

$$(\mathbf{M}_n^p)^T \hat{\mathbf{x}}_n - (\mathbf{N}_n^p)^T \hat{\mathbf{x}}_n + (\mathbf{K}_n^p)^T \hat{\mathbf{x}}_n = [\nabla_{\mathbf{x}} f]^T, \quad n = 1, 2, \dots, N. \quad (3.8)$$

Here, \mathbf{M}_n^p , \mathbf{N}_n^p and \mathbf{K}_n^p are the system matrices after the n th parameter perturbation. They are defined as

$$\begin{aligned} \mathbf{M}_n^p &= \mathbf{M} + \Delta_n \mathbf{M} \\ \mathbf{N}_n^p &= \mathbf{N} + \Delta_n \mathbf{N} \\ \mathbf{K}_n^p &= \mathbf{K} + \Delta_n \mathbf{K}. \end{aligned} \quad (3.9)$$

Note that this adjoint system is different from parameter to parameter, i.e., it is parameter dependent. The reason for the difference between (3.5) and (3.8) is that on structured grids, the adjoint system has to be defined as a perturbed system to preserve higher accuracy. The N additional adjoint analyses lead to an efficiency degrading of the AVM technique.

3.2.3 Vector wave equation and the original problem

An EM problem in a linear medium can be described by the vector wave equation for the electric field \mathbf{E} :

$$\nabla \times \mu^{-1} \nabla \times \mathbf{E} + \varepsilon \frac{\partial^2 \mathbf{E}}{\partial t^2} + \sigma \frac{\partial \mathbf{E}}{\partial t} = -\frac{\partial \mathbf{J}}{\partial t}$$

$$\mathbf{E}|_{t=0} = \mathbf{0} \quad (3.10)$$

$$\left. \frac{\partial \mathbf{E}}{\partial t} \right|_{t=0} = \mathbf{0}.$$

where ε , μ , and σ are the permittivity, permeability and conductivity of the medium, respectively. In the analysis afterwards, we assume an isotropic medium for simplicity, i.e., ε , μ , and σ are numbers rather than tensors. Here, \mathbf{J} is the excitation current density.

We discretize (3.10) by central finite differences [6] and obtain

$$\mathfrak{S}^2 \mathbf{E} - \alpha \cdot D_r \mathbf{E} - s \cdot D_{t2} \mathbf{E} = \mathbf{G} \quad (3.11)$$

where

$$\mathbf{G} = \beta \cdot D_t \mathbf{J}. \quad (3.12)$$

The constants α , β and s are defined as

$$\alpha = \varepsilon_r \left(\frac{\Delta h}{c \Delta t} \right)^2 \quad (3.13)$$

$$\beta = \mu_0 \frac{\Delta h^2}{\Delta t} \quad (3.14)$$

$$s = \frac{\sigma \mu_0}{2 \Delta t} \Delta h^2 \quad (3.15)$$

where c is the speed of light in vacuum, ε_r is the relative permittivity, μ_0 is the permeability of vacuum, Δt is the discretization step in time, and Δh is the

smallest cell size, $\Delta h = \min(\Delta x, \Delta y, \Delta z)$. The three time-domain finite-difference operators are defined as

$$D_n \mathbf{E}(t_0) = \mathbf{E}(t_0 + \Delta t) + \mathbf{E}(t_0 - \Delta t) - 2 \cdot \mathbf{E}(t_0) \quad (3.16)$$

$$D_{t2} \mathbf{E}(t_0) = \mathbf{E}(t_0 + \Delta t) - \mathbf{E}(t_0 - \Delta t) \quad (3.17)$$

$$D_t \mathbf{J}(t_0) = \mathbf{J}(t_0 + \Delta t / 2) - \mathbf{J}(t_0 - \Delta t / 2). \quad (3.18)$$

The difference between the first-order time operators in (3.17) and (3.18) is due to a half time-step shift of the discretization of the electric field and the current density in Yee's algorithm. In rectangular coordinates, the double curl operator \mathfrak{S}^2 produces three components as follows,

$$(\mathfrak{S}^2 \mathbf{E})_x = h_y^2 D_{yy} E_x + h_z^2 D_{zz} E_x - h_y h_x D_{yx} E_y - h_z h_x D_{zx} E_z \quad (3.19)$$

$$(\mathfrak{S}^2 \mathbf{E})_y = h_x^2 D_{xx} E_y + h_z^2 D_{zz} E_y - h_z h_y D_{zy} E_z - h_x h_y D_{xy} E_x \quad (3.20)$$

$$(\mathfrak{S}^2 \mathbf{E})_z = h_x^2 D_{xx} E_z + h_y^2 D_{yy} E_z - h_x h_z D_{xz} E_x - h_y h_z D_{yz} E_y \quad (3.21)$$

where

$$h_x = \frac{\Delta h}{\Delta x}, \quad h_y = \frac{\Delta h}{\Delta y}, \quad h_z = \frac{\Delta h}{\Delta z}. \quad (3.22)$$

Using central finite differences and the notations in Section 2.2.1, we write the operators in (3.19) to (3.21) as

$$D_{yy} E_x \Big|_{i,j,k} = E_x^{i,j+1,k} + E_x^{i,j-1,k} - 2E_x^{i,j,k} \quad (3.23)$$

$$D_{zz} E_x \Big|_{i,j,k} = E_x^{i,j,k+1} + E_x^{i,j,k-1} - 2E_x^{i,j,k} \quad (3.24)$$

$$D_{zx} E_z \Big|_{i,j,k} = E_z^{i+1,j,k} - E_z^{i,j,k} + E_z^{i,j,k-1} - E_z^{i+1,j,k-1} \quad (3.25)$$

$$D_{yx}E_y|_{i,j,k} = E_y^{i+1,j,k} - E_y^{i,j,k} + E_y^{i,j-1,k} - E_y^{i+1,j-1,k} \quad (3.26)$$

$$D_{xx}E_y|_{i,j,k} = E_y^{i+1,j,k} + E_y^{i-1,j,k} - 2E_y^{i,j,k} \quad (3.27)$$

$$D_{zz}E_y|_{i,j,k} = E_y^{i,j,k+1} + E_y^{i,j,k-1} - 2E_y^{i,j,k} \quad (3.28)$$

$$D_{xy}E_x|_{i,j,k} = E_x^{i,j+1,k} - E_x^{i,j,k} + E_x^{i-1,j,k} - E_x^{i-1,j+1,k} \quad (3.29)$$

$$D_{zy}E_z|_{i,j,k} = E_z^{i,j+1,k} - E_z^{i,j,k} + E_z^{i,j,k-1} - E_z^{i,j+1,k-1} \quad (3.30)$$

$$D_{xx}E_z|_{i,j,k} = E_z^{i+1,j,k} + E_z^{i-1,j,k} - 2E_z^{i,j,k} \quad (3.31)$$

$$D_{yy}E_z|_{i,j,k} = E_z^{i,j+1,k} + E_z^{i,j-1,k} - 2E_z^{i,j,k} \quad (3.32)$$

$$D_{xz}E_x|_{i,j,k} = E_x^{i,j,k+1} - E_x^{i,j,k} + E_x^{i-1,j,k} - E_x^{i-1,j,k+1} \quad (3.33)$$

$$D_{yz}E_y|_{i,j,k} = E_y^{i,j,k+1} - E_y^{i,j,k} + E_y^{i,j-1,k} - E_y^{i,j-1,k+1} \quad (3.34)$$

where (i, j, k) is the index of the grid point.

This is the original problem to solve. It is worth mentioning that we do not actually solve the problem with the discretized vector-wave equation. The system analysis is carried out with the FDTD method. The above equations are used in the sensitivity analysis only to determine the system coefficients. More specifically, they are used to compute the system matrix derivatives, as discussed in Sections 3.2.5 and 3.2.6.

3.2.4 Adjoint problem and its excitation

According to (3.5), the adjoint system can be expressed as

$$\begin{aligned} \nabla \times [\boldsymbol{\mu}^{-1}]^T \nabla \times \hat{\mathbf{E}} + \boldsymbol{\varepsilon}^T \frac{\partial^2 \hat{\mathbf{E}}}{\partial \tau^2} + \boldsymbol{\sigma}^T \frac{\partial \hat{\mathbf{E}}}{\partial \tau} &= \frac{\partial \hat{\mathbf{J}}}{\partial \tau} \\ \hat{\mathbf{E}} \Big|_{\tau=0} &= \mathbf{0} \\ \frac{\partial \hat{\mathbf{E}}}{\partial \tau} \Big|_{\tau=0} &= \mathbf{0}. \end{aligned} \quad (3.35)$$

Here, τ is the inverse-time variable, $\tau = T_{\max} - t$. Equivalently, it can be solved with the adjoint Maxwell system [5], [7]

$$\begin{aligned} \nabla \times \hat{\mathbf{H}} &= - \left(\frac{\partial \boldsymbol{\varepsilon}^T \hat{\mathbf{E}}}{\partial \tau} + \boldsymbol{\sigma}^T \hat{\mathbf{E}} \right) + \hat{\mathbf{J}} \\ \nabla \times \hat{\mathbf{E}} &= \frac{\partial \boldsymbol{\mu}^T \hat{\mathbf{H}}}{\partial \tau}. \end{aligned} \quad (3.36)$$

To solve the adjoint system, we have to use a backward-update scheme, proposed in [5]. This scheme becomes the same as the one we use to solve the original system, provided that we rewrite (3.35) and (3.36) in terms of $(-\hat{\mathbf{E}})$ instead of $\hat{\mathbf{E}}$, and use $(-\hat{\mathbf{J}})$ instead of $\hat{\mathbf{J}}$ as the adjoint excitation.

The adjoint excitation $\hat{\mathbf{J}}$ is a quasi-current density whose distribution in space-time depends on the local response $f(\mathbf{E}, \mathbf{p})$ according to (3.8) as:

$$\beta D_t \hat{\mathbf{J}} = \hat{\mathbf{x}} \frac{\partial f}{\partial E_x} + \hat{\mathbf{y}} \frac{\partial f}{\partial E_y} + \hat{\mathbf{z}} \frac{\partial f}{\partial E_z}. \quad (3.37)$$

To overcome the parameter-dependent feature of the adjoint system discussed in Section 3.2.2, approximation methodologies are proposed both in the transmission line method (TLM) [4] and the FDTD method [5]. Instead of solving N different perturbed adjoint systems, we solve only one unperturbed adjoint system and obtain all the required field values by a simple mapping. For the computation of shape sensitivities, only the field points around the perturbation region are needed. Therefore, we can approximate their values by the fields with a shift in space in the direction of the assumed n th parameter perturbation. Figure 3.1 illustrates how the mapping technique works in a 2-D problem.

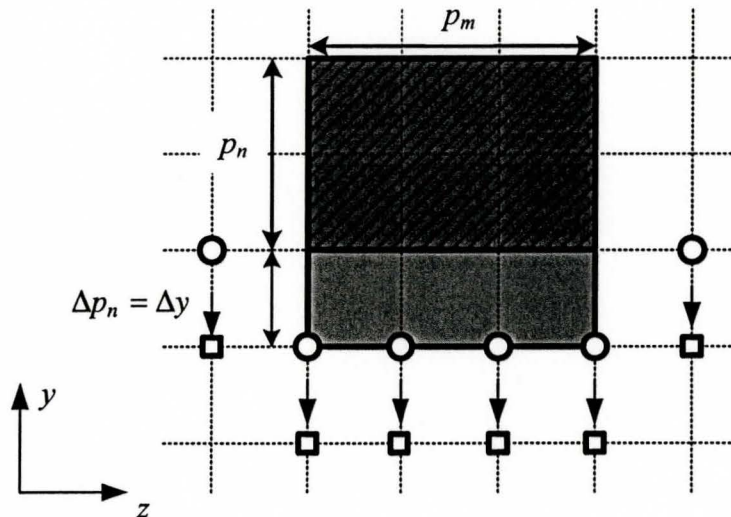


Figure 3.1 Field mapping technique.

In Figure 3.1, the dark area represents the original structure. In order to compute the adjoint field $\hat{\mathbf{E}}_n$ for a perturbation in the parameter p_n , we perturb the structure one cell further along the p_n direction, see the light-gray area. The adjoint field points of the perturbed problem involved in the sensitivity calculation are the square points. They are approximated by the adjoint field values at the circle points. Following this methodology, all N perturbed adjoint field solutions for the computation of the N parameter sensitivities can be obtained from only one unperturbed adjoint system analysis. The total number of system analyses for the response and its sensitivities becomes two, compared with $2N+1$ system analyses if a central finite-difference method is used.

3.2.5 Derivatives of the system coefficients for shape perturbations

When the design parameters relate to the shape, the derivatives of the system matrices cannot be mathematically defined [5], [8]. In this case, we resort to finding the differences of the system coefficients in two system states: the nominal (unperturbed) state and the n th perturbed state. In the n th perturbed state, the parameter p_n changes to $p_n + \Delta p_n$ while all other parameters are kept at their nominal values. The change Δp_n is usually chosen to be one cell, which is the smallest possible on-grid change. As a consequence, the system coefficients in (3.11) at the perturbation grid points change.

The perturbation grid points are the points where either the original or the

adjoint field is needed for the sensitivity computation. For example, for the computation of shape sensitivities of a perfect metallic object, the perturbation grid points are those being metallized or de-metallized during the perturbation. For the computation of constitutive-parameter sensitivities of a dielectric object, the perturbation grid points are those in the volume of the object whose permittivity changes.

The perturbations leading to the change of those three system coefficients can be classified as follows:

1. Change of the double curl operator \mathfrak{S}^2 .

When the structure is metallic, the cells in the perturbation region become metallized or de-metallized. If they are metallized, the tangential electric field components become zero. Correspondingly, the components of \mathfrak{S}^2 multiplying these electric field components become zero. Similarly, if the object is de-metallized, the tangential electric field components change from zero to the value defined by (3.19) to (3.21). Also, an implicit current term \mathbf{G} becomes zero [5].

2. Change of α .

When the shape parameter relates to a dielectric object immersed in a host medium of different permittivity, the perturbation affects the local permittivity at the perturbation grid points, which changes from that of the object to that of the host medium or vice versa. This results in a change of the coefficient α at these points.

3. Change of s .

Similarly to case 2, a change in the shape of a lossy object affects the local conductivity at the perturbation grid points. This results in a change of the coefficient s .

Through the system coefficient differences, the system coefficient derivatives are replaced by $\Delta_n \mathfrak{S}^2 / \Delta p_n$, $\Delta_n \alpha / \Delta p_n$, and $\Delta_n s / \Delta p_n$. Note that these difference ratios are in general not a good approximation of the respective coefficient derivatives. For example, the relative permittivity at a perturbation grid point changes from 1 to 40 when the shape of a dielectric resonator of $\epsilon_r = 40$ changes. As a result, α at this point changes by a factor of 40. In this case, $\Delta_n \alpha / \Delta p_n$ cannot be considered as an approximation of $\partial \alpha / \partial p_n$ at all.

3.2.6 Derivatives of the system coefficients for constitutive parameter perturbations [9]

When the design parameter is a local permittivity or conductivity, we can obtain the analytical derivatives of the system coefficients. According to (3.13) and (3.15), the derivatives can be computed as

$$\frac{d\alpha}{d\epsilon_r} = \left(\frac{\Delta h}{c\Delta t} \right)^2 \quad (3.38)$$

$$\frac{ds}{d\sigma} = \frac{\mu_0 \Delta h^2}{2\Delta t}. \quad (3.39)$$

Therefore, the system coefficient derivatives are analytical and the sensitivities can be computed exactly with (3.4). Also, with analytical derivatives of the

system coefficients, the adjoint solution $\hat{\mathbf{E}}$ must correspond to the unperturbed structure, as implied by (3.4). There is no need for the solution mapping [5], which is necessary when dealing with shape parameters and the coefficient difference ratios.

We notice that the sensitivity computation by the AVM with respect to the constitutive parameters is more reliable compared to the shape parameters. This is because it eliminates the inaccuracy in the system matrix derivatives and the adjoint field solution approximation through the mapping. It depends only on the accuracy of the field solution.

3.3 Self-adjoint Sensitivity Analysis for S -Parameters

3.3.1 Self-adjoint conditions [7]

In this section, we use the S -parameter formula without de-embedding. The phase adjustment can be done after the computations described below. Following the S -parameter definition and the notations in Section 2.3, the sensitivity of the S -parameter with respect to the n th design parameter can be expressed as

$$\frac{\partial S_{pq}}{\partial p_n} = \sqrt{\frac{Z_w^q}{Z_w^p}} \cdot \frac{1}{\tilde{F}_q} \cdot \frac{\partial \tilde{F}_{pq}}{\partial p_n}. \quad (3.40)$$

Here, we assume that Z_w^p , Z_w^q and \tilde{F}_q are not dependent on the design parameters, and the derivative depends only on the output port response \tilde{F}_p . Our objective becomes to compute the derivative $\partial \tilde{F}_{pq} / \partial p_n$, where \tilde{F}_{pq} is defined as

$$\tilde{F}_{pq} = \int_0^{T_{\max}} \iint_{S_{p\text{-port}}} \mathbf{E}_{pq} \cdot \mathbf{M}_p dx'_p dy'_p \cdot e^{-j\omega t} dt. \quad (3.41)$$

Here, \mathbf{E}_{pq} is the E-field observed at port p when port q is excited. \mathbf{M}_p is the field modal distribution at port p . Following the definition of the objective function in (3.2), we find our local response as

$$f(x'_p, y'_p, t) = \frac{\mathbf{E}_{pq}(x'_p, y'_p, t) \cdot \mathbf{M}_p(x'_p, y'_p)}{\Delta z_p} \cdot e^{-j\omega t} \quad (3.42)$$

where Δz_p is the longitudinal discretization step at port p . Note that we have Δz_p in the denominator to account for the difference between the integral of the objective function F in (3.2) and that of \tilde{F}_{pq} in (3.41). In (3.2), we have a volume integral, while \tilde{F}_{pq} is defined by the double integral across the port.

We rewrite the term $e^{-j\omega t}$ into its complex form and split the local response f into its real and imaginary parts as

$$f_R(x'_p, y'_p, t) = \frac{\mathbf{E}_{pq}(x'_p, y'_p, t) \cdot \mathbf{M}_p(x'_p, y'_p)}{\Delta z_p} \cdot \cos(\omega_0 t) \quad (3.43)$$

$$f_I(x'_p, y'_p, t) = -\frac{\mathbf{E}_{pq}(x'_p, y'_p, t) \cdot \mathbf{M}_p(x'_p, y'_p)}{\Delta z_p} \cdot \sin(\omega_0 t). \quad (3.44)$$

For each of the responses f_R and f_I , we have two different adjoint systems.

According to (3.37), their excitation waveforms are defined as

$$\beta \frac{\partial \hat{\mathbf{J}}_{pq}^v}{\partial t} = \frac{1}{\Delta t} \left(\hat{\mathbf{x}} \frac{\partial f_v}{\partial E_x} + \hat{\mathbf{y}} \frac{\partial f_v}{\partial E_y} + \hat{\mathbf{z}} \frac{\partial f_v}{\partial E_z} \right), \quad v = R, I \quad (3.45)$$

where $\hat{\mathbf{J}}_{pq}^v$ ($v = R, I$) is the adjoint current excitation for the computation of the derivative of the real and imaginary parts of S_{pq} . $\partial f_v / \partial E_\zeta$, ($v = R, I$ and $\zeta = x, y, z$) are defined as

$$\frac{\partial f_R}{\partial E_\zeta} = \frac{M_{p,\zeta}(x', y')}{\Delta z_p} \cdot \cos(\omega_0 t), \quad \zeta = x, y, z \quad (3.46)$$

$$\frac{\partial f_I}{\partial E_\zeta} = -\frac{M_{p,\zeta}(x', y')}{\Delta z_p} \cdot \sin(\omega_0 t), \quad \zeta = x, y, z. \quad (3.47)$$

Substituting (3.46) and (3.47) into (3.45), and integrating over time, we obtain the expressions for the excitation current density of the adjoint system for the calculation of the real and imaginary parts of the S_{pq} derivatives:

$$(-\hat{\mathbf{J}}_{pq}^R)_\zeta = \frac{1}{\beta \Delta t} \int \frac{\partial f_R}{\partial E_\zeta} dt = \frac{1}{\omega_0 \beta \Delta t} \frac{M_{p,\zeta}(x', y')}{\Delta z_p} \cdot \sin(\omega_0 t), \quad \zeta = x, y, z \quad (3.48)$$

$$(-\hat{\mathbf{J}}_{pq}^I)_\zeta(x', y', t) = \frac{1}{\omega_0 \beta \Delta t} \frac{M_{p,\zeta}(x', y')}{\Delta z_p} \cdot \cos(\omega_0 t), \quad \zeta = x, y, z. \quad (3.49)$$

Here, we add a minus sign before the current density to ensure the correct sign of the adjoint **E**-field solution as explained in Section 3.2.4. The two current densities in (3.48) and (3.49) can also be expressed in the following form:

$$(-\hat{\mathbf{J}}_{pq})_R(x'_p, y'_p, t) = \mathbf{M}_p(x'_p, y'_p) \cdot \hat{\mathbf{g}}_R^{\omega_0}(t) \quad (3.50)$$

$$(-\hat{\mathbf{J}}_{pq})_I(x'_p, y'_p, t) = \mathbf{M}_p(x'_p, y'_p) \cdot \hat{g}_I^{\omega_b}(t) \quad (3.51)$$

where

$$\hat{g}_R^{\omega_b}(t) = \frac{\sin(\omega_0 t)}{\omega_0 \beta \Delta t \Delta z_p} \quad (3.52)$$

$$\hat{g}_I^{\omega_b}(t) = \frac{\cos(\omega_0 t)}{\omega_0 \beta \Delta t \Delta z_p} \quad (3.53)$$

are the waveforms of the adjoint excitations for the real and imaginary S -parameter sensitivities, respectively. The modal distribution $\mathbf{M}_p(x'_p, y'_p)$ of the current density at port p of the adjoint problem is the same as that of port p in the original problem. The latter can be expressed as

$$\mathbf{J}_p(x'_p, y'_p, t) = J_p \cdot \mathbf{M}_p(x'_p, y'_p) \cdot g(t) \quad (3.54)$$

where J_p is a scaling factor, and $g(t)$ is the excitation waveform.

As discussed in Section 3.2.4, we use the same updating scheme to solve the original and adjoint systems, which share the same boundary conditions and initial conditions. This means that the two systems are equivalent, except for their excitations. Therefore, the condition which can make them have the same field solutions is that they must have identical excitations in terms of spatial distribution and temporal waveforms.

The excitation current densities of the adjoint system in (3.50)-(3.51) have the following two features:

- 1) They have the same modal distribution in space as the original system excitation — compare with (3.54).

- 2) They have time-harmonic waveforms.

The difference between the original and the adjoint system excitations lies in their temporal waveforms. We seek certain relationship between them to obtain the adjoint field solutions without performing the adjoint system analysis.

We can obtain the time-harmonic responses of a linear structure by exciting it with a time-limited pulse (e.g., a Gaussian pulse) and then performing the Fourier transform (FT) to obtain the desired spectral components. Therefore, it is possible to obtain the time-harmonic responses of the adjoint system by utilizing the same excitation scheme as that of the original structure and the FT. This adjoint system analysis is then exactly the same as the original system analysis and need not be carried out. The detailed manipulations of obtaining the adjoint field solution from the original one are discussed below.

Suppose the time waveform of the original excitation is $g(t)$. In order to have identical field solutions from the original and the adjoint systems, we assume the adjoint excitation to have the same waveform in reverse time τ as $g(t)$ in forward time. Here, τ is defined as the inverse time variable,

$$\tau = T_{\max} - t \quad (3.55)$$

where T_{\max} is the total simulation time. Thus, we have

$$\hat{g}(t) = g(T_{\max} - t). \quad (3.56)$$

The above is equivalent to $\hat{g}(\tau) = g(t)$.

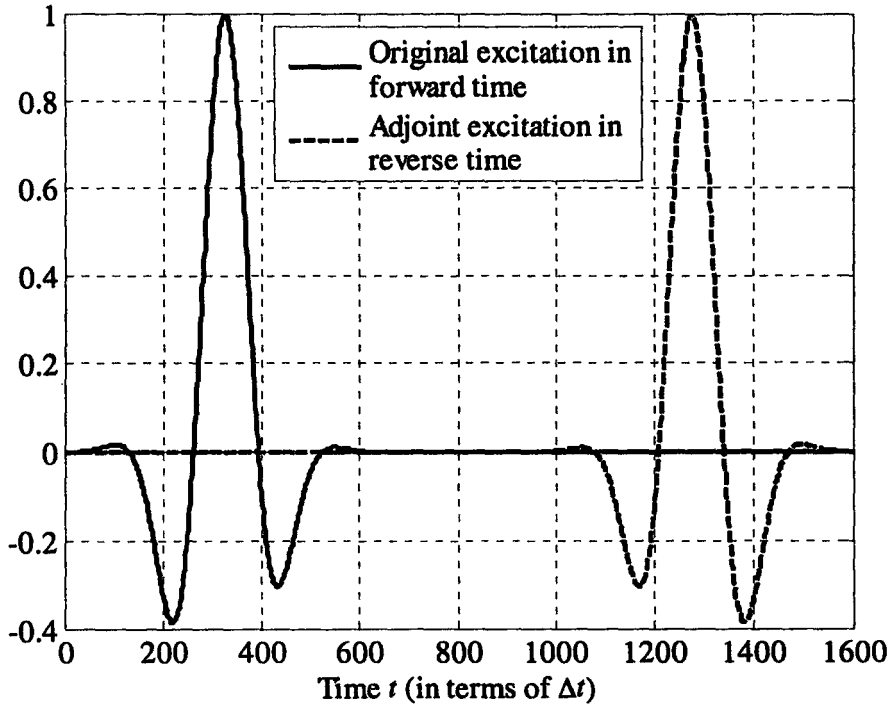


Figure 3.2 Original excitation $g(t)$ and assumed adjoint excitation $\hat{g}(t)=g(T_{\max}-t)$, with $T_{\max}=1600\Delta t$.

Figure 3.2 shows both the original excitation waveform $g(t)$ in forward time t and the assumed adjoint excitation waveform $\hat{g}(t)=g(T_{\max}-t)$ with T_{\max} equal to 1600 time steps.

We apply the FT to both excitation waveforms. The ω_0 spectral component of the forward pulse $g(t)$ can be found as

$$\underline{G} = \int_0^{T_{\max}} g(t) \cdot e^{-j\omega_0 t} dt = G_m \cdot e^{j\varphi_s}. \quad (3.57)$$

The reversed pulse $\hat{g}(t)=g(T_{\max}-t)$ has its ω_0 spectral component given by

$$\hat{G} = \int_0^{T_{\max}} g(T_{\max} - t) \cdot e^{-j\omega_0 t} dt = G^* \cdot e^{-j\omega_0 T_{\max}} = G_m \cdot e^{-j(\omega_0 T_{\max} + \varphi_g)}. \quad (3.58)$$

Here, G^* is the conjugate of G , and G_m is the magnitude of G as defined in (3.57). Thus, the ω_0 spectral component of $\hat{g}(t)$ is

$$\hat{g}^{\omega_0}(t) = G_m \cos(\omega_0 t - \varphi_g - \omega_0 T_{\max}). \quad (3.59)$$

We now compare the desired adjoint excitation waveforms in (3.48) and (3.49) with the ω_0 component of the adjoint pulse in (3.59). Their magnitudes and phases are related as follows,

$$|\hat{g}_R^{\omega_0}| = |\hat{g}_I^{\omega_0}| = \frac{|\hat{g}^{\omega_0}|}{G_m \omega_0 \beta \Delta t \Delta z_p} \quad (3.60)$$

$$\text{Angle}\{\hat{g}_R^{\omega_0}\} = \text{Angle}\{\hat{g}^{\omega_0}\} + \varphi_g + \omega_0 T_{\max} - \pi/2 \quad (3.61)$$

$$\text{Angle}\{\hat{g}_I^{\omega_0}\} = \text{Angle}\{\hat{g}^{\omega_0}\} + \varphi_g + \omega_0 T_{\max}. \quad (3.62)$$

We now examine the relationship of the field solutions between the original and the adjoint systems. Due to the equivalence between the forward-running original and the backward-running adjoint problems, the so obtained adjoint field is related to the original one as

$$\hat{E}_{pq}(P, T_{\max} - t) = E_p(P, t) \quad (3.63)$$

at a point P . The ω_0 spectral component of the adjoint field solution is

$$\hat{E}_{\zeta pq}^{\omega_0}(P, t) = |E_{\zeta p(P)}^{\omega_0}| \cos(\omega_0 t - \varphi_{e\zeta p(P)} - \omega_0 T_{\max}), \quad \zeta = x, y, z. \quad (3.64)$$

Here, ζ denotes the vector component; $|E_{\zeta p(P)}^{\omega_0}|$ and $\varphi_{e\zeta p(P)}$ are the magnitude and the phase of the ω_0 spectral component of the original waveform $E_{\zeta pq}$ at P .

The desired adjoint fields $(\hat{E}_{pq})_R$ and $(\hat{E}_{pq})_I$ can be obtained from the ω_0 component of the adjoint field (3.64) by: 1) scaling the magnitude by the factor in (3.60), and 2) adding the difference in the angles in (3.61) and (3.62) to their respective phases. The so obtained adjoint field for the real and the imaginary parts of $\partial S_{pq} / \partial p_n$ becomes:

$$(\hat{E}_{\zeta pq}^{\omega_0})_R(P, t) = \frac{|E_{\zeta p(P)}^{\omega_0}|}{J_p G_m \omega_0 \beta \Delta t \Delta z_p} \cos\left(\omega_0 t - \varphi_{e\zeta p(P)} + \varphi_g - \frac{\pi}{2}\right) \quad (3.65)$$

$$(\hat{E}_{\zeta pq}^{\omega_0})_I(P, t) = \frac{|E_{\zeta p(P)}^{\omega_0}|}{J_p G_m \omega_0 \beta \Delta t \Delta z_p} \cos(\omega_0 t - \varphi_{e\zeta p(P)} + \varphi_g) \quad (3.66)$$

$$\zeta = x, y, z.$$

Here, the scaling factor J_p is added in the denominator to account for the actual strength of the source, see (3.54). In (3.65) and (3.66), G_m and φ_g are obtained through the FT of the original excitation pulse $g(t)$ as per (3.57), while $|E_{\zeta p(P)}^{\omega_0}|$ and $\varphi_{e\zeta p(P)}$ are obtained through the FT of the E-field recorded at a perturbation grid point P during the original simulation, in which port p is excited. To illustrate the manipulations of the magnitudes and the phases, a comparison of the desired and obtained excitations and field solutions are listed in Table 3.1. In this table, the desired quantities are from (3.52), (3.53), (3.65) and (3.66). The obtained quantities are from (3.59) and (3.64).

In conclusion, we do not need to perform any adjoint simulations in order to compute the derivatives of the whole scattering matrix with respect to all design parameters. The necessary information is already contained in the EM field solution of the original problem. Our algorithm, which exploits the self-adjoint nature of the linear problem, uses this information in the most efficient manner.

Table 3.1: Comparison between the desired and obtained excitations and field solutions.

	Desired quantities	Obtained quantities
Excitations	$\hat{g}_R^{\omega_0}(t) = \frac{\sin(\omega_0 t)}{\omega_0 \beta \Delta t \Delta z_p},$ $\hat{g}_I^{\omega_0}(t) = \frac{\cos(\omega_0 t)}{\omega_0 \beta \Delta t \Delta z_p}$	$\hat{g}^{\omega_0}(t) = G_m \cdot$ $\cos(\omega_0 t - \varphi_g - \omega_0 T_{\max})$
Field solutions	$(\hat{E}_{\zeta pq}^{\omega_0})_R(P, t) = \frac{ E_{\zeta p}^{\omega_0}(P) }{J_p G_m \omega_0 \beta \Delta t \Delta z_p} \cdot$ $\cos\left(\omega_0 t - \varphi_{e\zeta p(P)} + \varphi_g - \frac{\pi}{2}\right),$ $(\hat{E}_{\zeta pq}^{\omega_0})_I(P, t) = \frac{ E_{\zeta p}^{\omega_0}(P) }{J_p G_m \omega_0 \beta \Delta t \Delta z_p} \cdot$ $\cos(\omega_0 t - \varphi_{e\zeta p(P)} + \varphi_g)$ $\zeta = x, y, z$	$\hat{E}_{\zeta pq}^{\omega_0}(P, t) = E_{\zeta p}^{\omega_0}(P) \cdot$ $\cos(\omega_0 t - \varphi_{e\zeta p(P)} - \omega_0 T_{\max}),$ $\zeta = x, y, z$

3.3.2 Summary of the self-adjoint sensitivity algorithm for S -parameters [7]

The proposed S -parameter sensitivity algorithm is summarized below.

Stage 1: System Analysis (repeat for all K ports)

- A. Set excitation of q -port guide, acquire incident field.
- B. Run time-domain simulation of structure.

Acquire outgoing field at all ports.

Record fields at perturbation grid points. (Note: the perturbation grid points are those surrounding the boundaries or material interfaces affected by a design parameter perturbation; for details, see [5].)

- C. Compute \tilde{F}_{pq} ($p = 1, \dots, K$), \tilde{F}_q , and the S_{pq} parameters.

Stage 2: Sensitivity Analysis

- A. Find G_m and φ_g through FT of $g(t)$, see (3.57).
- B. Set column index of scattering matrix, $q=1$.
- C. Set row index of scattering matrix, $p=1$.
- D. Set design parameter, $n = 1$.
- E. Find $|E_{\zeta p}^{\omega_0}|$ and $\varphi_{e\zeta p(P)}$ through FT of $E_{\zeta p}(P, t)$, $\zeta = x, y, z$, $P \in S_n$,

where S_n is the set of perturbation grid points associated with a one-cell perturbation of the shape parameter p_n .

- F. Compute the derivatives of $\text{Re} \tilde{F}_{pq}$ and $\text{Im} \tilde{F}_{pq}$ with the discretized

sensitivity expression of (3.7), discretized as

$$\frac{\partial \text{Re} \tilde{F}_{pq}}{\partial p_n} \approx -\frac{\Delta t}{\Delta p_n} \sum_{n_t=1}^{N_{\max}} \sum_{P \in S_n} \left[(\hat{\mathbf{E}}_{pq}^{\omega_0})_R^{(n_t)} \cdot \Delta_n R(\bar{\mathbf{E}}_q^{(n_t)}) \cdot \Delta x \Delta y \Delta z \right]_P, \quad (3.67)$$

$$\frac{\partial \text{Im} \tilde{F}_{pq}}{\partial p_n} \approx -\frac{\Delta t}{\Delta p_n} \sum_{n_t=1}^{N_{\max}} \sum_{P \in S_n} \left[(\hat{\mathbf{E}}_{pq}^{\omega_0})_I^{(n_t)} \cdot \Delta_n R(\bar{\mathbf{E}}_q^{(n_t)}) \cdot \Delta x \Delta y \Delta z \right]_P, \quad (3.68)$$

Here, the three (x, y, z) components of $(\hat{\mathbf{E}}_{pq}^{\omega_0})_R^{(n_t)}$ and $(\hat{\mathbf{E}}_{pq}^{\omega_0})_I^{(n_t)}$ are given by (3.65) and (3.66) with $t=n_t\Delta t$, respectively. We emphasize that these adjoint fields are entirely determined by the original-system simulation with a p -port excitation. $\bar{\mathbf{E}}_q^{(n_t)}$ is the original-system field sampled at $(P, t=n_t\Delta t)$ and produced by the simulation with a q -port excitation.

G. Compute the S_{pq} derivative using

$$\frac{\partial S_{pq}}{\partial p_n} = \sqrt{\frac{Z_q}{Z_p}} \cdot \frac{1}{\tilde{F}_q} \left(\frac{\partial \text{Re} \tilde{F}_p}{\partial p_n} + j \frac{\partial \text{Im} \tilde{F}_p}{\partial p_n} \right) \quad (3.69)$$

Compute the derivative of the magnitude and phase of S_{pq} from the derivatives of its real and imaginary parts if necessary.

H. Set next shape parameter: $n=n+1$.

If $n \leq N$ then start over at step E, else continue.

I. Set next row index of scattering matrix: $p=p+1$.

If $p \leq K$ then start over at step D, else continue.

J. Set next column of scattering matrix: $q=q+1$.

If $q \leq K$ then start over at step C, else end.

3.4 2-D Implementations with an In-house FDTD Solver

3.4.1 Metallic objects

The validation of the self-adjoint sensitivity analysis (SASA) approach is carried out through several waveguide examples. We first present a single-resonator filter example to illustrate the sensitivity computation with respect to the shape parameters of metallic objects.

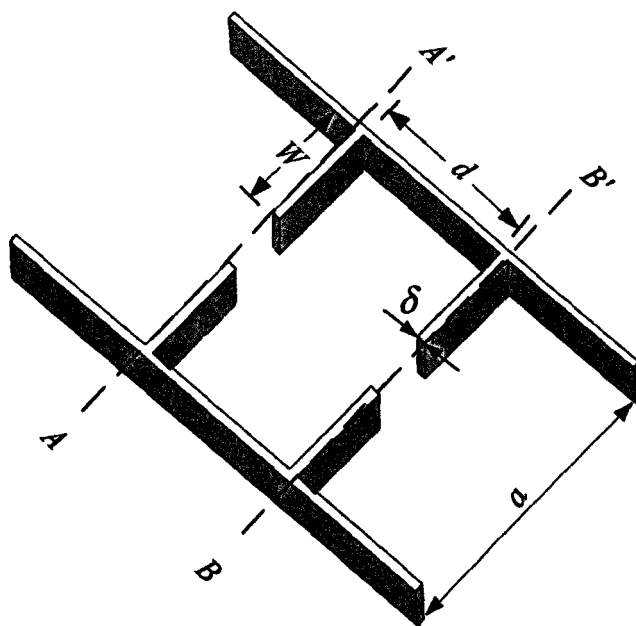


Figure 3.3 The single-resonator filter [4].

The sensitivities of this structure, shown in Figure 3.3, have been already investigated for an energy-type response with the TLM method [4]. There, an

adjoint simulation is performed since the energy response leads to an adjoint excitation whose profile across the port differs from that of the original one.

Here, we analyze the filter for its S -parameters and their sensitivities. The nominal design values of the structure are shown in Table 3.2. The simulation is performed in our FDTD-based in-house solver. We need only one simulation of the original structure to obtain all the necessary information. The FDTD simulation settings are listed as follows:

- 1) Uniform FDTD grid with $\Delta h = 0.5$ mm .
- 2) Time step is set as $\Delta t = 6.67 \times 10^{-13}$ s , such that the stability criterion is satisfied with $\Delta h / (c \cdot \Delta t) = 2.5 > \sqrt{3}$.
- 3) The simulation duration is set as $T_{max} = 6 \times 10^4 \Delta t$.
- 4) The computational domain is set as $60 \times 1 \times 200$ cells.
- 5) An 8-layer PML is applied as an absorbing boundary at the ports.

The excitation is a sine wave modulated by a Gaussian pulse for a band limited spectrum of about 2 GHz (from 3 to 5 GHz). The spatial distribution across the port is a half-sine modal distribution. The location of the excitation is 30 cells away from the PML boundary of the port.

The magnitudes of the S -parameters are plotted in Figure 3.4. They are compared with the results from HFSS. Figures 3.5 to 3.7 show the derivatives of the real and the imaginary parts as well as the magnitude of S_{11} with respect to the width W of the septum in the frequency band from 3 GHz to 5 GHz. Figures 3.8

to 3.10 show the derivatives of the real and the imaginary parts as well as the magnitude of S_{21} with respect to W . In all plots, the derivative curves obtained with our SASA approach are marked as SASA, while the curves obtained through finite differencing of the S -parameters are marked as BFD, CFD, FFD for backward, central, and forward finite differences, respectively. The SASA curves follow closely the finite-difference estimates. They match best with the central finite differences, which have higher accuracy than the forward and backward finite differences.

We compute the sensitivities in the metallization case, i.e. the forward perturbation. The perturbation points we use to compute the sensitivities with respect to the septum width W are shown in Figure 3.11. The points where the field is recorded are marked with a cross. The points denoted with a circle are those for the original field while the points marked with a square are for the adjoint field of the perturbed problem. The adjoint field is obtained through the field mapping denoted by the arrows.

Table 3.2 Nominal design values of the single-resonator filter.

Design parameter	Value (mm)
a	60
d	28
W	13
δ	1

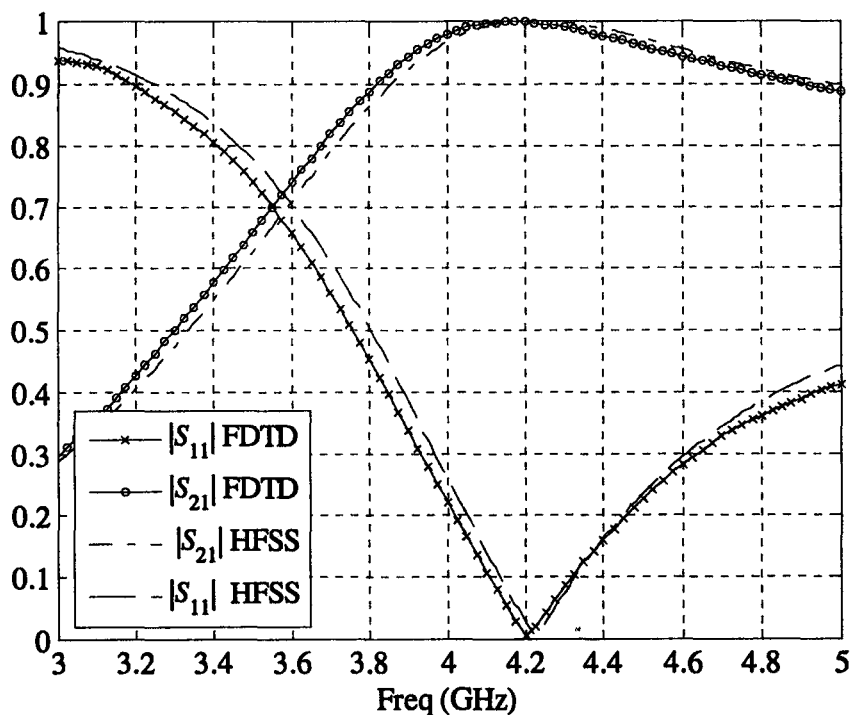


Figure 3.4 Comparison of the magnitudes of the S -parameters.

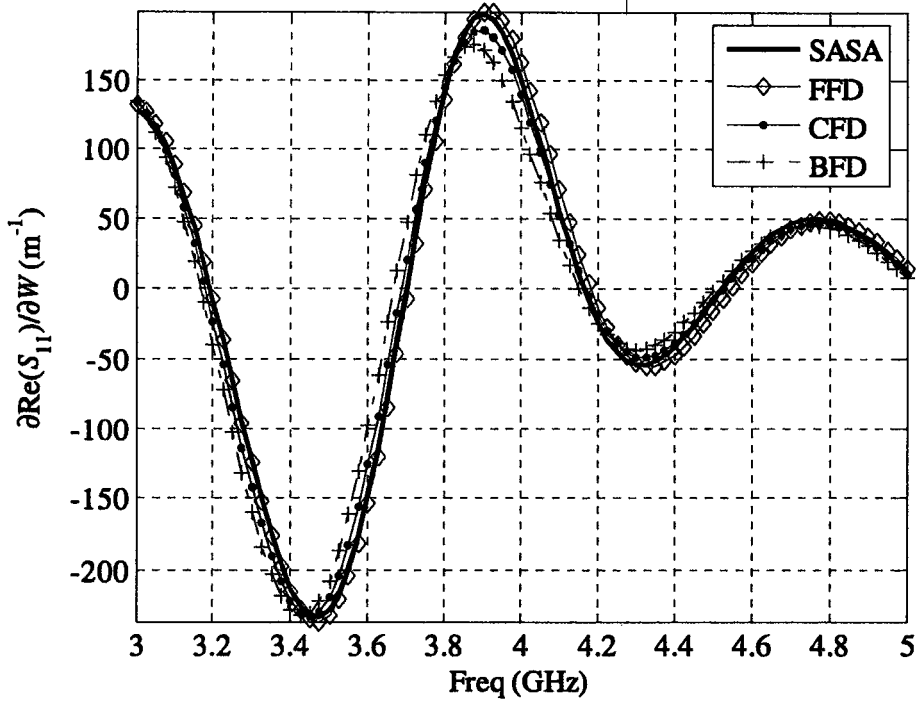


Figure 3.5 Derivative of $\text{Re}S_{11}$ with respect to the septum width W of the single-resonator filter at the nominal design $p^T = [d \ W] = [28 \ 13]$ mm.

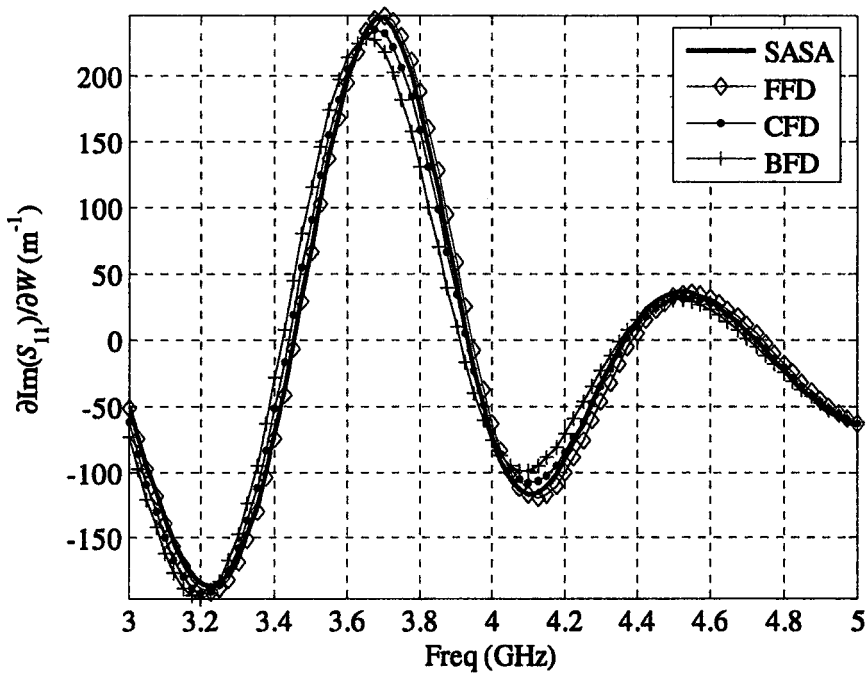


Figure 3.6 Derivative of $\text{Im}S_{11}$ with respect to the septum width W of the single-resonator filter at the nominal design $p^T = [d \ W] = [28 \ 13]$ mm.

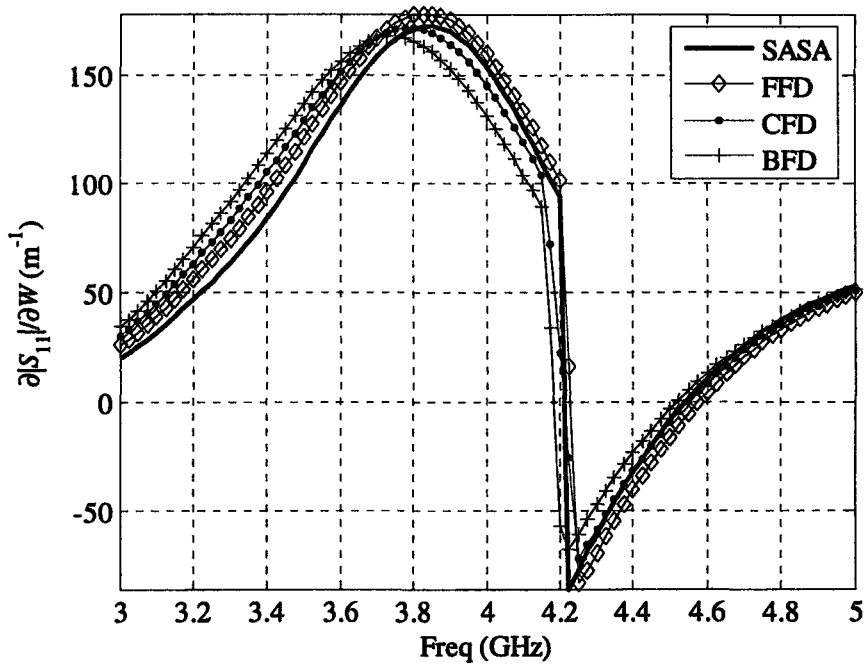


Figure 3.7 Derivative of $|S_{11}|$ with respect to the septum width W of the single-resonator filter at the nominal design $p^T = [d \ W] = [28 \ 13]$ mm.

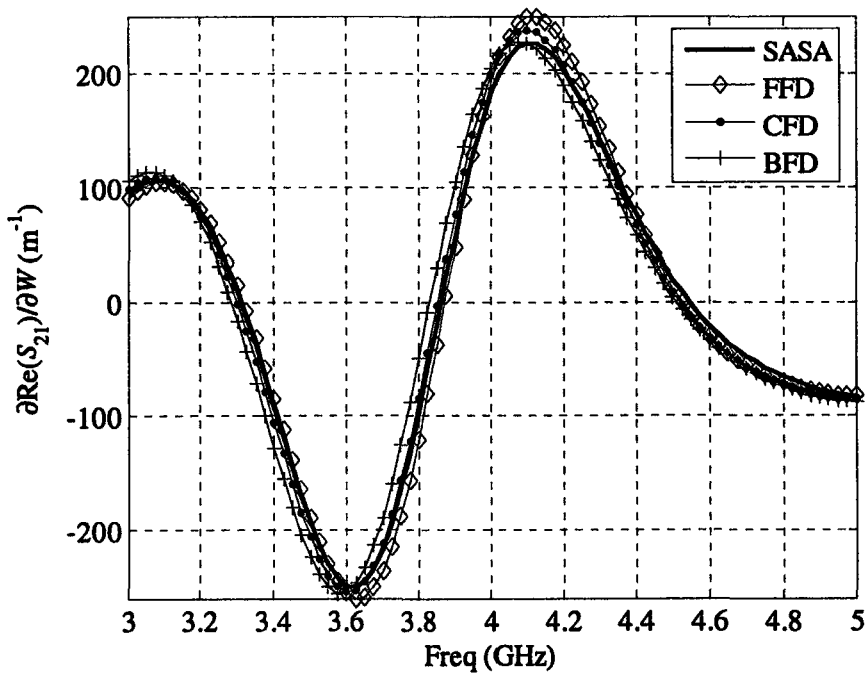


Figure 3.8 Derivative of $\text{Re}(S_{21})$ with respect to the septum width W of the single-resonator filter at the nominal design $p^T = [d \ W] = [28 \ 13]$ mm.

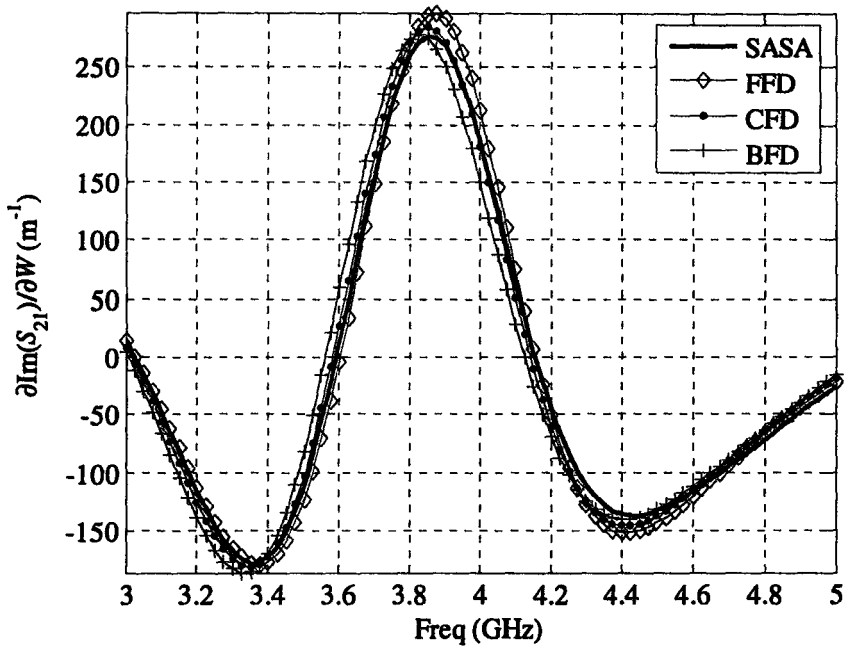


Figure 3.9 Derivative of $\text{Im}(S_{21})$ with respect to the septum width W of the single-resonator filter at the nominal design $p^T = [d \ W] = [28 \ 13]$ mm.

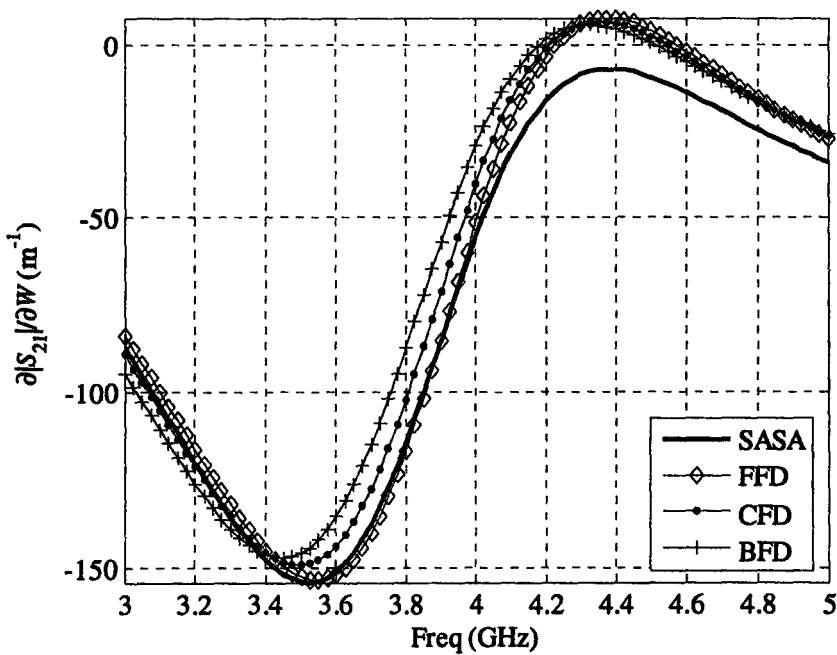


Figure 3.10 Derivative of $|S_{21}|$ with respect to the septum width W of the single-resonator filter at the nominal design $p^T = [d \ W] = [28 \ 13]$ mm.

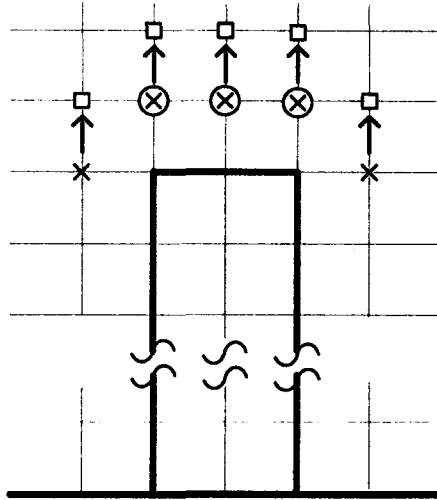


Figure 3.11 Recorded field points in the FDTD simulation. The points at which the field is recorded are marked with a cross. The original field and the adjoint field are needed at the points marked with circles and squares, respectively. The arrows denote the field mapping used to obtain the adjoint field of the perturbed problem.

3.4.2 Dielectric objects

In this example, we simulate a normally incident TEM plane wave in a lossy medium. The structure and its dimensions are shown in Figure 3.12. The host medium is vacuum and a lossy dielectric object is in it. The structure is designed to have minimal reflection at 3 GHz. Correspondingly, the length L of the lossy object is set as half of the wavelength in the lossy medium. In the lossy medium, the propagation constant is defined as

$$\gamma = j\omega\sqrt{\mu\tilde{\epsilon}} = \alpha + j\beta, \quad (3.70)$$

where $\tilde{\epsilon}$ is the complex permittivity,

$$\tilde{\epsilon} = \epsilon_0 \epsilon_r - j\sigma / \omega. \quad (3.71)$$

Here, ϵ_r , μ and σ are the relative permittivity, the permeability and the conductivity, respectively. Then, we can determine L as

$$L = \frac{\lambda}{2} = \frac{\pi}{\beta}. \quad (3.72)$$

L is computed to be 13 mm.

The simulation is performed in our FDTD in-house solver. The FDTD simulation settings are listed as follows:

- 1) Uniform FDTD grid with $\Delta h = 1$ mm.
- 2) Time step is set as $\Delta t = 1.9245 \times 10^{-12}$ s, such that the stability criterion is satisfied with $\Delta h / (v_{\max} \cdot \Delta t) > 1$. The velocity v_{\max} is equal to c here, which is the speed of light in vacuum, because the host medium is vacuum.
- 3) The simulation duration is set as $T_{\max} = 4 \times 10^4 \Delta t$.
- 4) The computational domain is set as (200×2) cells.
- 5) A 5-layer PML is applied as an absorbing boundary at the ports.

The excitation is a sine wave modulated by a Gaussian pulse for a band limited spectrum from 2.5 to 3.5 GHz. It has a uniform distribution across the port conforming to a TEM plane wave. The location of the excitation is 5 cells away from the PML boundary of the port.

The design parameters are $\mathbf{p}^T = [\epsilon_r, \sigma]$, which are the constitutive parameters of the central layer. Here, we compute the S -parameter sensitivities with respect to both the relative permittivity and the conductivity of the lossy object. Figure 3.13 shows the S -parameters, compared with the HFSS results. Figures 3.14 to 3.19 show the S_{11} and S_{21} sensitivities with respect to the relative permittivity of the middle layer. Figures 3.20 to 3.22 show the S_{11} sensitivities with respect to the conductivity of the middle layer. They show good agreement with the finite difference curves.

The recorded field points are illustrated in Figure 3.23. To simplify the figure, we assume the length L to be 3 cells. The points marked with \times are the points where we record the field for both the original and the adjoint problems.

We notice that the agreement in this lossy structure is not as good as what we obtain in the metallic object example. We attribute this to the less accurate field solutions. In FDTD, we employ the averaging scheme of the permittivity to model the interface between two materials. This introduces error, especially for the field at the interface. This may lead to degradation of the accuracy of the SASA.

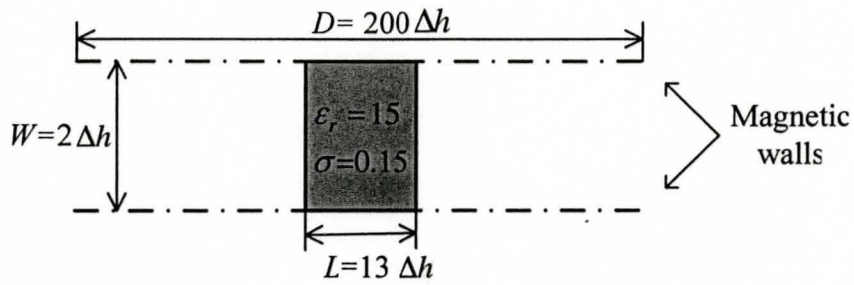


Figure 3.12 Geometry of the lossy dielectric object in vacuum.

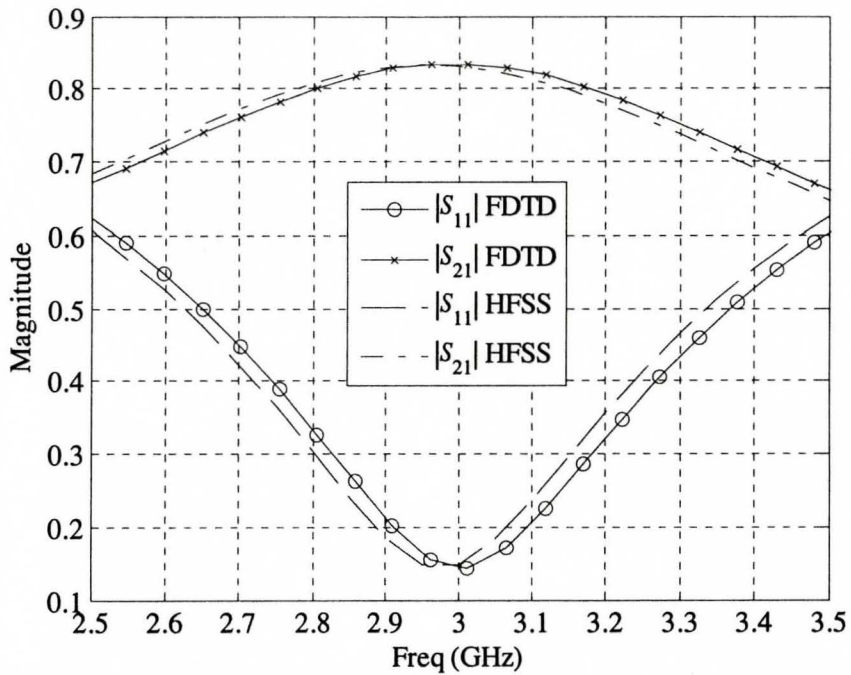


Figure 3.13 S-parameters of the structure shown in Figure 3.12.

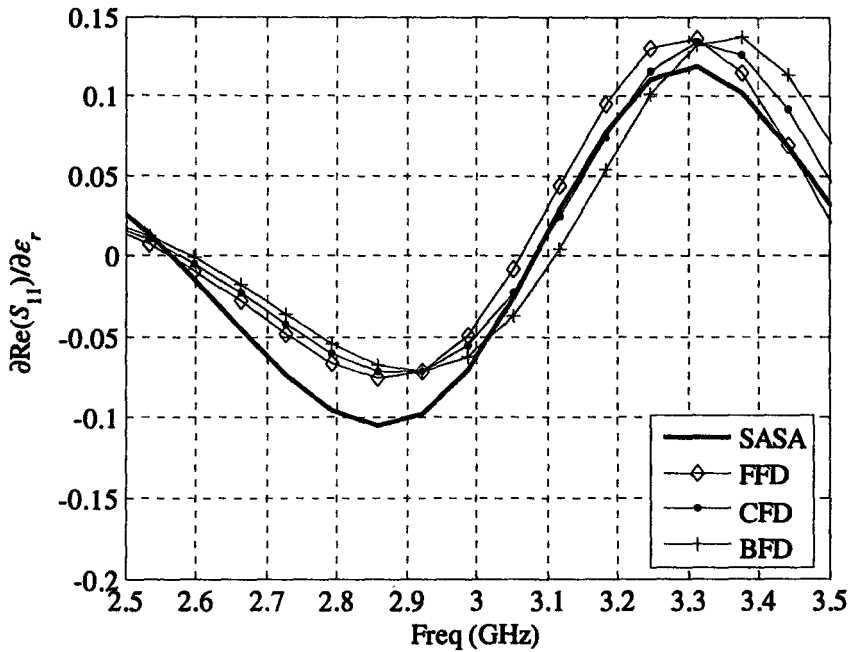


Figure 3.14 Derivative of $\text{Re}(S_{11})$ with respect to the relative permittivity ϵ_r of the central layer at the nominal design: $\epsilon_r = 15$, $\sigma = 0.15 \text{ S/m}$.

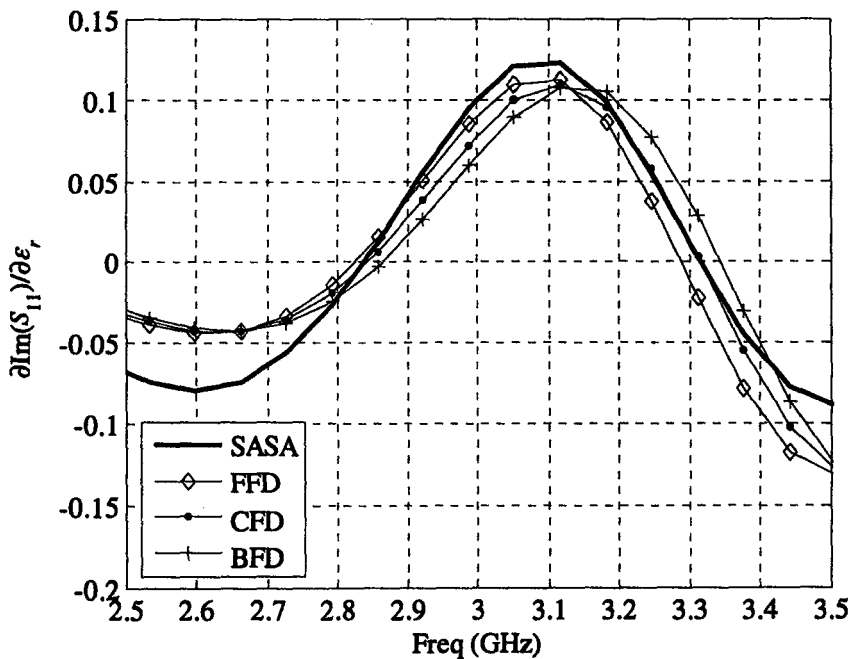


Figure 3.15 Derivative of $\text{Im}(S_{11})$ with respect to the relative permittivity ϵ_r of the central layer at the nominal design: $\epsilon_r = 15$, $\sigma = 0.15 \text{ S/m}$.

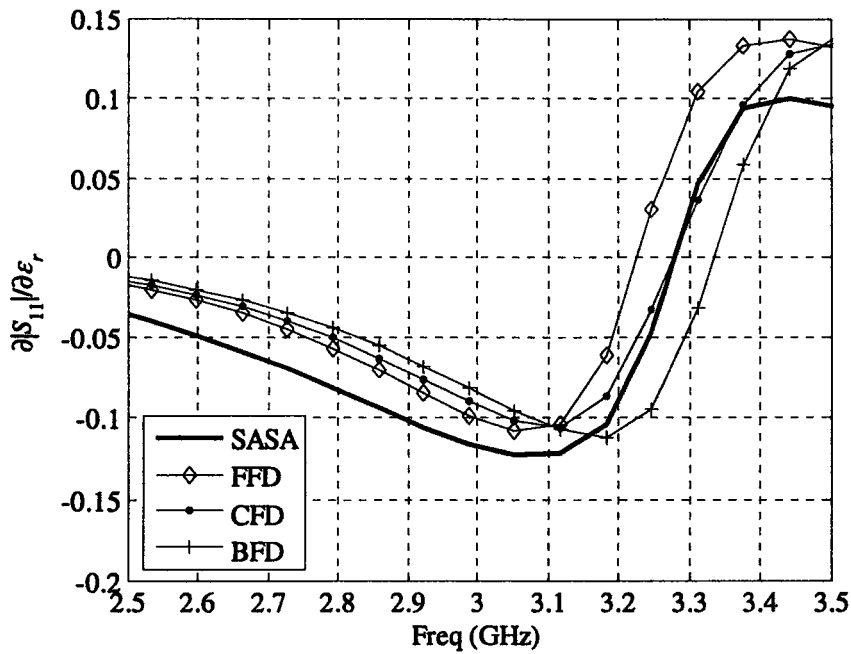


Figure 3.16 Derivative of $|S_{11}|$ with respect to the relative permittivity ϵ_r of the central layer at the nominal design: $\epsilon_r = 15$, $\sigma = 0.15$ S/m.

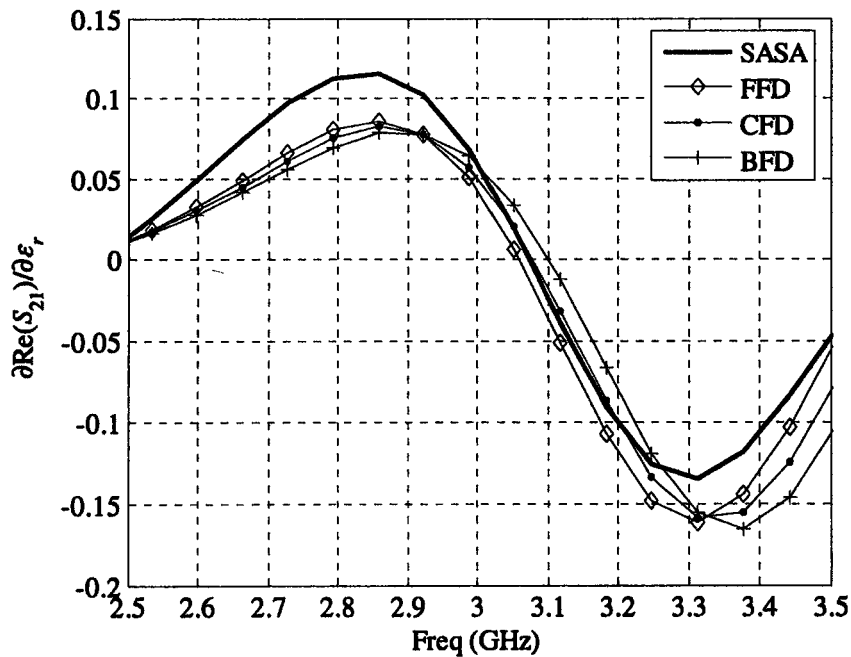


Figure 3.17 Derivative of $\text{Re}(S_{21})$ with respect to the relative permittivity ϵ_r of the central layer at the nominal design: $\epsilon_r = 15$, $\sigma = 0.15$ S/m.

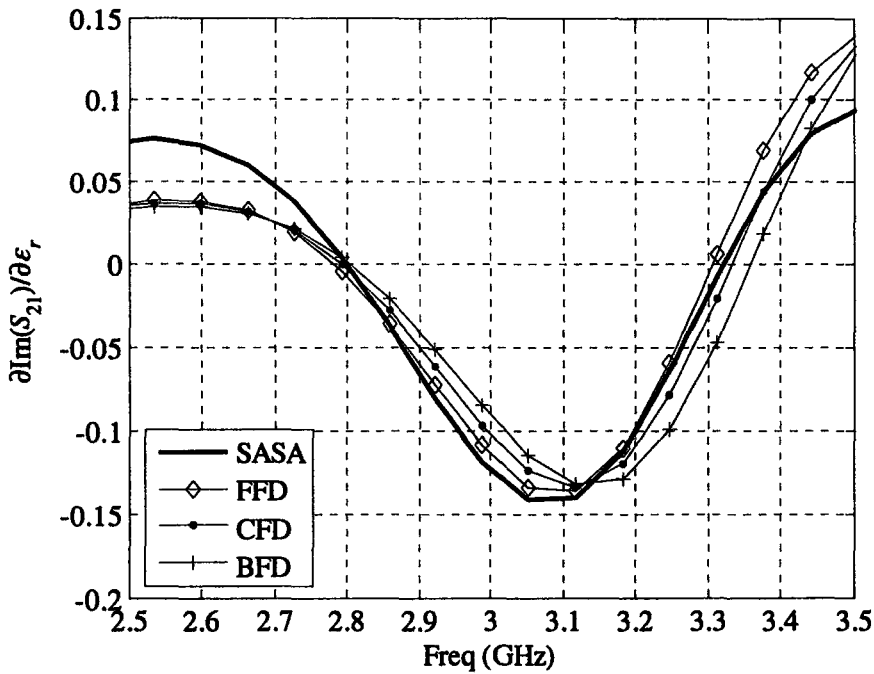


Figure 3.18 Derivative of $\text{Im}(S_{21})$ with respect to the relative permittivity ϵ_r of the central layer at the nominal design: $\epsilon_r = 15$, $\sigma = 0.15 \text{ S/m}$.

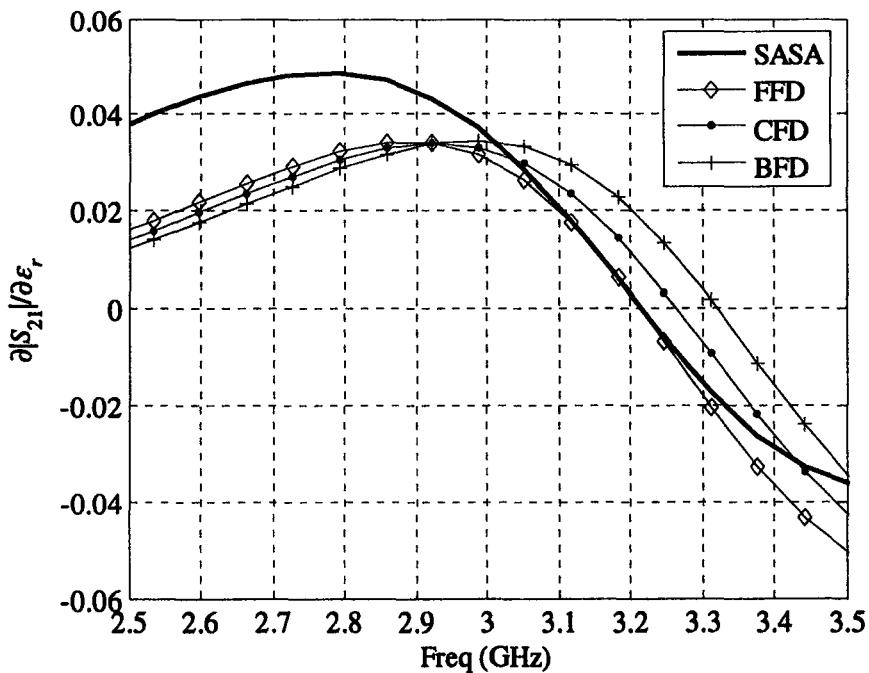


Figure 3.19 Derivative of $|S_{21}|$ with respect to the relative permittivity ϵ_r of the central layer at the nominal design: $\epsilon_r = 15$, $\sigma = 0.15 \text{ S/m}$.

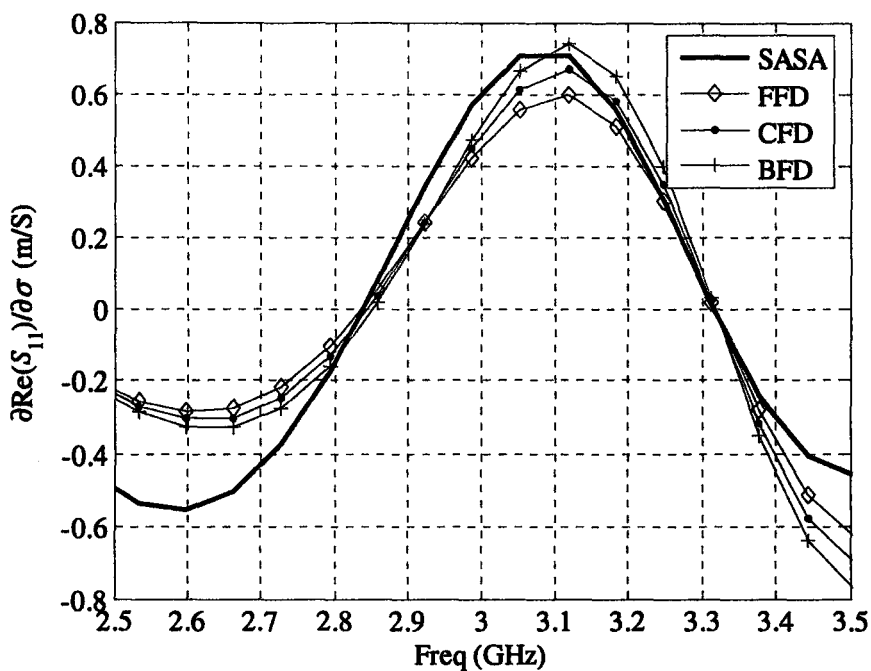


Figure 3.20 Derivative of $\text{Re}(S_{11})$ with respect to the conductivity σ of the central layer at the nominal design: $\epsilon_r = 15$, $\sigma = 0.15$ S/m.

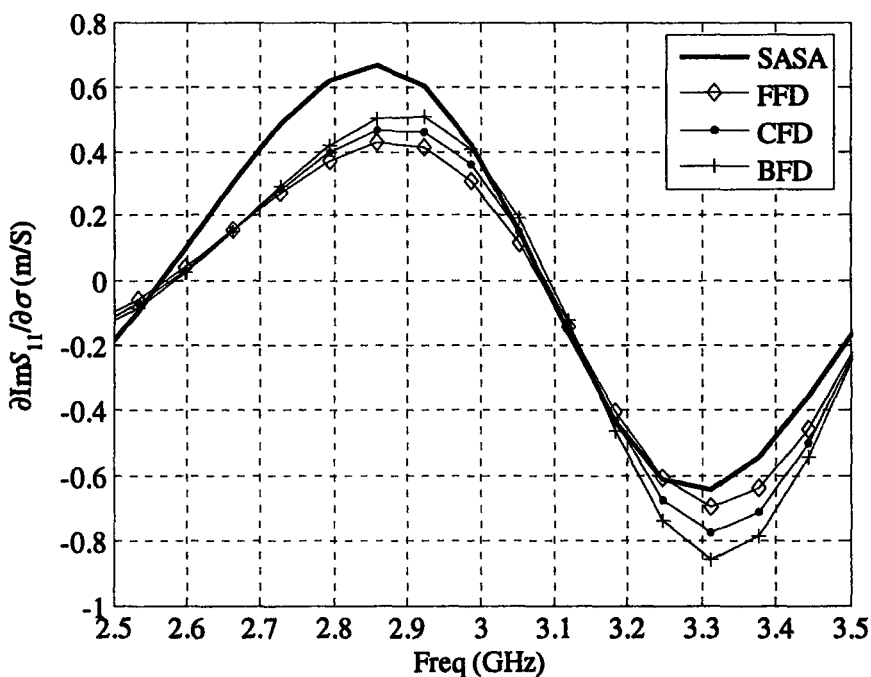


Figure 3.21 Derivative of $\text{Im}(S_{11})$ with respect to the conductivity σ of the central layer at the nominal design: $\epsilon_r = 15$, $\sigma = 0.15$ S/m.

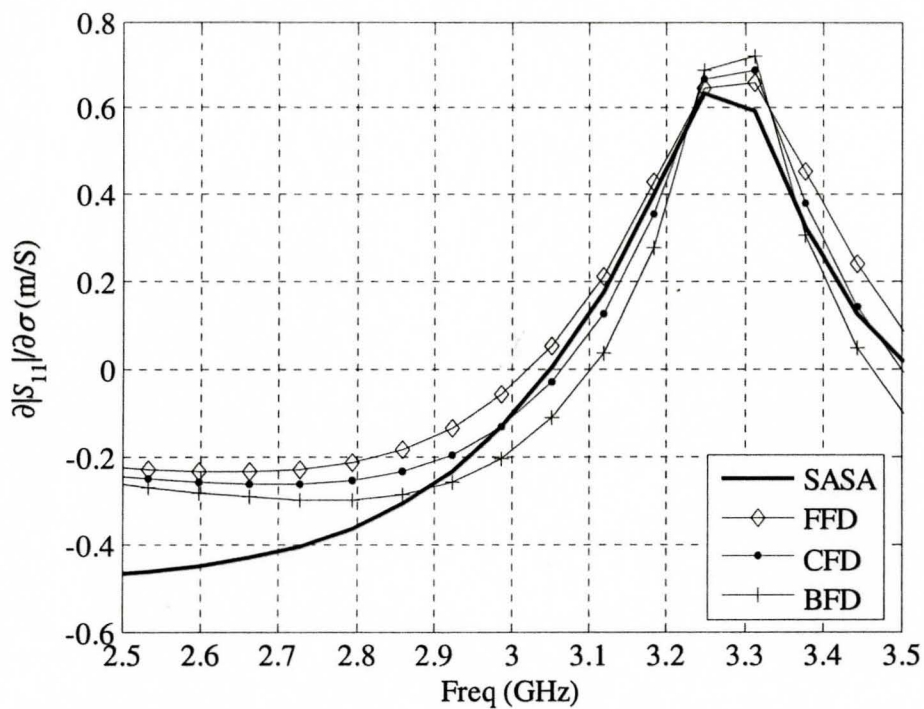


Figure 3.22 Derivative of $|S_{11}|$ with respect to the conductivity σ of the central layer at the nominal design: $\epsilon_r = 15$, $\sigma = 0.15$ S/m.

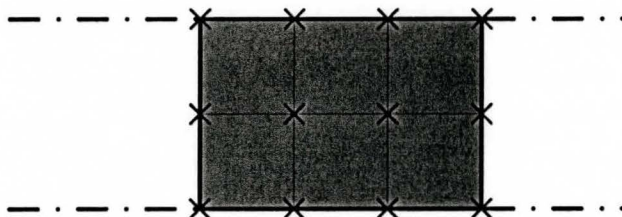


Figure 3.23 The recorded points in simulation. The points with marks are the points where we record the field for both the original and the adjoint E-field.

3.5 Summary

In this chapter, we first review the theory of the AVM with time-domain EM numerical methods. We focus on the adjoint system formulation and the computation of the system coefficient derivatives. Then, we present a detailed derivation of the SASA method and give the algorithm for the S -parameter sensitivity computation. Metallic and dielectric object examples validate the SASA method. In the examples, we compute the S -parameter sensitivities with respect to shape and constitutive parameters and achieve good agreement.

Here, all the field solutions are obtained from an in-house FDTD solver. In the next chapter, we implement the SASA algorithm with one of the existing time-domain FDTD solvers, XFDTD v. 6.3.

3.6 References

- [1] E. J. Haug, K. K. Choi and V. Komkov, *Design Sensitivity Analysis of Structural Systems*. Academic Press Inc., Harcourt Bruce Jovanovich Publishers, Orlando, Florida, 1986.
- [2] Y. Chung, C. Cheon, I. Park, and S. Hahn, "Optimal shape design of microwave device using FDTD and design sensitivity analysis," *IEEE*

- Trans. on Microwave Theory Tech.*, vol. 48, no. 12, pp. 2289-2296, December 2000.
- [3] N. K. Nikolova, "Sensitivity analysis with EM solvers on structured grids: the FDTD case," Computational Electromagnetics Research Laboratory presentation, December 2004.
- [4] M. H. Bakr and N. K. Nikolova, "An adjoint variable method for time domain TLM with fixed structured grids," *IEEE Trans. Microwave Theory Tech.*, vol. 52, pp. 554-559, February 2004.
- [5] N. K. Nikolova, H. W. Tam, and M. H. Bakr, "Sensitivity analysis with the FDTD method on structured grids," *IEEE Trans. Microwave Theory Tech.*, vol. 52, pp. 1207-1216, April 2004.
- [6] J. C. Strikwerda, *Finite Difference Schemes and Partial Differential Equations*. Pacific Grove, California: Wadsworth & Brooks, 1989, Chapter 3.
- [7] N. K. Nikolova, Ying Li, Yan Li, M. H. Bakr, "Sensitivity analysis of scattering parameters with electromagnetic time-domain simulators," *IEEE Trans. Microwave Theory Tech.*, vol. 54, pp. 1598-1610, April 2006.
- [8] M. H. Bakr and N. K. Nikolova, "An adjoint variable method for time domain TLM with fixed structured grids," *IEEE Trans. Microwave Theory Tech.*, vol. 52, pp. 554-559, Feb. 2004.

- [9] Ying Li, Yan Li, N. K. Nikolova, and M. H. Bakr, “Time domain sensitivity analysis of lossy dielectric structures,” *Frontiers in Applied Computational Electromagnetics*, June 2006.
- [10] Y. Qian, T. Itoh, *FDTD Analysis and Design of Microwave Circuits and Antennas*. Realize Inc.1999, Chapter. 4.
- [11] N. Marcuvitz, *Waveguide Handbook*. London, UK: Peter Peregrinus Ltd., 1993 reprint, Chapter 2.
- [12] D. Pozar, *Microwave Engineering*, Addison Wesley Publishing Company Inc., USA, 1993.

Chapter 4

THE FDTD S-PARAMETER SENSITIVITY ANALYSIS WITH COMMERCIAL SIMULATORS

4.1 Introduction

The commercial software packages for the simulation and design of high frequency (HF) structures use either time-domain or frequency-domain analysis techniques. For example, the full wave electromagnetic (EM) solver XFDTD 6.3 from Remcom Inc. [1], and the EM simulation package FIDELITY 3.0 from Zeland Software Inc. [2] use the Finite-Difference Time-Domain (FDTD) method. The MEFiSTo-3D Pro™ from Faustus Scientific Corporation [3] uses the Transmission Line Method (TLM). The HF structure simulator Ansoft HFSS from Ansoft Corporation [4], and the modeling package COMSOL Multiphysics 3.2 from COMSOL [5] Inc. use the Finite Element Method (FEM). The planar EM field simulator Agilent Momentum from Agilent Technologies [6], Sonnet *em* from Sonnet Software Inc. [7], Ansoft Ensemble from Ansoft Corporation [4], and FEKO from EM Software & Systems-S.A. (Pty) Ltd. [8] are based on the Method

of Moment (MOM). The 3-D and the planar EM simulators can provide a variety of highly flexible, feature-rich, customized systems for the design of complex 3-D geometries or 2-D planar HF structures.

Some of the software packages also include an optimization module to facilitate the design of HF structures. The pioneering HF computer-aided design (CAD) packages featuring optimization capabilities were OSA90/hope™ [9], Empipe™ [10], Empipe3D™ [11] offered by the Optimization Systems Associates Inc. Even though optimizers are now available in most of the commercial HF CAD packages, none of these packages is equipped with analysis tool providing sensitivity information for the response of the structure. They approximate the objective functions using linear or quadratic interpolation over a set of data points. From the interpolated function, the gradient of the response is obtained. Such practice leads to significant computational time when the number of design variables is large. For examples, n design variables need $n+1$ simulations to compute the derivatives of the response function with respect to each design variable by the forward or backward finite-difference method. This significant limitation is overcome in the adjoint variable method (AVM) and the self-adjoint sensitivity analysis (SASA) for response sensitivity analysis developed here.

In this chapter, we investigate the feasibility of implementing the SASA technique with one of the commercial FDTD simulators, XFDTD v. 6.3. We find that the only requirement for the simulator is the ability to export the

time-dependent field solution at user-defined points. Most commercial solvers have this ability, which makes our approach readily applicable to practical optimization problems and to tolerance analysis. The SASA approach is verified through 2-D examples using the commercial simulator XFDTD v. 6.3.

4.2 Settings in XFDTD

A brief review of the XFDTD settings is presented in this section. General setting information can be found in [12], and here, we focus on the settings for the waveguide structure simulations.

4.2.1 Simulation mode

For many waveguide structures, the field of the dominant mode is not dependent on the vertical direction. We can simulate such structures in a 2-D mode, which saves time without sacrificing the accuracy. In XFDTD, the structure is simulated automatically in a 3-D mode and there is no separate option for a 2-D simulation. In order to perform a 2-D simulation in XFDTD, we need to set the grid size in the vertical direction as 1 cell under the Mesh tab. We use the single-resonator filter as an example to illustrate the setting. The structure is shown in Figure 4.1, in which z is set as the vertical direction. Figure 4.2 shows the mesh setting for a 2-D simulation. Once we set the grid size in the z direction as 1 cell, a warning window pops up reminding us that a 2-D simulation

is assumed and the upper and lower boundaries are set to be perfect conducting walls automatically.

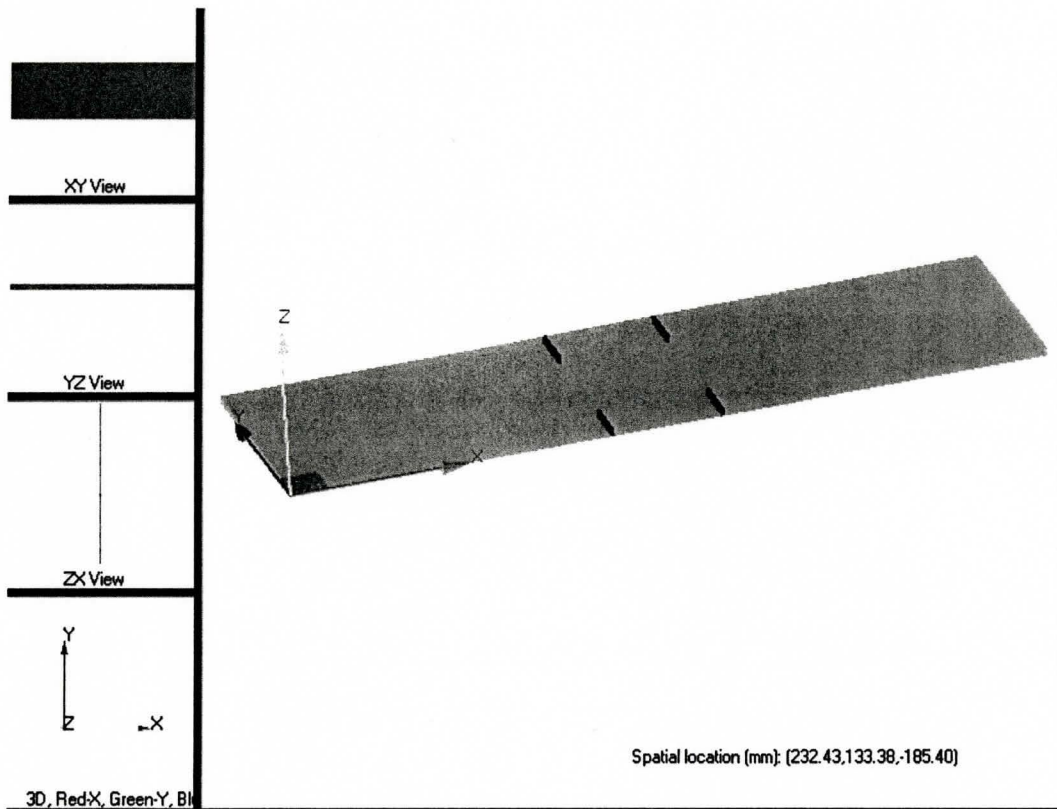


Figure 4.1 The single-resonator filter viewed in the editing window in XFDTD.

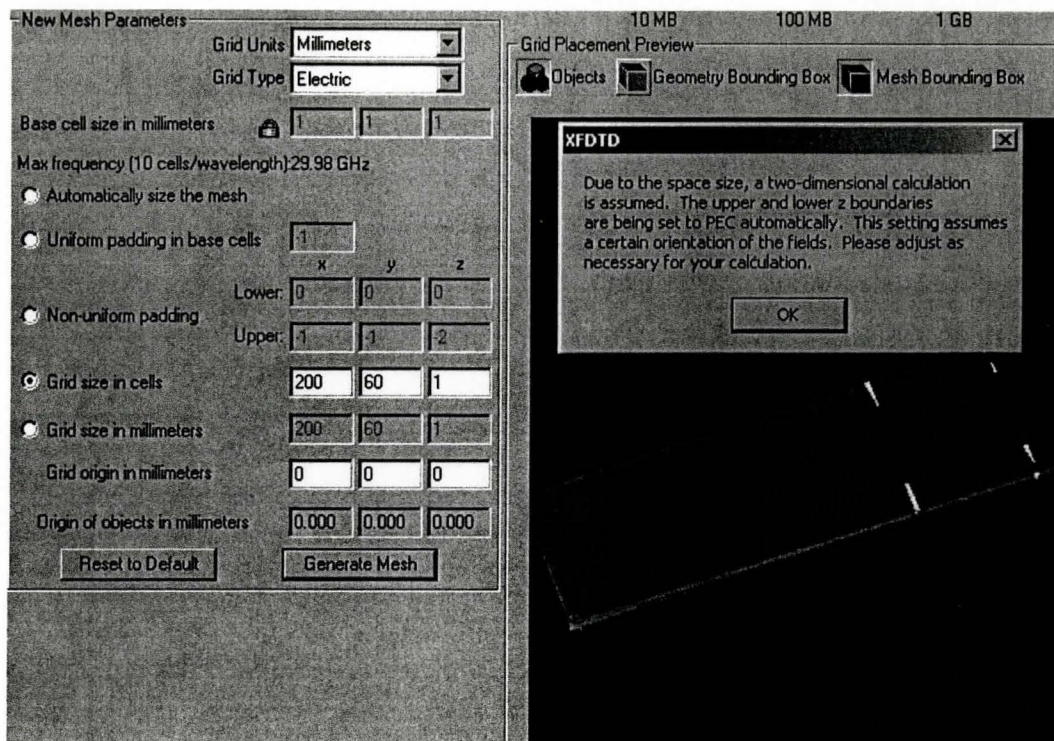


Figure 4.2 The mesh setting for a 2-D simulation.

4.2.2 Excitation

There are three main choices for the excitation in XFDTD: discrete source, plane wave and Gaussian beam as shown in Figure 4.3. We usually use the discrete source as the excitation for the S -parameter computation of the waveguide structures.

A discrete source is a cell edge on which the electric field is modified by the addition of some type of input waveform. The cell edge can be modified to behave like a voltage or a current source. The current source is a preferable choice. The problem with the voltage source is that when the source pulse

duration ends, the voltage source acts as a short circuit, which leads to substantial reflection. After selecting the parallel current source, we set the impedance associated with this source to be zero, as shown in Figure 4.4.

In order to excite the desired mode of the waveguide structure, we need to use several discrete sources conforming to the corresponding field spatial distribution. For example, in the single-resonator filter simulation, we use five evenly placed discrete current sources to represent a half-sine modal distribution as shown in Figure 4.5.

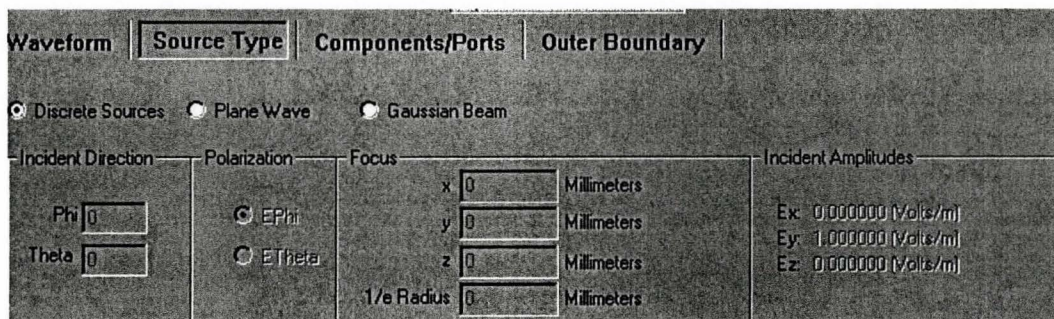


Figure 4.3 Three types of sources in XFDTD.

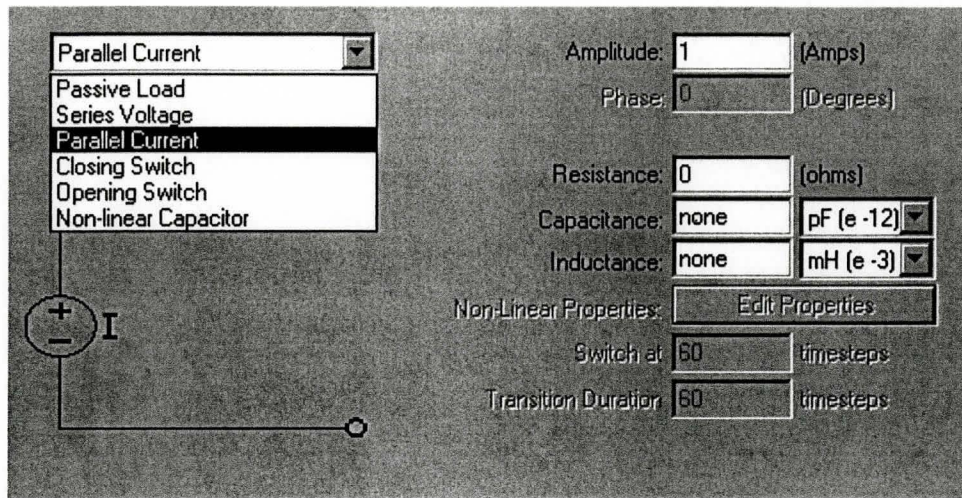


Figure 4.4 Current or voltage sources in XFDTD.

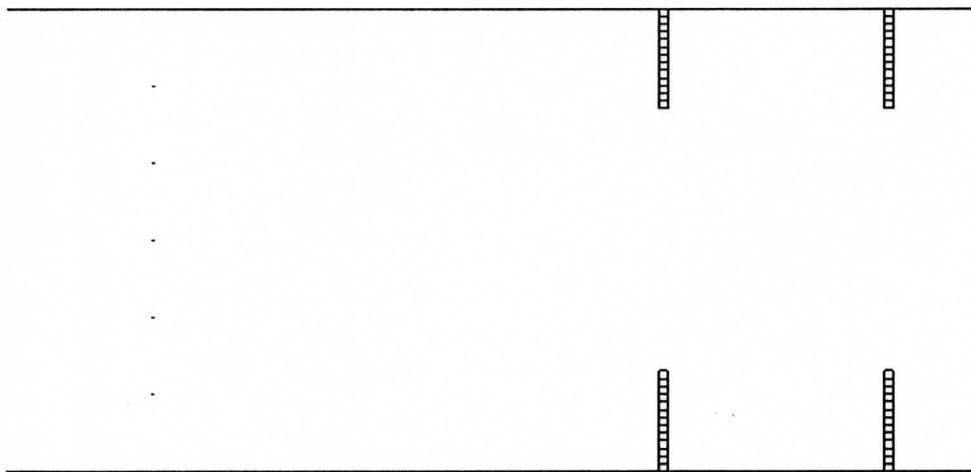


Figure 4.5 The five excitation points for the simulation of the single-resonator filter.

4.2.3 Boundaries and simulation time

The boundary conditions have to be set properly, or undesired reflections and unstable calculations may occur. There are four types of boundaries available in XFDTD as shown in Figure 4.6: perfect electrical conductor (PEC), perfect magnetic conductor (PMC), Liao absorbing boundary and perfectly matched layer (PML). The last two types are absorbing boundaries.

Although theoretically PML works better than Liao when the number of layers is set properly, we find in our simulations that Liao boundary works well in the waveguide structure while PML does not, no matter how many layers we choose.

The PMC boundary is useful when the geometry is symmetric. The computational domain can be reduced in half by employing the PMC boundary.

The simulation time has to be set long enough to let the propagating wave establish well and the field decay completely in the whole structure. We can check the time-domain waveform at an arbitrary point to ensure this.

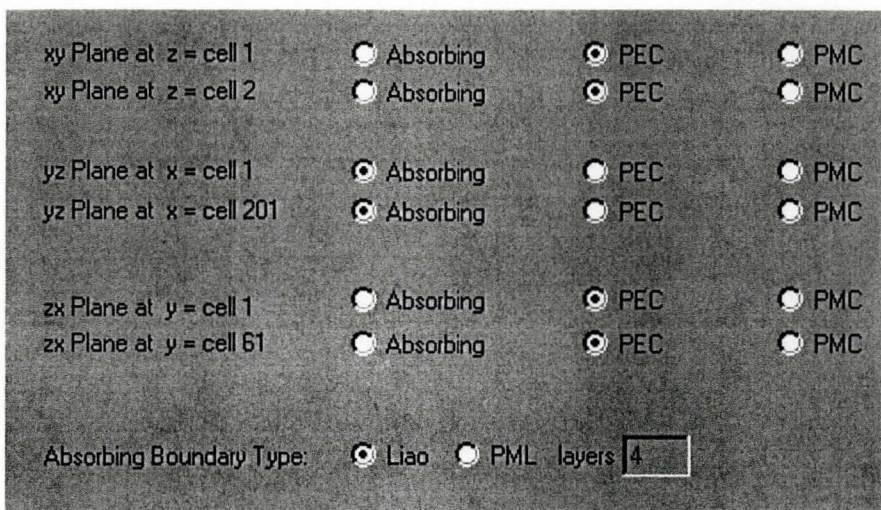


Figure 4.6 The outer-boundary section.



Figure 4.7 The reference structure for the *S*-parameter computation.

4.2.4 Data export

For the sensitivity computation, we need the field values around the perturbation area. Although there is no direct data exporting option in XFDTD,

we can easily access the files containing the field values saved at every time step. The files are saved in the same directory as the project files. A typical name for the near-zone data file might be 'filterEZT.x00011.y00020.z00005.g0'. Embedded in this filename is information that specifies exactly what data is contained within. In this example, the z component of the total E field (EZT) is saved from cell location (11, 20, 5) in the main FDTD grid (g0) of the 'filter' project. Such name format facilitates importing the data into MATLAB® [13].

4.3 Implementations with XFDTD

To compute the S -parameter sensitivities, the first task is to obtain the accurate S -parameters. Because the settings for the S -parameter computation in XFDTD are not suitable for waveguide structures, we resort to finding the S -parameters by two system analyses. One is for the structure which has the same dimensions as the input port of the investigated structure, but without any discontinuities. The other is the actual structure we are interested in. The first simulation is used to obtain the incident field. For the single-resonator filter example, the reference and the investigated structures simulated in XFDTD are shown in Figure 4.7 and Figure 4.1, respectively. With the data from XFDTD, the S -parameters are computed as

$$S_{11}(f) = \frac{\tilde{V}_1(f) - \tilde{V}_{1ref}(f)}{\tilde{V}_{1ref}(f)} \quad (4.1)$$

$$S_{21}(f) = \frac{\tilde{V}_2(f)}{\tilde{V}_{1ref}(f)} \quad (4.2)$$

where $\tilde{V}_1(f)$, $\tilde{V}_2(f)$, $\tilde{V}_{1ref}(f)$ are the Fourier transforms of the total recorded voltage at port 1, the voltage at port 2 and the incident voltage of the reference structure at port 1.

Before the simulation, we have to select all perturbation grid points at which the field is recorded and exported as required by the SASA algorithm in the Save Near-Zone Data tab in XFDTD, as shown in Figure 4.8. With the so obtained S -parameters and field values, we proceed to the SASA algorithm implemented in MATLAB.

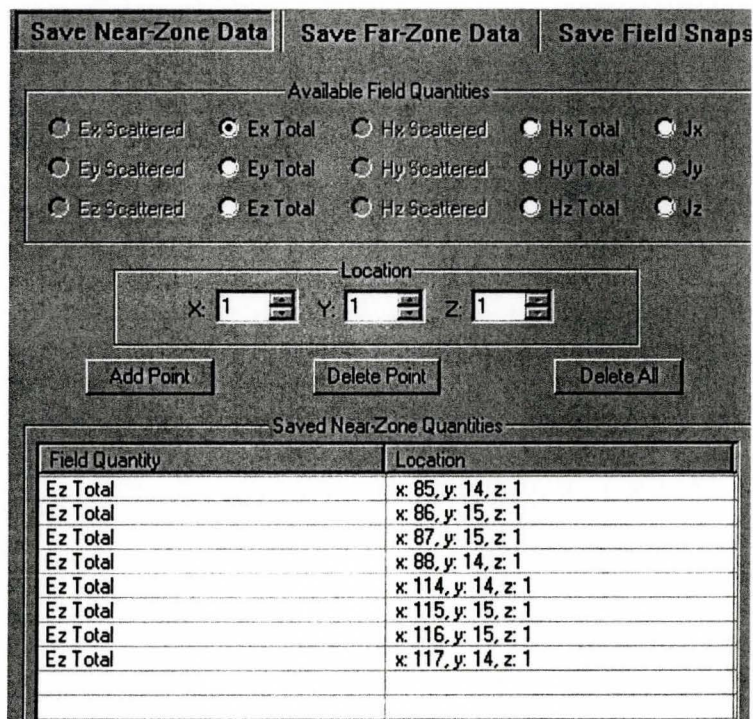


Figure 4.8 Select the perturbation field points in XFDTD.

4.4 Examples

We present two examples, the single-resonator filter and the H-plane filter, to validate the SASA algorithm with XFDTD. The detailed settings in XFDTD are presented. In all plots, the derivative curves obtained with our SASA approach are marked as SASA, while the curves obtained through parameter perturbations and finite differencing of the S -parameters are marked as BFD, CFD and FFD for backward, central, and forward finite differences, respectively.

4.4.1 Single-resonator filter

The single-resonator filter has been investigated with the in-house solver in Chapter 3. Here, we compute the S -parameter sensitivities with respect to another design parameter, d , the distance between the two septa. The single-resonator filter shown in Figure 4.9 has the dimensions $(200 \times 60 \times 1)$ mm. The septa are placed symmetrically in the waveguide. Their thickness is one cell, which is $\Delta h = 1$ mm. The design parameters are $p = [d \ W]^T$ and we compute the derivatives at the nominal values $[d \ W] = [28 \ 13]$, both in millimeters.

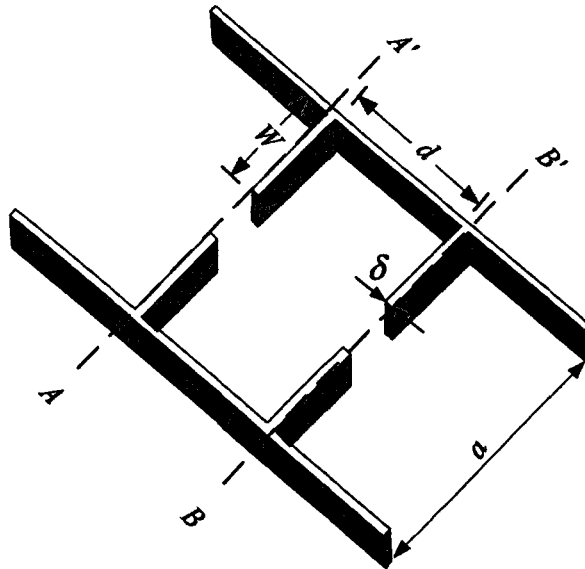


Figure 4.9 The single-resonator filter.

The details of the settings in XFDTD 6.3 are:

1. Constants: $\Delta h = 1$ mm, $\Delta t = 1.926$ ps and $q = \Delta h / (c\Delta t) = 1.7301$, which is close to $\sqrt{3} = 1.7321$.
2. Excitation: The structure is excited with a modulated Gaussian pulse whose spectrum is from 3 GHz to 5 GHz and has 600 time steps in the time domain. We use 5 probes placed uniformly along the excitation plane to form a half-sinusoidal modal distribution. The location of the excitation plane is 20 cells away from the absorbing boundary.
3. Ports: We record the field 15 spatial steps away from the excitation plane for the input port and 35 steps away from the absorbing boundary for the output. These field values are used to calculate the

S-parameters.

4. Computational domain: We set one cell in the z direction to run a 2D simulation in XFDTD and we use the Liao absorbing boundaries at the ports. The simulation time is 40000 time steps.

The magnitudes of the *S*-parameters are plotted in Figure 4.10. They are compared with the results from HFSS. The derivatives of the *S*-parameters with respect to the design parameters d are estimated using the SASA method and compared with the finite-difference method. Figures 4.10 to 4.15 show the derivatives of the real and the imaginary parts as well as the magnitudes of S_{11} and S_{21} with respect to d . We also implement the de-metallization method to compute the sensitivities of the *S*-parameters with respect to d for comparison. They show little difference compared with the results in the metallization case. The differences between them are shown in Figure 4.17 .

We find that the results from our SASA method match well with those from the finite differences. They match best with the central finite difference, which has higher accuracy than the forward and backward finite differences. The comparison between metallization and de-metallization shows that both methods yield the same results. In fact, the points we need to record are the same in both cases; the only difference is in which points relate to the original field and which to the adjoint field. The points where the field is recorded when computing the sensitivities with respect to d are the points marked with a cross in Figures 4.17 and 4.18. The points denoted with a circle are those for the original

field while the points marked with a square are for the adjoint field of the perturbed problem. The arrows denote the field mapping we use to obtain the adjoint field.

In summary, when our approach is used, it does not matter what direction of the perturbation is chosen. This holds for both metallic and dielectric structure details.

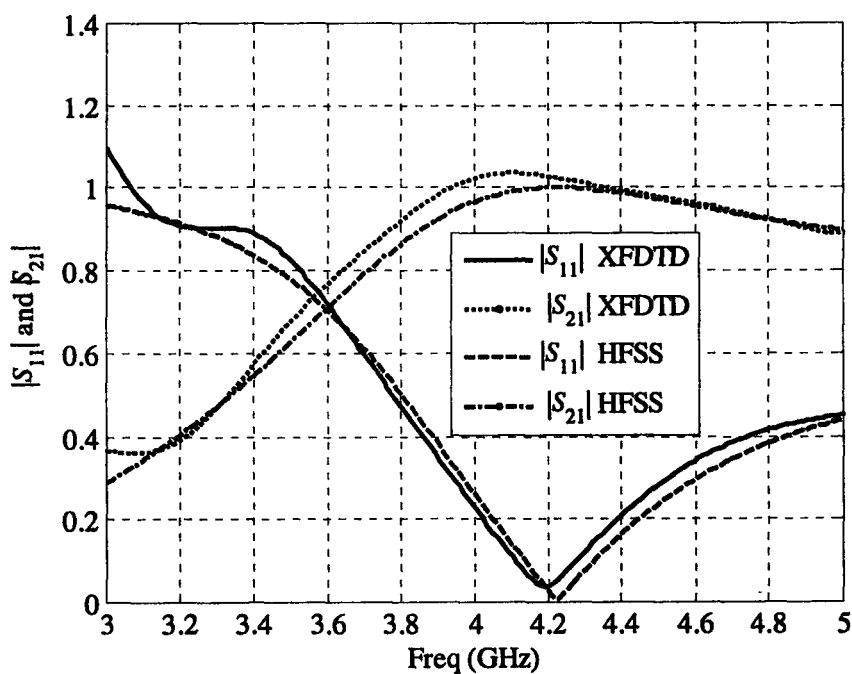


Figure 4.10 The S -parameters of the single-resonator filter ($\Delta h = 1$ mm).

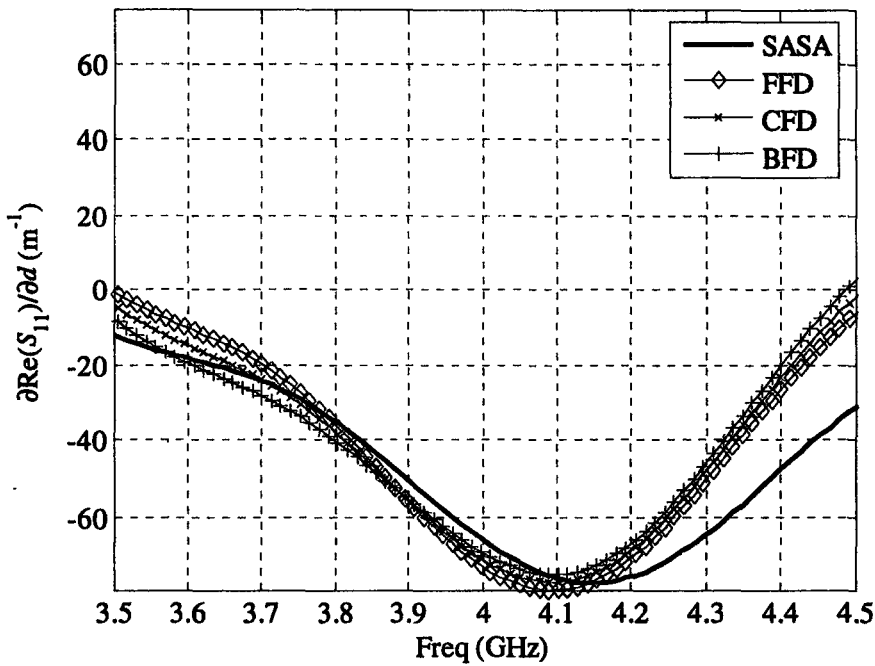


Figure 4.11 Derivative of $\text{Re}(S_{11})$ with respect to d over a sweep of frequencies for $[d W] = [28\Delta h \ 13\Delta h]$ using metallization.

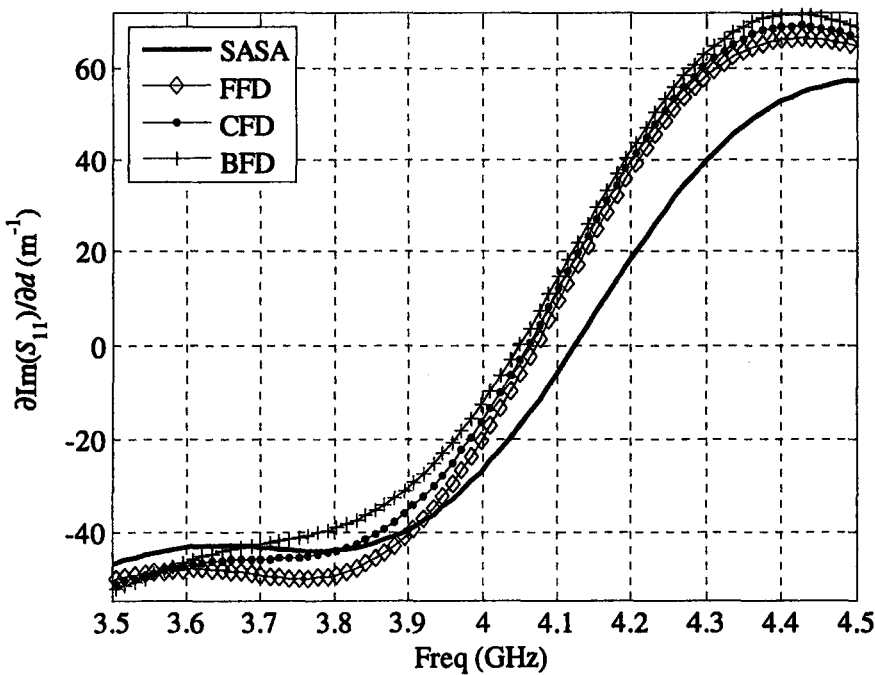


Figure 4.12 Derivatives of $\text{Im}(S_{11})$ with respect to d over a sweep of frequencies for $[d W] = [28\Delta h \ 13\Delta h]$ using metallization.

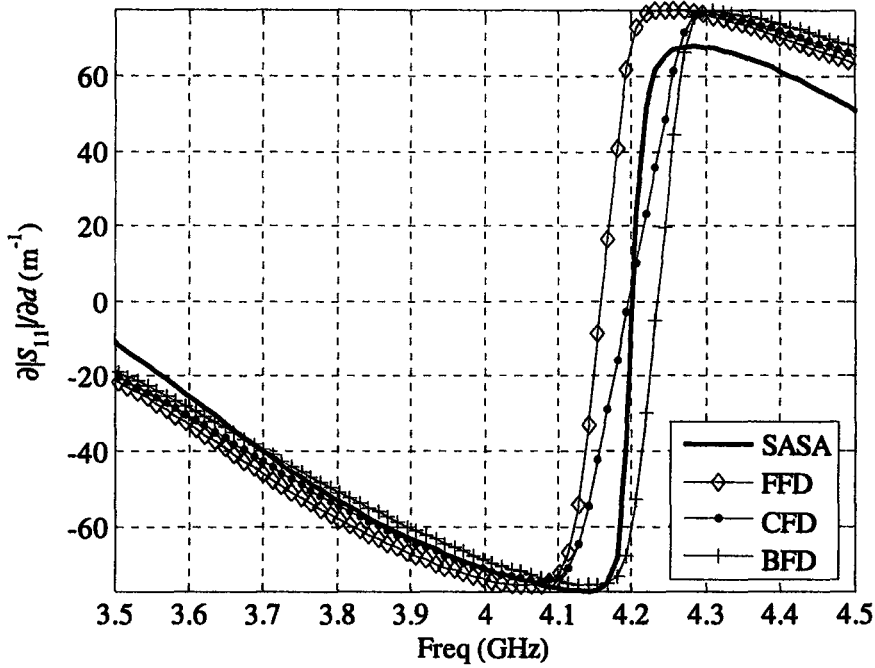


Figure 4.13 Derivatives of $|S_{11}|$ with respect to d over a sweep of frequencies for $[d W] = [28 \Delta h \ 13 \Delta h]$ using metallization.

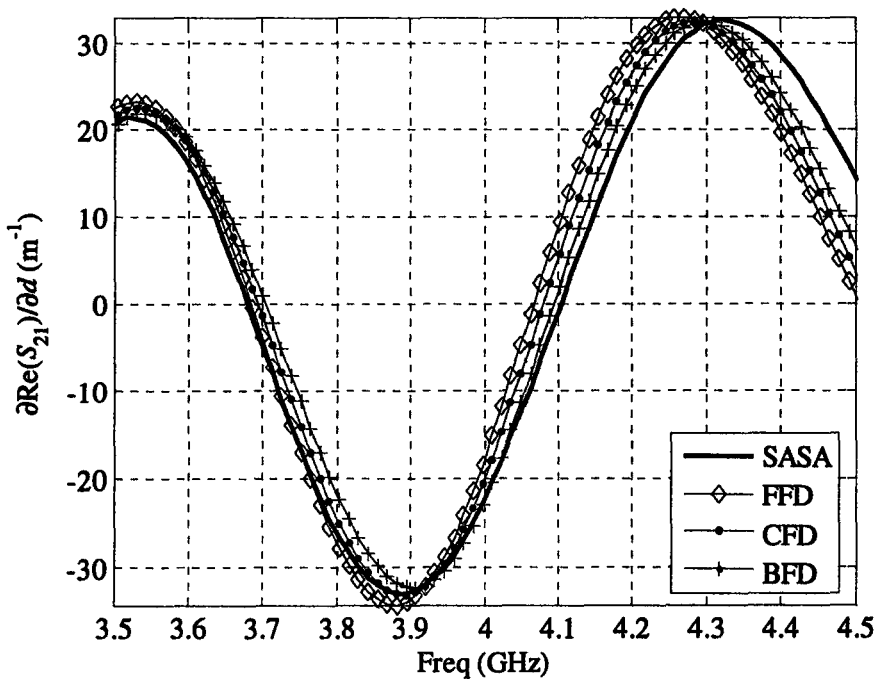


Figure 4.14 Derivatives of $\text{Re}(S_{21})$ with respect to d over a sweep of frequencies for $[d W] = [28 \Delta h \ 13 \Delta h]$ using metallization.

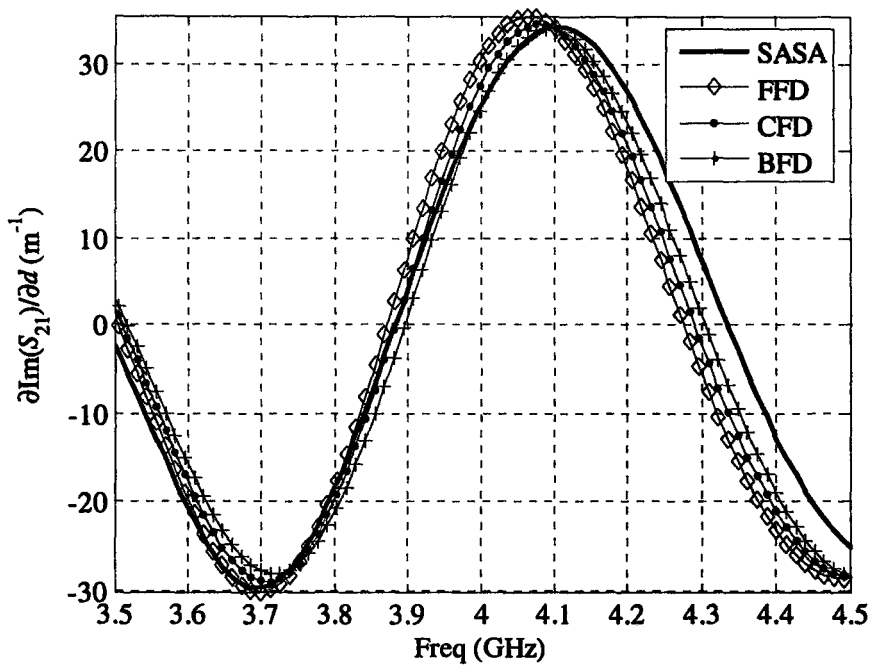


Figure 4.15 Derivatives of $\text{Im}(S_{21})$ with respect to d over a sweep of frequencies for $[d W] = [28 \Delta h \ 13 \Delta h]$ using metallization.

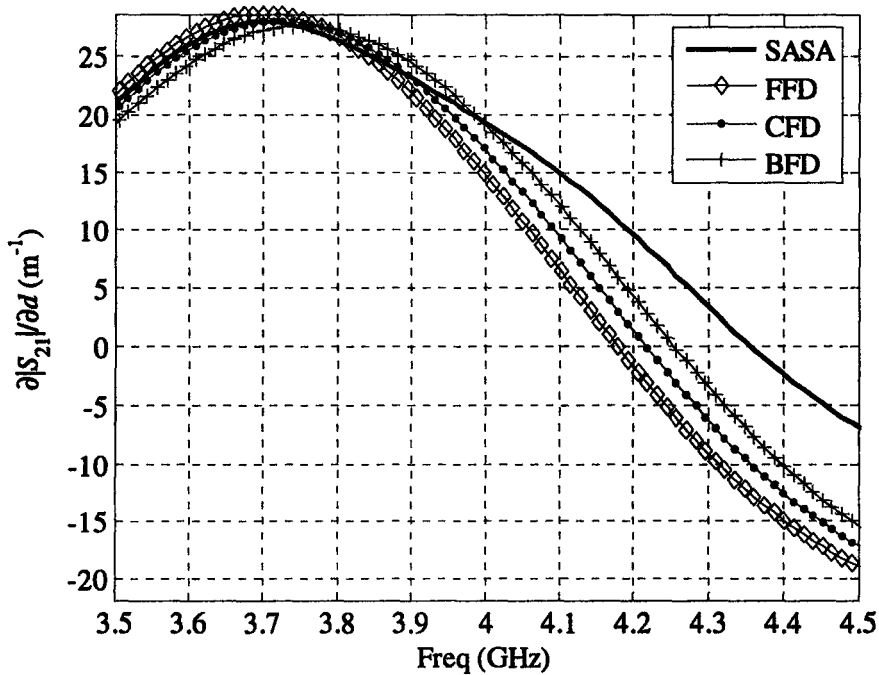


Figure 4.16 Derivatives of $|S_{21}|$ with respect to d over a sweep of frequencies for $[d W] = [28 \Delta h \ 13 \Delta h]$ using metallization.

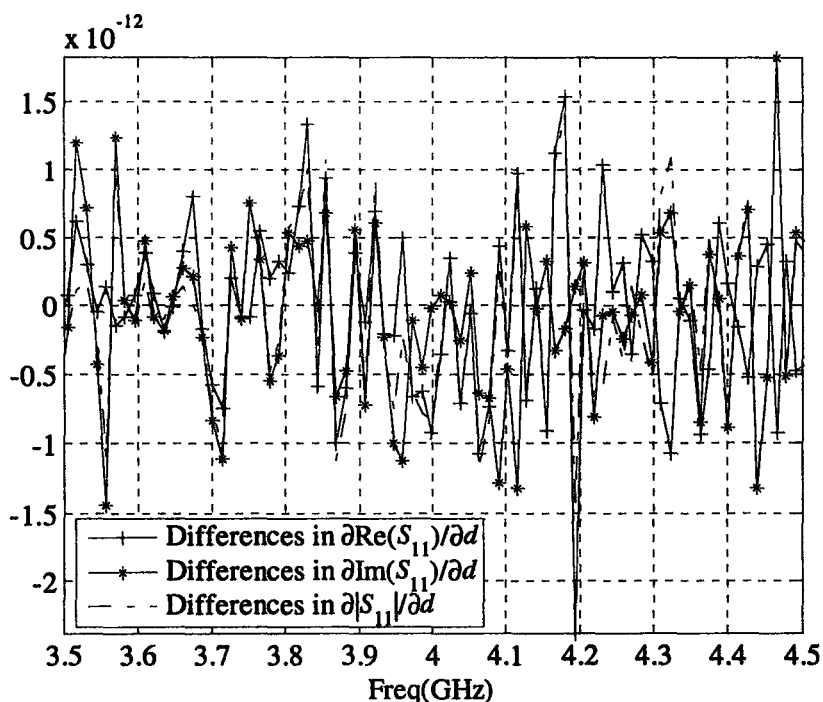


Figure 4.17 Differences in the sensitivities with respect to d between metallization and de-metallization cases.

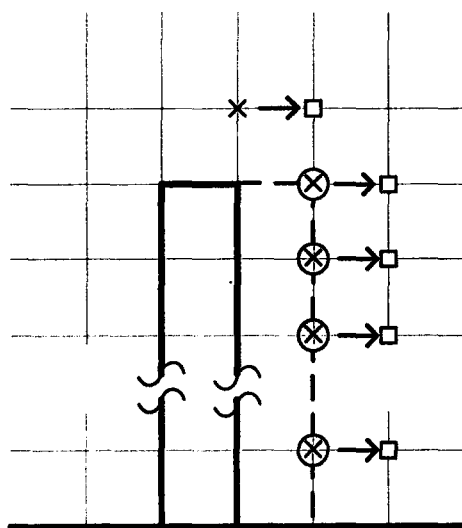


Figure 4.18 Perturbation grid points in the metallization case. The points at which the field is recorded are marked with a cross. The original field and the adjoint field are needed at the points marked with circles and squares, respectively. The arrows denote the field mapping we use to obtain the adjoint field of the perturbed problem.

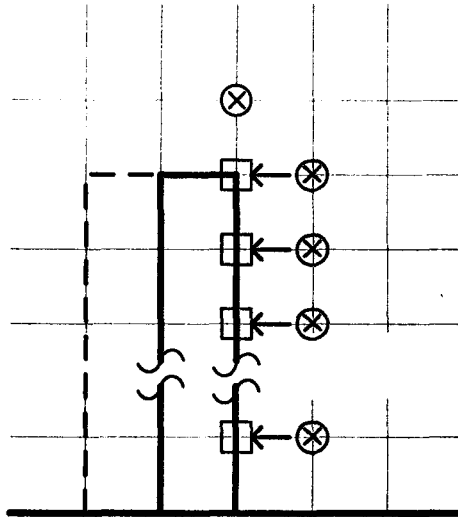


Figure 4.19 Perturbation grid points needed in the de-metallization case. The points at which the field is recorded are marked with a cross. The original field and the adjoint field are needed at the points marked with circles and squares, respectively. The arrows denote the field mapping we use to obtain the adjoint field of the perturbed problem.

We refine the mesh to perform a convergence analysis. We set $\Delta h=0.5$ mm and repeat all the simulations and computations above. The results are shown in Figures 4.19 to 4.25. In Figures 4.23 and 4.26, we compare the S -parameter magnitude sensitivities between $\Delta h=0.5$ mm and $\Delta h=1$ mm cases. In Figure 4.23, we find that the difference between the two SASA curves is not as large as those between finite-difference curves around the resonating frequency and the finite-difference curves become closer to the SASA curve after the refinement. This indicates that the SASA curve has higher accuracy. In Figure 4.26, the difference between the SASA curves is larger than those of the finite-difference curves. This is because of the inaccuracy of the obtained S_{21} itself. And we find again that the finite-difference curves become closer to the

SASA curve with $\Delta h=0.5$.

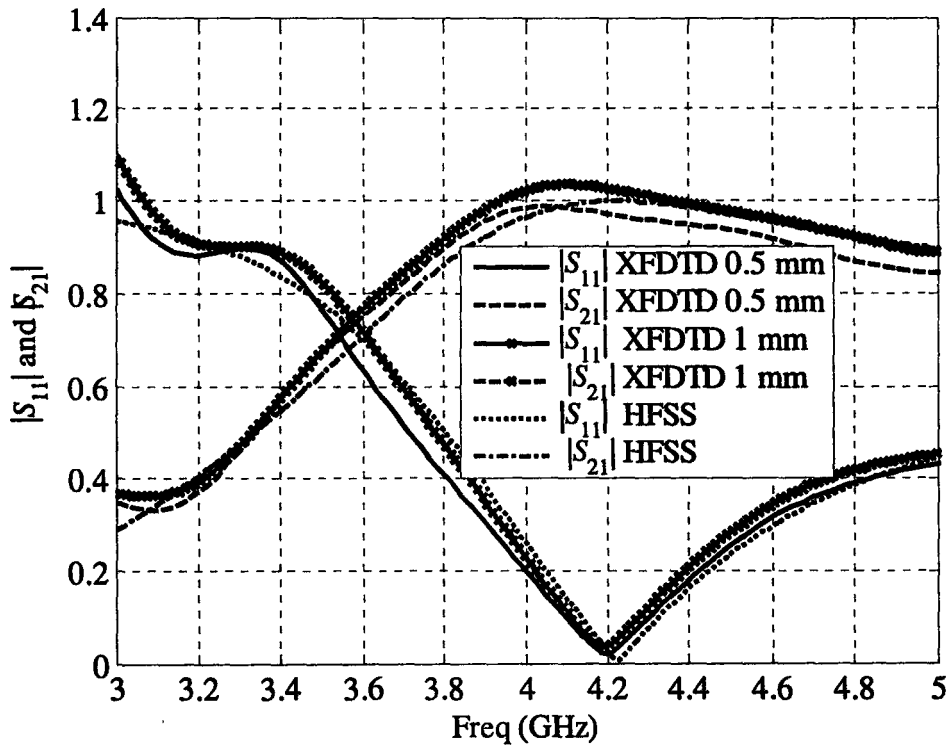


Figure 4.20 Comparison of magnitudes of the S -parameters among $\Delta h=0.5$, $\Delta h=1$ mm, and HFSS results.

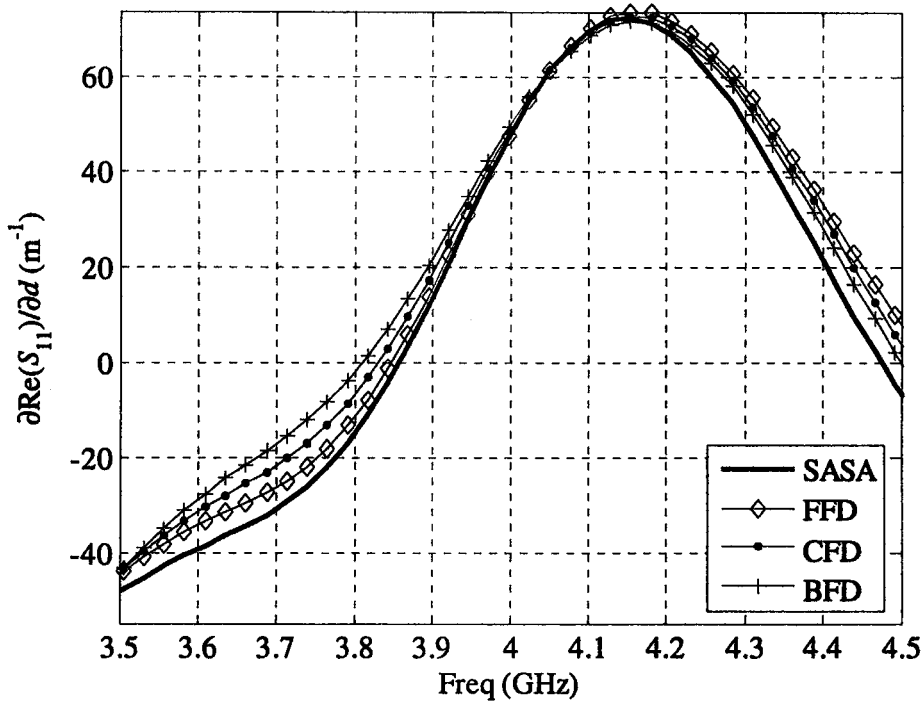


Figure 4.21 Derivative of $\text{Re}(S_{11})$ with respect to d , with $\Delta h = 0.5$ mm.

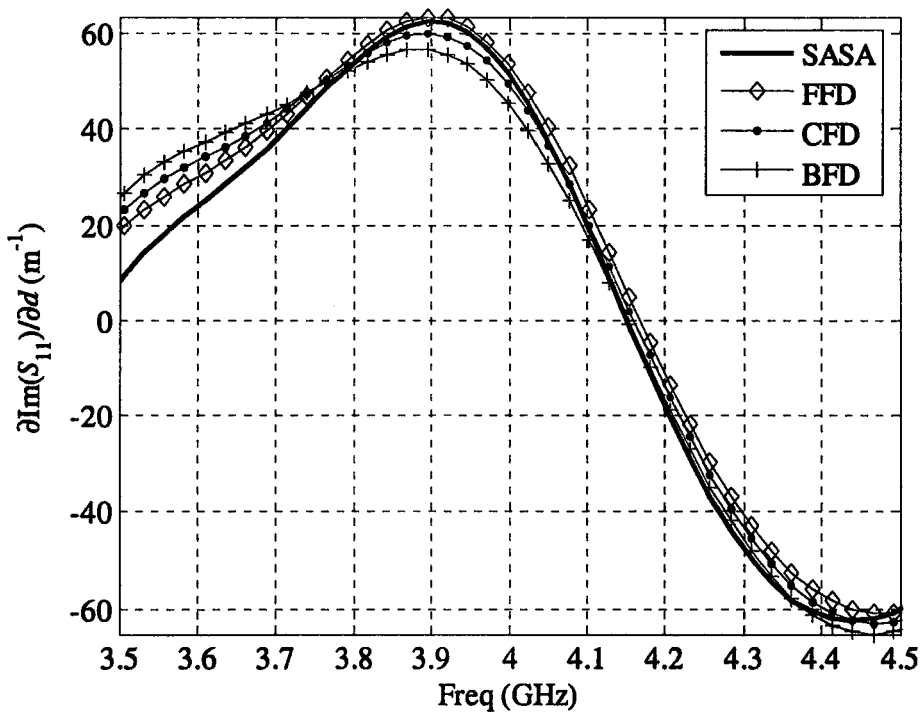


Figure 4.22 Derivative of $\text{Im}(S_{11})$ with respect to d , with $\Delta h = 0.5$ mm.

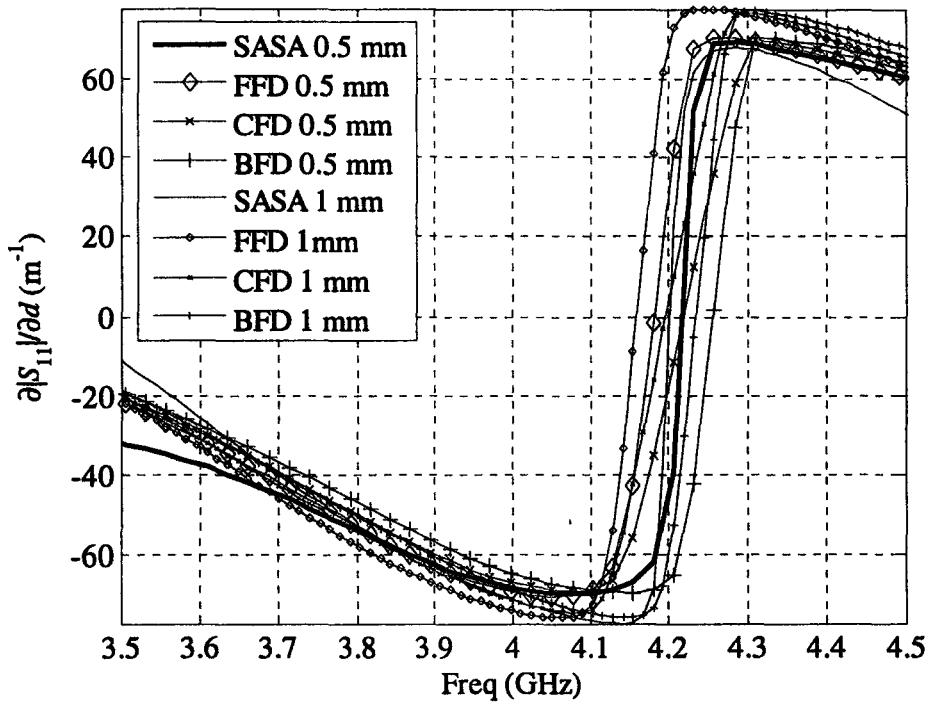


Figure 4.23 Comparison of the derivatives of $|S_{11}|$ with respect to d , with $\Delta h = 0.5$ mm and $\Delta h = 1$ mm.

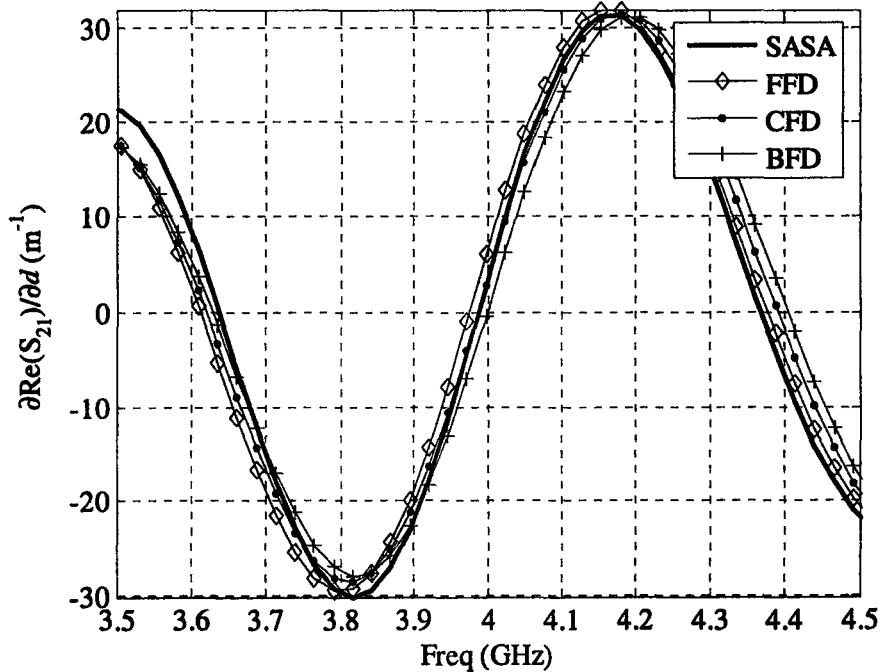


Figure 4.24 Derivative of $\text{Re}(S_{21})$ with respect to d , with $\Delta h = 0.5$ mm.

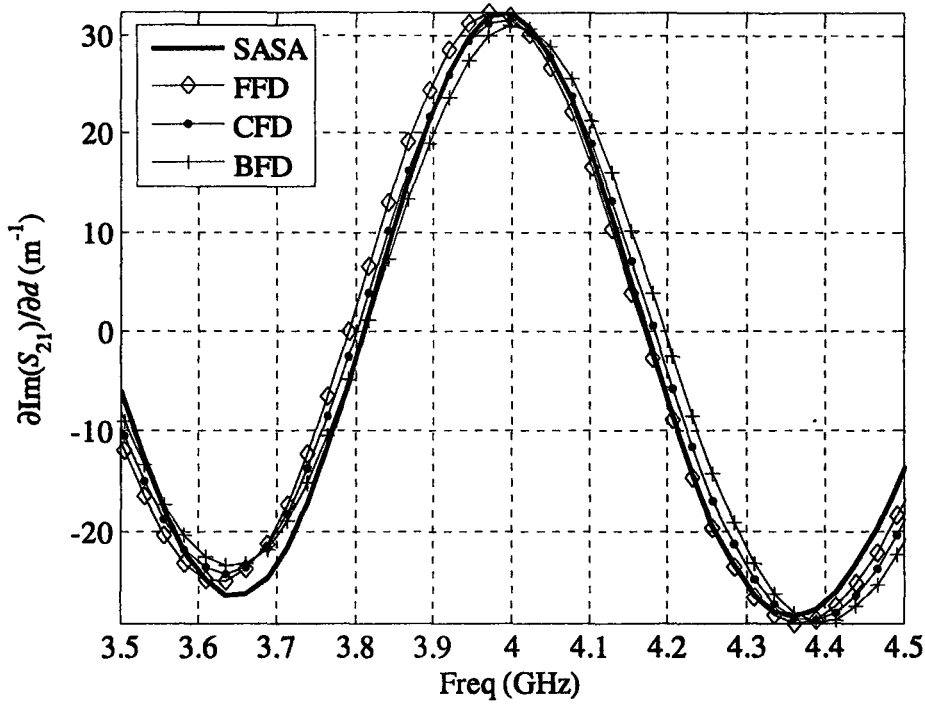


Figure 4.25 Derivative of $\text{Im}(S_{21})$ with respect to d , with $\Delta h = 0.5$ mm.

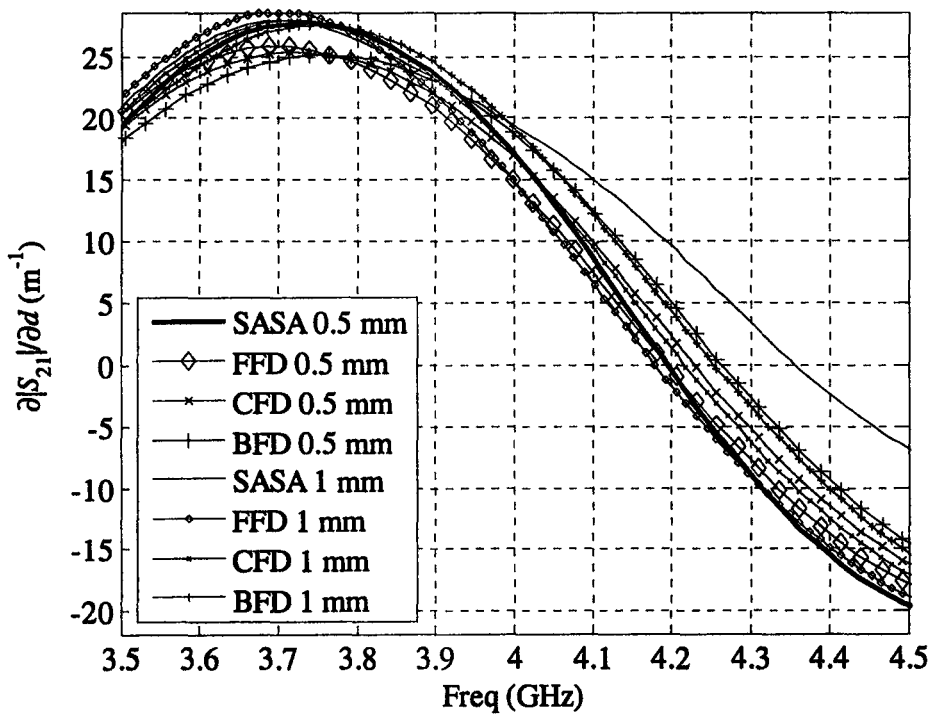


Figure 4.26 Comparison of the derivatives of $|S_{21}|$ with respect to d , with $\Delta h = 0.5$ mm and $\Delta h = 1$ mm.

4.4.2 H-plane filter

The geometry of this filter [15] is shown in Figure 4.27 and the nominal design parameter values are shown in Table 4.1. We consider the derivatives of the S -parameters with respect to L_4 and S_1 . We sweep L_4 from $6\Delta h$ to $15\Delta h$, and S_1 from $21\Delta h$ to $30\Delta h$, with the other parameters set at their nominal values. The settings in XFDTD 6.3 are:

1. Constants: $\Delta h=0.6223$ mm, $\Delta t=1.198\times 10^{-12}$ s and $q=\Delta h/(c\Delta t)=1.7315$.
2. Excitation: The structure is excited with a modulated Gaussian pulse with spectrum from 5 GHz to 10 GHz, which is above the cut-off frequency 4.3 GHz, and has 600 steps in the time domain. We use 5 probes placed uniformly along the excitation plane to form a half sinusoidal modal distribution. The location of the excitation plane is 20 cells away from the absorbing boundary.
3. Ports: We record the central fields 15 steps away from the excitation plane for the input port and 35 steps away from the absorbing boundary for the output port. Note that this is for the S -parameter computation only.
4. Computational domain: The structure has the dimensions $301\Delta h\times 56\Delta h\times 1\Delta h$. The use of one cell in the z direction makes the

simulator run a 2D simulation. We choose Liao's absorbing boundaries at the ports. The simulation time is 40000 time steps.

First, we plot the S -parameters in Figure 4.28, compared with the results of HFSS. Figures 4.28 to 4.30 show the derivatives of S_{21} with respect to L_4 at 7 GHz while Figures 4.31 to 4.34 show their derivatives with respect to S_1 . It is shown that the SASA curves track the central finite difference curve best, especially for the magnitude sensitivities. The magnitude sensitivities of S_{11} and S_{21} must cross the zero point at the same parameter values and the SASA curves do precisely this.

In the XFDTD analysis, we have to run a simulation once to get the S_{11} derivatives while for S_{21} , we have to excite port 2 to get the adjoint fields. However, for this particular example, we do not need to excite port 2 because of its symmetry with respect to port 1 and port 2. One simulation is sufficient to get the derivatives of both S_{11} and S_{21} .

The field components we need to record are the ones adjacent to the perturbed boundary. For the derivatives with respect to L_4 , the recorded field locations are shown in Figure 4.36. Here, we assume the metallization case. For the derivatives with respect to S_1 , the perturbation grid points are shown in Figure 4.37. Here, we assume a shift of the structure to the left, so the grid points on the left side are for the metallization case while the right-hand points are used for the de-metallization case. In Figures 4.35 and 4.36, the points at which the field is recorded are marked with a cross. The original field and the adjoint

field are recorded at the points marked with circles and squares, respectively. The arrows denote the field mapping we use to obtain the adjoint field of the perturbed problem.

The CPU time estimation results are shown in Tables 4.2 and 4.3. Table 4.2 shows the simulation time in XFDTD and Table 4.3 shows the CPU time of the derivative computation. The fast Fourier transform is replaced by the discrete Fourier transform. All these simulations and computations are done on Intel(R) Pentium 4 PCs with CPU clock at 2.8 GHz and RAM at 1 GHz. We use MATLAB v. 7 under Windows XP. From the tables, we find that the derivative computation is fast – it requires at most a couple of seconds. On the other hand, the time-domain EM simulations take at least a couple of minutes in the considered 2-D problems. Therefore, our SASA approach is far more computationally efficient than the finite-difference approximates.

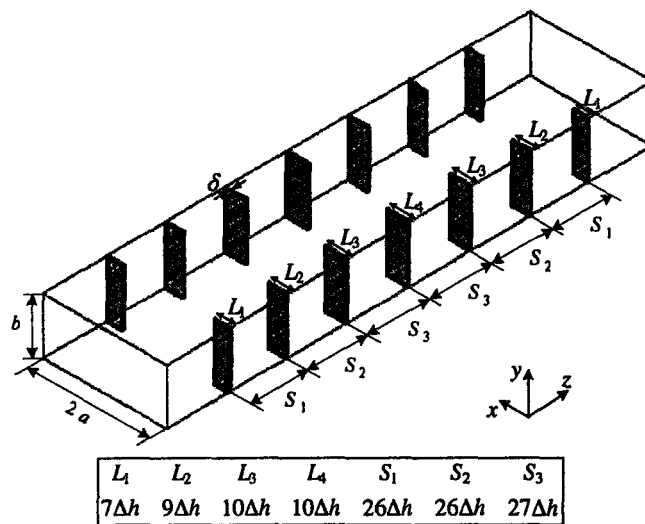
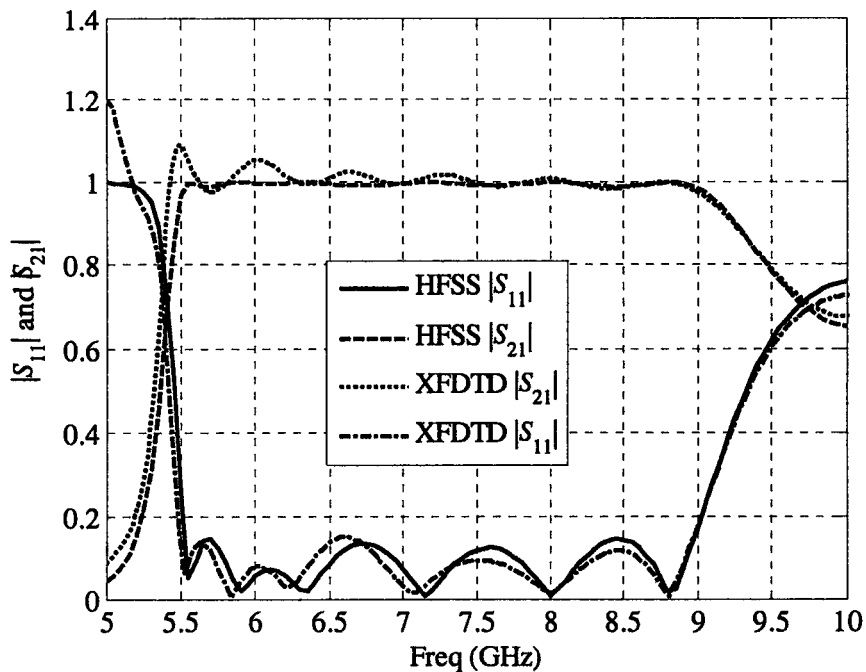


Figure 4.27 The six-resonator H-plane filter [15].

Table 4.1 The nominal design parameter values. (All dimensions in mm)

a	17.4244
b	15.7988
δ	0.62230
L_1	4.35610
L_2	5.60070
L_3	6.22300
L_4	6.22300
S_1	16.1798
S_2	16.1798
S_3	16.8021

Figure 4.28 The S -parameters of the H-plane filter.

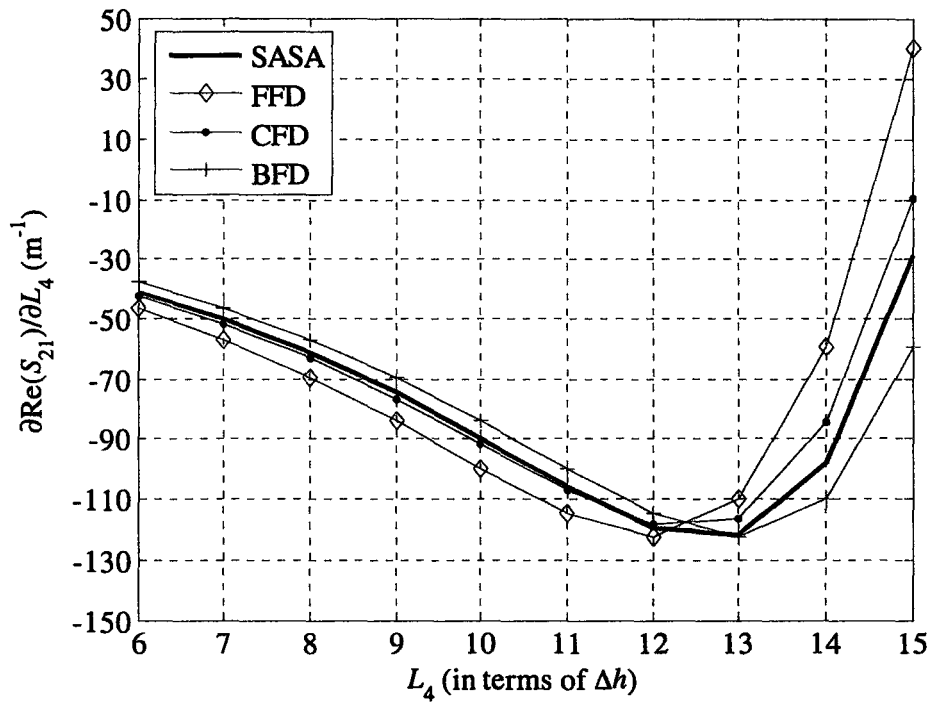


Figure 4.29 The derivative of $\text{Re}(S_{21})$ with respect to L_4 at 7 GHz for the H-plane filter.

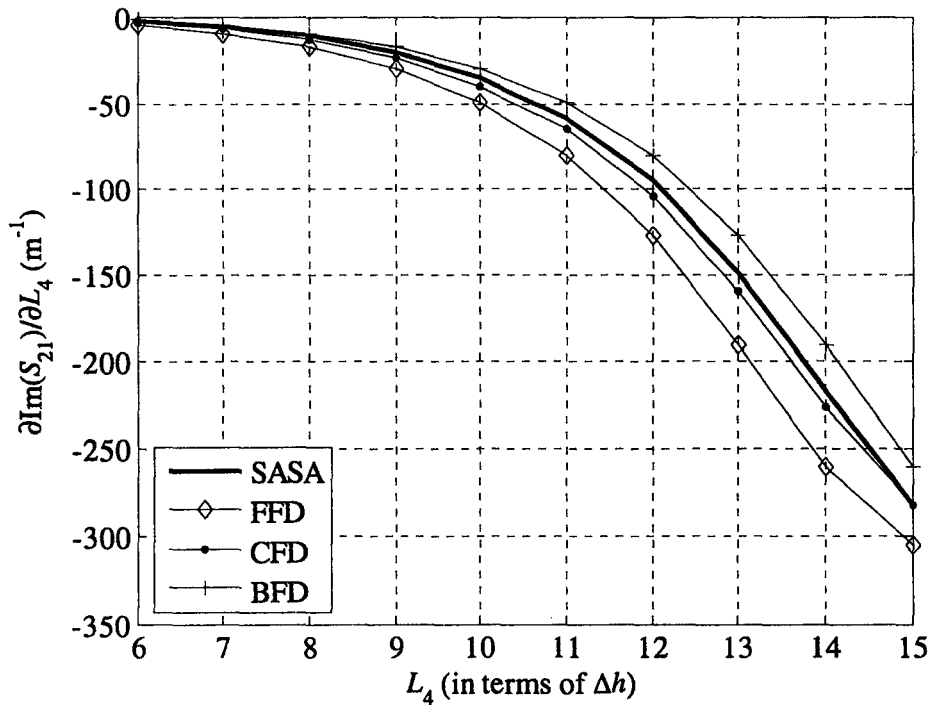


Figure 4.30 The derivative of $\text{Im}(S_{21})$ with respect to L_4 at 7 GHz for the H-plane filter.

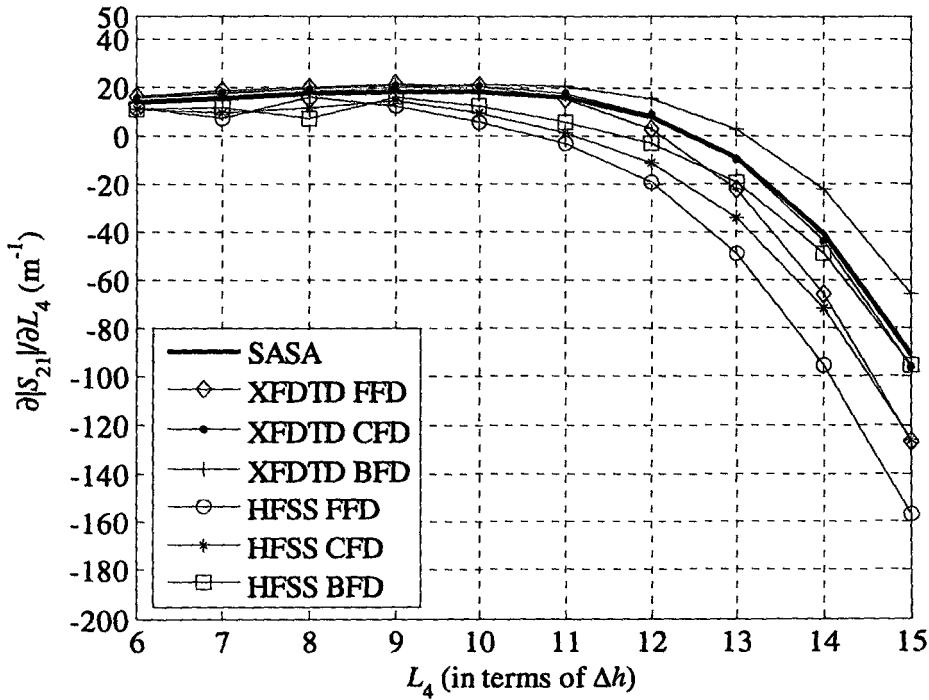


Figure 4.31 The derivative of $|S_{21}|$ with respect to L_4 at 7 GHz for the H-plane filter.

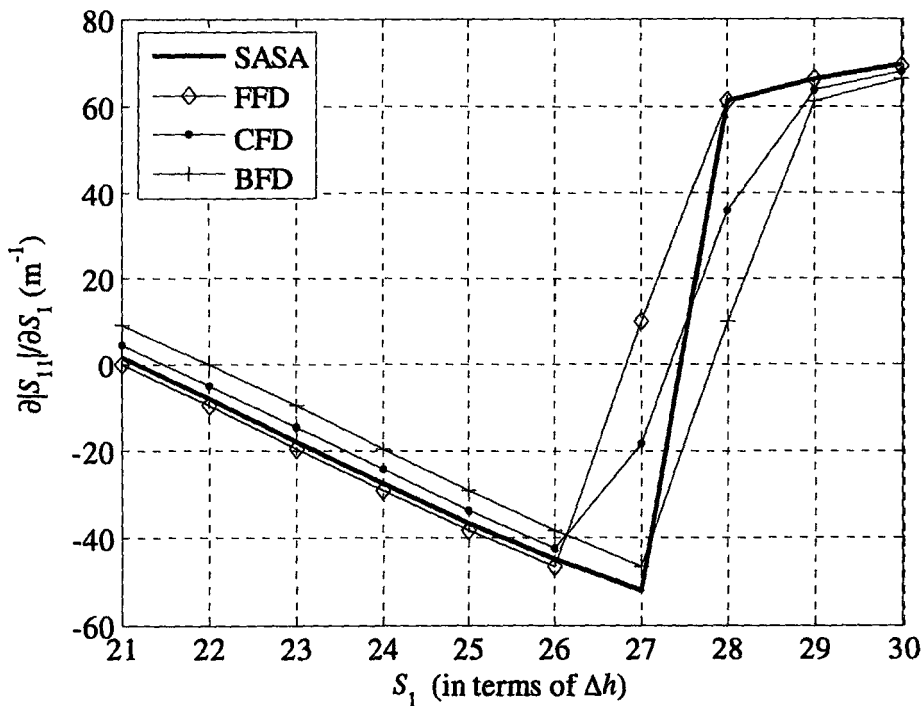


Figure 4.32 The derivative of $|S_{11}|$ with respect to S_1 at 7 GHz for the H-plane filter.

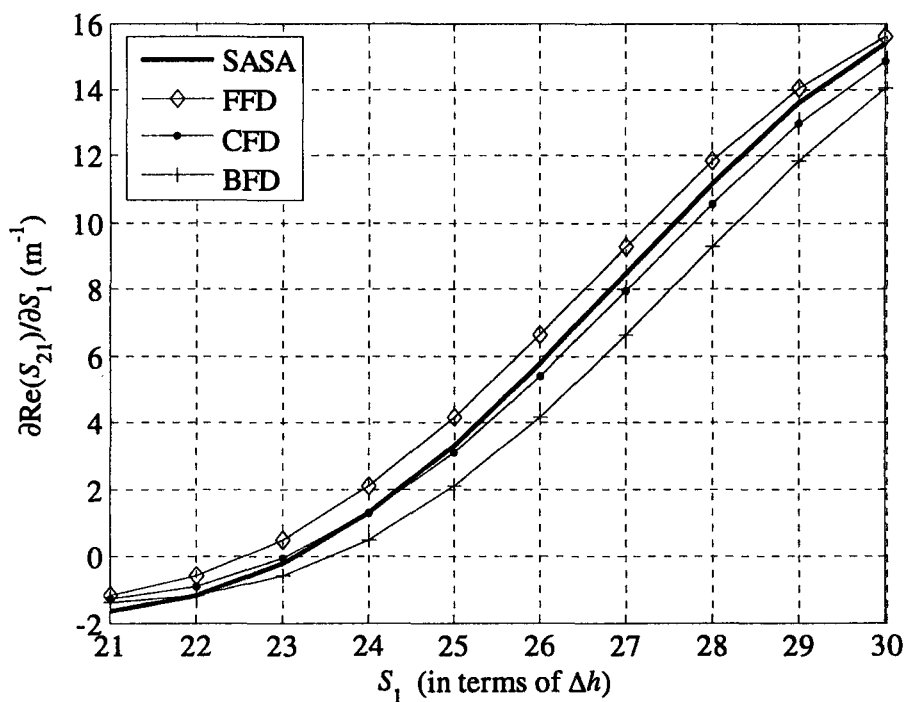


Figure 4.33 The derivative of $\text{Re}(S_{21})$ with respect to S_1 at 7 GHz for the H-plane filter.

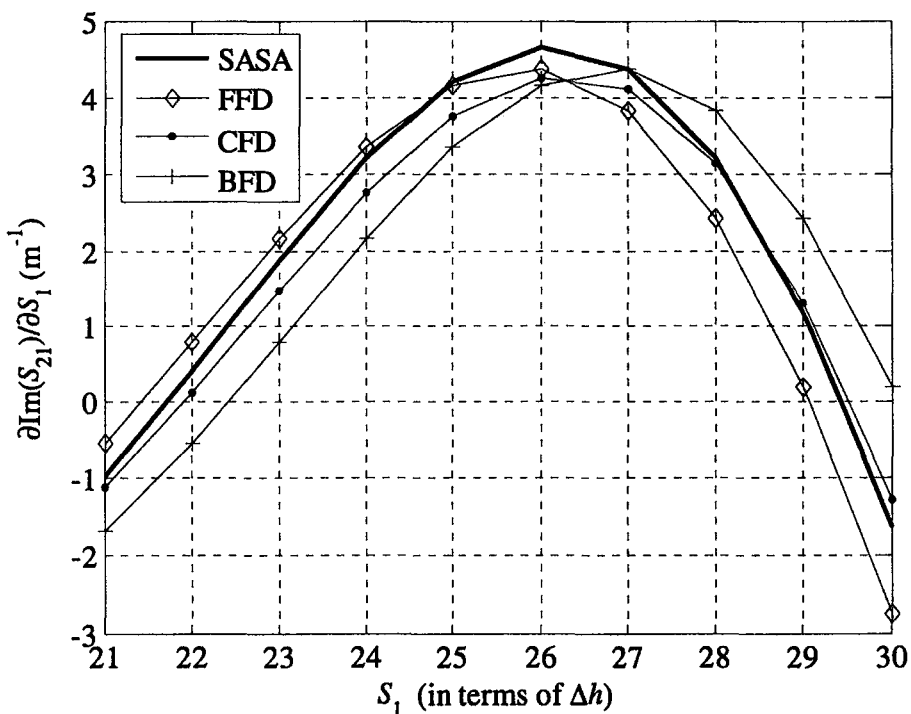


Figure 4.34 The derivative of $\text{Im}(S_{21})$ with respect to S_1 at 7 GHz for the H-plane filter.

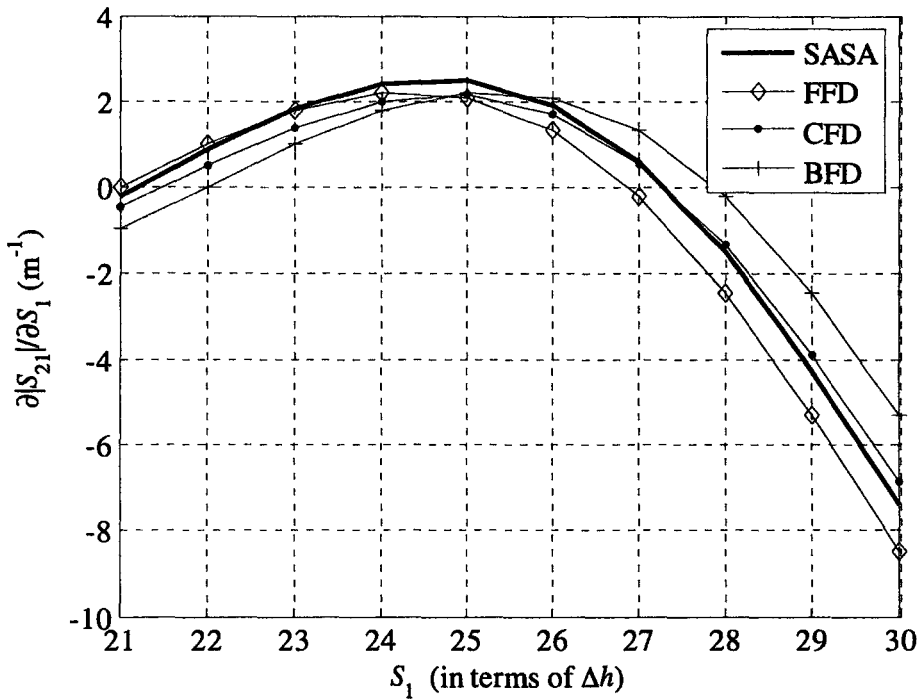


Figure 4.35 The derivative of $|S_{21}|$ with respect to S_1 at 7 GHz for the H-plane filter.

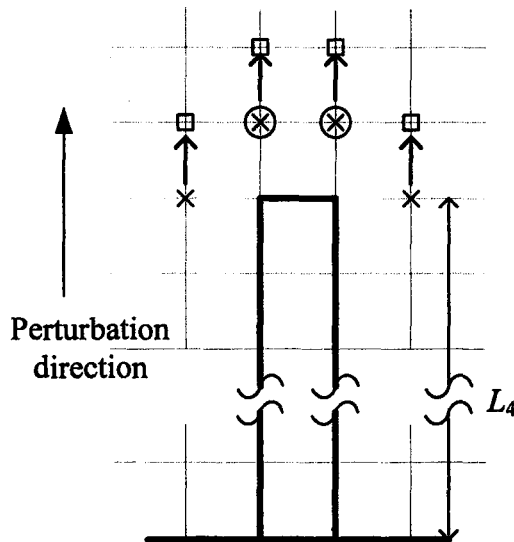


Figure 4.36 The recorded-field points for the derivatives with respect to L_4 . The points, at which the field is recorded, are marked with a cross. The original field and the adjoint field are needed at the points marked with circles and squares, respectively. The arrows denote the field mapping we use to obtain the adjoint field of the perturbed problem.

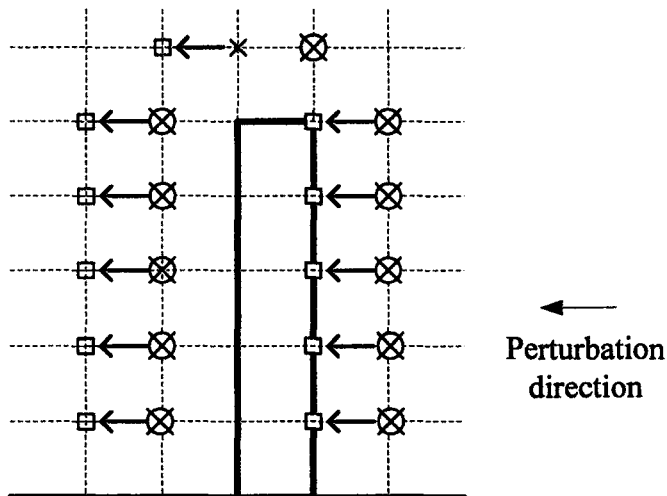


Figure 4.37 The recorded-field points for the derivatives with respect to S_1 . The points, at which the field is recorded, are marked with a cross. The original field and the adjoint field are needed at the points marked with circles and squares, respectively. The arrows denote the field mapping we use to obtain the adjoint field of the perturbed problem.

Table 4.2 Simulation time in XFDTD.

Without any probes	1min 44s
With 2 probes to compute S -parameter	3min 51s + 2min 48s (reference waveguide with 1 probe)
Reference waveguide input (5 probes)	6min 47s
With probes to compute the sensitivity with respect to L_4 (4 probes)	7min 32s
With probes to compute the sensitivity with respect to S_1 (32 probes)	34min 13s

Table 4.3 Derivative computation time in MATLAB.

Sensitivities of S_{11} (real, imaginary, magnitude) with respect to L_4	0.2969s
Sensitivities of S_{21} (real, imaginary, magnitude) with respect to L_4	0.2813s
Sensitivities of S_{11} and S_{21} (real, imaginary, magnitude) with respect to L_4	0.2969s
Sensitivities of S_{11} (real, imaginary, magnitude) with respect to S_1	1.5000s
Sensitivities of S_{21} (real, imaginary, magnitude) with respect to S_1	1.5469s
Sensitivities of S_{11} and S_{21} (real, imaginary, magnitude) with respect to S_1	1.5625s

4.5 Feasibility of Other Time-domain Simulators

In addition to the FDTD-based time-domain simulators, we can also implement the SASA approach with the TLM-based simulators, i.e. MEFiSTo-3D Pro. Since the locations of the field points on the TLM grid do not coincide with those on the FDTD Yee grid, we perform averaging [16] to obtain the field at the points required by the FDTD-based self-adjoint method.

In summary, no matter which time-domain simulator we use to solve the EM problem, as long as the simulator is capable of providing the field solutions at

the designated points, the SASA approach can be implemented.

4.6 Summary

In this chapter, the proposed self-adjoint sensitivity analysis approach is implemented with one of the commercial time-domain FDTD-based simulators, XFDTD v. 6.3. In order to excite the desired mode, we use 5 excitation points to conform to a modal distribution across the port. The field solution is exported and manipulated in MATLAB to yield the sensitivity information. Two waveguide examples are presented to illustrate the settings in XFDTD v. 6.3 and to verify the SASA approach.

We find several features of the SASA approach through the implementation. Refining the mesh helps improve the accuracy of the algorithm since more points are involved in the computation of the sensitivities as well as the field solution becomes more accurate. The perturbation direction (metallization and de-metallization) makes no difference in the sensitivity results, because the same field information is used in the implementation and the only difference is which field relates to the original field and which to the adjoint field. We also estimate the computational overhead of the XFDTD simulation and sensitivity computation, from which we confirm that our SASA approach yields higher efficiency than the finite-difference method.

4.7 References

- [1] Remcom Inc., <http://www.remcom.com>.
- [2] Zeland Software Corporation, <http://www.zeland.com>.
- [3] Faustus Scientific Corporation, <http://www.faustus.com>.
- [4] Ansoft corporation, <http://www.ansoft.com>.
- [5] COMSOL Inc., <http://www.comsol.com>.
- [6] Agilent Technologies, <http://www.agilent.com>.
- [7] Sonnet Software, Inc., <http://www.sonnetusa.com>.
- [8] EM Software & Systems-S.A. (Pty) Ltd., <http://www.feko.info/index.html>.
- [9] OSA/900hope (1997) Version 4.0, formerly Optimization Systems Associates Inc., P. O. Box 8083, Dundas, Ontario, Canada L9H 5E7, now Agilent Eseof EDA, 1400 Fountaingrove Parkway, Santa Rosa, CA 95403-1799.
- [10] Empipe (1997) Version 4.0, formerly Optimization Systems Associates Inc., P. O. Box 8083, Dundas, Ontario, Canada L9H 5E7, now Agilent Eseof EDA, 1400 Fountaingrove Parkway, Santa Rosa, CA 95403-1799.
- [11] Empipe3D (1997) Version 4.0, formerly Optimization Systems Associates Inc., P. O. Box 8083, Dundas, Ontario, Canada L9H 5E7, now Agilent Eseof EDA, 1400 Fountaingrove Parkway, Santa Rosa, CA 95403-1799.
- [12] XFDTD® v. 6.3, *Reference Manual*. Remcom, 2005.
- [13] MATLAB v. 7, The MathWorks, Inc.,

<http://www.mathworks.com/products/matlab>.

- [14] M. H. Bakr and N. K. Nikolova, "An adjoint variable method for time domain TLM with fixed structured grids," *IEEE Trans. Microwave Theory Tech.*, vol. 52, pp. 554-559, February 2004.
- [15] G. Matthaei, L. Young, and E. M. T. Jones, *Microwave Filters, Impedance-Matching Networks, and Coupling structures*. Norwood, MA: Artech House, 1980, p. 545.
- [16] N. K. Nikolova, Ying Li, Yan Li, M. H. Bakr, "Sensitivity analysis of scattering parameters with electromagnetic time-domain simulators," *IEEE Trans. Microwave Theory Tech.*, vol. 54, pp. 1598-1610, April 2006.

Chapter 5

CONCLUSIONS

In this thesis, a self-adjoint sensitivity analysis (SASA) algorithm for applications with the finite-difference time-domain (FDTD) method is developed. The application of the SASA algorithm to the S -parameter sensitivity analysis is our focus. Several 2-D waveguide examples are investigated. The implementations are conducted with both an in-house FDTD solver and one of the commercial FDTD simulators, XFDTD v. 6.3.

A brief review of the FDTD method is presented in Chapter 2. In addition to the FDTD basics, we focus on the special considerations for the waveguide structure simulation and the computation of the S -parameters from the FDTD field solution at the ports. This is essential in our later developments of the S -parameter sensitivity analysis approach.

The adjoint variable method (AVM) theory and the development of the SASA algorithm are discussed in detail in Chapter 3. Our SASA approach is an efficient way to compute the gradient of the response of a high frequency (HF) structure. Compared to the original AVM, it improves the efficiency of the sensitivity computation drastically since it eliminates the additional (adjoint)

simulation. The S -parameter sensitivities are analyzed with the SASA method, since the self-adjoint condition of the problem is met. The application of the SASA algorithm to the waveguide structures is presented, with the original problem simulated in the in-house FDTD solver. Examples illustrate the S -parameter sensitivities computation with respect to both the shape and constitutive parameters in metallic and lossy dielectric objects. The SASA method features second-order accuracy and high computational efficiency.

The SASA application with commercial time-domain simulators is presented in Chapter 4. XFDTD v. 6.3 is utilized as a typical time-domain FDTD simulator, providing the E -field solution for the S -parameter sensitivity computation. We describe the necessary settings of the XFDTD simulation for the waveguide structure. The way the necessary field values at the perturbation grid points are exported is also explained in detail. Two waveguide filter examples are provided, with the details of the XFDTD simulation set-up. The computational overhead is estimated for the sensitivity computation and it is compared with the simulation time of XFDTD. The SASA shows superior efficiency over the finite-difference approximation. Our implementation has only one requirement for the simulator — the ability to export the time-dependent field solution at user-defined points. Most commercial solvers have this ability, which makes the SASA readily applicable to practical optimization and tolerance analysis.

From the experience and knowledge gained in the above work, the

following topics for further research are suggested:

1. At present, all the examples involving the perfect metallic objects are 2-D examples. 3-D metallic examples are needed to confirm the SASA technique and its implementation. The differencing of the double-curl operator in the 3-D case must be implemented in order to compute the derivatives of the system coefficients in the case of 3-D metallic details and infinitesimally thin strips of finite size.
2. The SASA method has not been applied yet to practical optimization or to tolerance and yield analyses. This is essential for the future development of an efficient CAD framework exploiting design sensitivities.

COMPLETE REFERENCE LIST

Chapter 1

- [1] E. J. Haug, K. K. Choi, and V. Komkov, *Design Sensitivity Analysis of Structural System*. New York: Academic, 1996.
- [2] L. J. Lions, *Optimal Control of Systems Governed by Partial Differential Equations*. S. K Mitter, Ed. Berlin, Germany: Springer-Verlag, 1971.
- [3] S. W. Director and R. A. Rohrer, "The generalized adjoint network and network sensitivities," *IEEE Trans. Circuit Theory*, vol. CT-16, pp. 318-323, Aug. 1969.
- [4] S. W. Director and R. A. Rohrer, "Automated network design- The frequency-domain case," *IEEE Trans. Circuit Theory*, vol. CT-16, pp. 330-337, Aug. 1969.
- [5] B. D. H. Tellegen, "A general network theorem, with applications," *Philips Res. Rep.*, vol. 7, pp. 259-269, 1959.

- [6] P. Penfield, Jr., R. Spence, and S. Duinker, "A generalized form of Tellegen's theorem," *IEEE Trans. Circuit Theory*, vol. CT-17, pp. 302-305, Aug. 1970.
- [7] N. K. Nikolova, H. W. Tam, M. H. Bakr, "Sensitivity analysis with the FDTD method on structured grids," *IEEE Trans. Microwave Theory Tech.*, vol. 52, pp. 1207-1216, Apr. 2004.
- [8] G. Shen, H. W. W. Tam, N. K. Nikolova, M. H. Bakr, "Adjoint sensitivity techniques for FDTD method on structured grids," *IEEE/URSI Int. Antennas and Propagation Symp. Dig. 2003*, vol. 3, Columbus, OH, June 2003, pp. 746-749.
- [9] M. H. Bakr, N. K. Nikolova, "An adjoint variable method for time domain TLM with fixed structured grids," *IEEE/URSI Int. Antennas and Propagation Symp. Dig. 2003*, vol. 2, Columbus, OH, June 2003, pp. 1121-1124.
- [10] P. A. W. Basl, M. H. Bakr, N. K. Nikolova, "An AVM technique for 3-D TLM with symmetric condensed nodes," *IEEE Microwave and Wireless Components Letters*, vol. 15, pp. 618-620, Oct. 2005.
- [11] N. K. Georgieva, S. Glavic, M. H. Bakr and J. W. Bandler, "Feasible adjoint sensitivity technique for EM design optimization," *IEEE Trans. Microwave Theory Tech.*, vol. 50, pp. 2751-2758, Dec. 2002.
- [12] M. H. Bakr and N. K. Nikolova, "An adjoint variable method for frequency domain TLM problems with conducting boundaries," *IEEE*

Microwave and Wireless Components Letters, vol. 13, pp. 408-410, Sept. 2003.

- [13] S. M. Ali, N. K. Nikolova, and M. H. Bakr, "Recent advances in sensitivity analysis with frequency-domain full-wave EM solvers," *Applied Computational Electromagnetics Society Journal*, vol. 19, pp. 147-154, Nov. 2004.
- [14] XFDTD v. 6.3, Remcom, <http://www.remcom.com>.

Chapter 2

- [1] K. S. Yee, "Numerical solution of initial boundary value problems involving Maxwell's equations in isotropic media," *IEEE Trans. Antennas Propagat.*, vol. AP-14, pp. 302-307, 1966.
- [2] T. Weiland, "A discretization method for the solution of Maxwell's equations for six-component fields," *Electronics and Communication (AEU)*, vol. 31, 1977, pp. 116-120.
- [3] Y. Qian and T. Itoh, *FDTD Analysis and Design of Microwave Circuits and Antennas: Software and Applications*. Realize Inc., Tokyo, 1999.
- [4] A. Taflove, *Computational Electrodynamics: the Finite-Difference Time-Domain Method*. Artech House, 1995.

- [5] K. Kunz, R. Luebbers, *Finite-Difference Time-Domain Method for Electromagnetics*. Artech House, 1995.
- [6] N. K. Nikolova, Ying Li, Yan Li, M. H. Bakr, “Sensitivity analysis of scattering parameters with electromagnetic time-domain simulators,” *IEEE Trans. Microwave Theory Tech.*, vol. 54, pp. 1598-1610, April 2006.
- [7] N. Marcuvitz, *Waveguide Handbook*. London, UK: Peter Peregrinus Ltd., 1993 reprint, Chapter 2.
- [8] D. Pozar, *Microwave Engineering*. USA: Addison Wesley Publishing Company Inc., 1993.
- [9] N. K. Nikolova, “The finite-difference time-domain (FDTD) method-part III,” lecture notes of ECE 758 Numerical Techniques in Electromagnetics, Electrical & Computer Engineering Department, McMaster University, Fall 2004.
- [10] N. K. Nikolova, “Extracting S -parameter derivatives from time domain solutions: the case,” Computational Electromagnetics Research Laboratory presentation, Dec. 2004.

Chapter 3

- [1] E. J. Haug, K. K. Choi and V. Komkov, *Design Sensitivity Analysis of Structural Systems*. Academic Press Inc., Harcourt Bruce Jovanovich Publishers, Orlando, Florida, 1986.

-
- [2] Y. Chung, C. Cheon, I. Park, and S. Hahn, "Optimal shape design of microwave device using FDTD and design sensitivity analysis," *IEEE Trans. on Microwave Theory Tech.*, vol. 48, no. 12, pp. 2289-2296, December 2000.
- [3] N. K. Nikolova, "Sensitivity analysis with EM solvers on structured grids: the FDTD case," Computational Electromagnetics Research Laboratory presentation, December 2004.
- [4] M. H. Bakr and N. K. Nikolova, "An adjoint variable method for time domain TLM with fixed structured grids," *IEEE Trans. Microwave Theory Tech.*, vol. 52, pp. 554-559, February 2004.
- [5] N. K. Nikolova, H. W. Tam, and M. H. Bakr, "Sensitivity analysis with the FDTD method on structured grids," *IEEE Trans. Microwave Theory Tech.*, vol. 52, pp. 1207-1216, April 2004.
- [6] J. C. Strikwerda, *Finite Difference Schemes and Partial Differential Equations*. Pacific Grove, California: Wadsworth & Brooks, 1989, Chapter 3.
- [7] N. K. Nikolova, Ying Li, Yan Li, M. H. Bakr, "Sensitivity analysis of scattering parameters with electromagnetic time-domain simulators," *IEEE Trans. Microwave Theory Tech.*, vol. 54, pp. 1598-1610, April 2006.
- [8] M. H. Bakr and N. K. Nikolova, "An adjoint variable method for time domain TLM with fixed structured grids," *IEEE Trans. Microwave Theory Tech.*, vol. 52, pp. 554-559, Feb. 2004.

- [9] Ying Li, Yan Li, N. K. Nikolova, and M. H. Bakr, “Time domain sensitivity analysis of lossy dielectric structures,” *Frontiers in Applied Computational Electromagnetics*, June 2006.
- [10] Y. Qian, T. Itoh, *FDTD Analysis and Design of Microwave Circuits and Antennas*. Realize Inc.1999, Chapter. 4.
- [11] N. Marcuvitz, *Waveguide Handbook*. London, UK: Peter Peregrinus Ltd., 1993 reprint, Chapter 2.
- [12] D. Pozar, *Microwave Engineering*, Addison Wesley Publishing Company Inc., USA, 1993.

Chapter 4

- [1] Remcom Inc., <http://www.remcom.com>.
- [2] Zeland Software Corporation, <http://www.zeland.com>.
- [3] Faustus Scientific Corporation, <http://www.faustus.com>.
- [4] Ansoft corporation, <http://www.ansoft.com>.
- [5] COMSOL Inc., <http://www.comsol.com>.
- [6] Agilent Technologies, <http://www.agilent.com>.
- [7] Sonnet Software, Inc., <http://www.sonnetusa.com>.
- [8] EM Software & Systems-S.A. (Pty) Ltd., <http://www.feko.info/index.html>.
- [9] OSA/900hope (1997) Version 4.0, formerly Optimization Systems Associates Inc., P. O. Box 8083, Dundas, Ontario, Canada L9H 5E7, now

- Agilent Eseof EDA, 1400 Fountaingrove Parkway, Santa Rosa, CA 95403-1799.
- [10] Empipe (1997) Version 4.0, formerly Optimization Systems Associates Inc., P. O. Box 8083, Dundas, Ontario, Canada L9H 5E7, now Agilent Eseof EDA, 1400 Fountaingrove Parkway, Santa Rosa, CA 95403-1799.
- [11] Empipe3D (1997) Version 4.0, formerly Optimization Systems Associates Inc., P. O. Box 8083, Dundas, Ontario, Canada L9H 5E7, now Agilent Eseof EDA, 1400 Fountaingrove Parkway, Santa Rosa, CA 95403-1799.
- [12] XFDTD® v. 6.3, *Reference Manual*. Remcom, 2005.
- [13] MATLAB v. 7, The MathWorks, Inc.,
<http://www.mathworks.com/products/matlab>.
- [14] M. H. Bakr and N. K. Nikolova, "An adjoint variable method for time domain TLM with fixed structured grids," *IEEE Trans. Microwave Theory Tech.*, vol. 52, pp. 554-559, February 2004.
- [15] G.. Matthaei, L. Young, and E. M. T. Jones, *Microwave Filters, Impedance-Matching Networks, and Coupling structures*. Norwood, MA: Artech House, 1980, p. 545.
- [16] N. K. Nikolova, Ying Li, Yan Li, M. H. Bakr, "Sensitivity analysis of scattering parameters with electromagnetic time-domain simulators," *IEEE Trans. Microwave Theory Tech.*, vol. 54, pp. 1598-1610, April 2006.